Generating entangled photons from spontaneous parametric down-conversion pumped by incoherent light sources

Author:
Cheng LI

Supervisor:
Professor Robert W.BOYD

Thesis submitted to the University of Ottawa
in partial fulfillment of the requirements for the
Doctorate in Philosophy Physics

Department of Physics
Faculty of Science
University of Ottawa

Abstract

Spontaneous parametric down-conversion (SPDC) can produce entangled photons from a nonlinear medium driven by a pump beam, and has thus been a key resource in photonic quantum technologies. Historically, the low efficiency of SPDC prompted the use of lasers, which are high-intensity light sources, as pump sources. However, the practical implementation of laser-driven systems faces an imminent energy bottleneck. Lasers typically have suboptimal energy efficiencies due to lasing thresholds and the technical demands of thermal management. As a result, laser-pumped entangled photon sources suffer from significant power overhead, rendering quantum devices less sustainable. Over the past few decades, light-emitting diodes (LEDs) have emerged as inexpensive and energy-efficient alternatives for high-intensity light sources. Since 2010, studies have shown that LEDs can drive SPDC and generate photon pairs. These results suggests the potential to replace lasers with ubiquitous and natural light sources to build environmentally friendly quantum devices. However, replacing lasers with other light sources entails a lack of coherence in all degrees of freedom (DoFs) of the pump beam, including spatial, temporal-spectral, and polarization, which may influence the resulting entanglement generated from SPDC. While earlier studies established that pump coherence in a specific DoF sets an upper bound for entanglement in that same DoF, the cross-influence between different DoFs has not been fully investigated. In this thesis, we study the influence of the pump's spatiotemporal coherence on the polarization entanglement generated from SPDC. First, we experimentally demonstrate that polarization-entangled two-photon states can be generated from SPDC pumped by spatiotemporally incoherent light emitted from an LED. Although the resulting entanglement appears lower than that of laser-pumped SPDC, we theoretically show that spatiotemporal incoherence does not fundamentally constrain polarization entanglement; rather, the reduction arises from a coupling between spatiotemporal and polarization DoFs introduced by the experimental setup. We determined experimentally that this cross-influence acts as a deterministic mapping from the spatial components of the pump to the two-photon polarization state. Because this mapping depends on technical aspects of the setup, we envisioned that it could be either (i) engineered to structure entanglement in higher dimensions, or (ii) compensated to reduce spatial distinguishability. Building on the latter, we show that by placing the nonlinear medium in a phase-compensated interferometric setup, SPDC pumped by spatially incoherent light can produce high polarization entanglement that violates local realism, even without postselecting the SPDC field for a single spatial mode. Finally, as a proof-of-principle demonstration of a truly environmentally friendly quantum light source, we demonstrate the generation of polarization-entangled two-photon states from SPDC pumped by a natural source—sunlight.

Acknowledgements

First of all, I would like to express my sincerest gratitude to my supervisor, Prof. Robert Boyd. His support and guidance are what made this thesis possible. Joining his research group turns out to be one of the best decisions I have ever made in my life. He placed his faith in me during my moments of heightened self-doubt and took me under his wing when I felt adrift in my academic endeavours. His passion for science, attentiveness to rigor, and breadth of intellectual curiosity exemplify the scientist I aspire to be. From him, I have learned always to think critically and dare to question assumptions that even the best of us have taken for granted.

My PhD journey would not have been smooth and steady without the wonderful mentors by my side: Dr. Boris Braverman and Dr. Girish Kulkarni, who were then postdocs of the group (and now professors at the University of Toronto and the Indian Institute of Technology, Ropar, respectively), and Dr. Jeremy Upham, our beloved lab manager. From the beginning of my PhD study, they have always come to my aid whenever I need help understanding fundamental concepts, troubleshooting experimental setups, or navigating the administrative intricacies. I have learned as much from their actions as from their words. Working with them has not only enabled me to conduct good research but also prepared me to become a better researcher.

I feel honoured to have worked alongside and befriended my amazing peers: Maryam Abbasi, Mahtab Amooei, Saad Bin Alam, Aaron Cardoso, Lin Cheng, Manuel Ferrer, Brayden Freitas, Ryan Hogan, Yuelang Huang, Mahdieh Jabbari, Mohammad Karimi, Theng Loo Lim, Xialin Liu, Tobey Luck, Yaryna Mamchur, Omid Mozafar, Jeremy Rioux, Isaac Soward, Sisira Suresh, Jesse Thompson, Yaswant Vaddi, Qiang Wang, and Juntong Yang. Outside of academia, I am proud to call these beautiful souls my friends: Aran Chen, Eryi Dong, Yu Huang, Jiaying Jin, Yechen Shen, Sizhao Wei, Ruoshi Xu, M.K. (Roya), and Yichang Zhao. Having arrived at Ottawa as a stranger, I can now call this city home away from home because of all my friends.

I am forever in debt to my mother, Xiaoying Li, and my father, Zhigeng Li. Thank you for bringing me to this colorful world that I have just started to explore. Thank you for raising me and believing in my dream. To my entire family, thank you for your love and support that have made me who I am today.

Special thanks to Dua Lipa, Billie Eilish, and Laufey. Your great works of music have made every minute of my PhD life even more enjoyable.

Contents

List of Figures

List of Tables

List of Publications

1. **C. Li**, B. Braverman, G. Kulkarni, and R. W. Boyd, "Experimental generation of polarization entanglement from spontaneous parametric down-conversion pumped by spatiotemporally highly incoherent light." *Physical Review A* **107**(4), L041701 (2023).
2. A. Mavian, Y. Xu, **C. Li**, and R. W. Boyd, "Fast quantum ghost imaging with a single-photon-sensitive time-stamping camera." *Optics Letters* **50**(2), 594-597 (2025).
3. **C. Li**, J. Upham, B. Braverman, and R. W. Boyd, "Violation of local realism with spatially multimode parametric down-conversion pumped by spatially incoherent light." *Physical Review A* **112**, 053726 (2025).
4. A. A. Aguilar-Cardoso, **C. Li**, T. J. B. Luck, M. F. Ferrer-García, J. Upham, J. S. Lundeen, and R. W. Boyd, "Tailoring spatial modes produced by stimulated parametric down-conversion." *Physical Review A* **112**(4), 043541 (2025).
5. T. Luck, A. A. Aguilar-Cardoso, **C. Li**, M. F. Ferrer-García, J. Upham, J. S. Lundeen, and R. W. Boyd, "Description of single-photon orbital angular momentum conjugation with stimulated parametric down-conversion [Invited]," *Journal of the Optical Society of America B* **43**, A37-A45 (2026).
6. A. A. Aguilar-Cardoso, **C. Li**, T. J. B. Luck, M. F. Ferrer-García, J. Upham, J. S. Lundeen, and R. W. Boyd, "All-optical turbulence mitigation for free-space quantum key distribution using stimulated parametric down-conversion." *Optica* **13**, 386-394 (2026).
7. M. C. Jabbari, **C. Li**, X. Liu, R. M. Córdova-Castro, B. Braverman, J. Upham, and R. W. Boyd, "Fast control of the transverse structure of a light beam using acousto-optic modulators." *Physical Review Applied* (*Accepted*).
8. **C. Li**, G. Kulkarni, I. Soward, Y. Zhang, J. Upham, D. England, A. Nomerotski, E. Karimi, and R. W. Boyd, "Full-field mapping of spatially varying polarization entanglement generated from spontaneous parametric down-conversion." *Physical Review Applied* (*Under review*).

9. **C. Li**, J. Brar, M. Küblböck, J. Upham, H. Fattahi, R. W. Boyd, "Generating quantum entanglement from sunlight" *Optica* (*Under review*).

Chapter 1

Background

Entanglement refers to the phenomenon that the joint state of two or more quantum systems cannot be written as the product of the states of individual constituent systems [1]. This feature has been exploited in many quantum applications, including quantum computation [2, 3], quantum communication [4, 5], and quantum sensing [6]. While entanglement can be created in various platforms, such as superconducting circuits [7, 8], trapped ions [9], and solid-state spins [10, 11], photons (particles of light) [12, 13] offer unique advantages that make them promising candidates for practical quantum applications [14]. As bosonic particles with zero electric charge, photons interact only extremely weakly with one another and rarely exchange energy with thermal or electromagnetic fields in the environment [15]. Consequently, photonic quantum systems are highly robust against decoherence and can maintain their quantum state over long distances and for extended periods. Entangled photon states are conventionally produced from nonlinear optical processes, such as spontaneous parametric down-conversion (SPDC) [16, 17, 18] and spontaneous four-wave mixing (SFWM) [19, 20]. In Fig. 1.1, we depict the schematics of generating entangled photons using SPDC and SFWM. In this thesis, we focus the discussion on SPDC-based entanglement generation.

In SPDC, a nonlinear medium interacts with a photon with a higher frequency and splits it into a pair of photons with lower frequencies. The higher-frequency photon is termed the *pump* photon, and the two lower-frequency photons are referred to as the *signal* and *idler* photons. The signal and idler photons can exhibit entanglement across all degrees of freedom (DoF) of light, including spatial, temporal-spectral, and polarization. Conventionally, lasers are chosen as the source of pump photons due to their high brightness. Since the photon conversion efficiency of SPDC (and nonlinear optical processes in general) is typically low, with one in about 10^8 pump photons getting down-converted [21]; thus, the high optical intensity provided by lasers is advantageous for generating entangled photons at practical rates. Second, lasers exhibit high optical coherence across all DoFs of light, namely, photons emitted from lasers are highly indistinguishable in terms of their spatial, temporal-spectral, and polarization modes [22]; this feature has been widely assumed to be indispensable for generating entanglement. Building on a series of successful demonstrations in laser-driven entanglement generation, studies on the applications of photonic quantum technologies have been expanding into their field deployment in areas of strategic importance, such as space [23] and the Arctic region [24]. Practical and large-scale implementation of quantum technologies in these scenarios often requires accommodation of the limited energy supplies and thermal management.

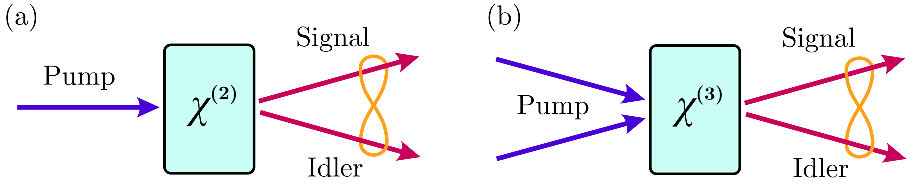

FIGURE 1.1: Schematic diagrams of photon entanglement generation using (a) SPDC and (b) SFWM, where $\chi^{(2)}$ and $\chi^{(3)}$ denote nonlinear media with second- and third-order optical nonlinearity, respectively.

However, at low driving current, lasers often fall short in their electrical-to-optical energy conversion efficiency (also referred to as the wall-plug efficiency η_{WPE}) compared to incoherent light sources, such as light-emitting diodes (LEDs). For instance, while GaN-based blue light LEDs can achieve up to $\eta_{\mathrm{WPE}} = 84\%$, studies on GaN-based laser diodes have typically reported $\eta_{\mathrm{WPE}} = 40\%$ [25]. This efficiency gap arises largely because lasers require population inversion to reach the lasing threshold, necessitating higher current densities. Furthermore, steady operation of laser devices often requires resource overheads such as optical stabilization and active thermal management, which exacerbate the already suboptimal energy utilization. These features could significantly limit the scalability and accessibility of photonic quantum technologies. Not to mention the manufacturing and maintenance costs that may render the exquisite laser devices less financially desirable for their practical implementations. Moreover, integrating laser-driven quantum devices with existing information and communication infrastructures could exacerbate the environmental issues, given that the classical information and communication technology sector already accounts for $\sim$ 1.8–3.9% of worldwide greenhouse gas emissions [26, 27]. This imminent bottleneck for photonic quantum technologies can potentially be resolved if one can generate entangled photons from nonlinear optical processes pumped by incoherent light sources. In other words, if the low optical coherence of the pump source does not fundamentally constrain the generation of high two-photon entanglement, one can employ more ubiquitous and energy-efficient light sources, such as LEDs, or even natural sources of light, such as sunlight, to facilitate the development of scalable and environmentally friendly photonic quantum technologies.

The role of pump coherence in SPDC-based entanglement generation turns out to be manifold. On one hand, earlier studies indicate that the coherence of the pump beam in a given DoF sets an upper bound for the two-photon entanglement produced in that same DoF [28, 29, 30, 31, 32, 33, 34, 35, 36, 37]. For instance, Zhang et al. [32] have experimentally demonstrated that the degree of spatial entanglement in the position-momentum basis decreases as the spatial coherence of the pump beam is reduced. In particular, they showed that when SPDC is driven by spatially incoherent light emitted by an LED, the spatial correlation between down-converted photons becomes so weak that position-momentum entanglement vanishes. The mechanism is almost intuitive: when the pump photons are emitted from highly incoherent light sources, they are distinguishable in terms of their spatial properties; the down-conversion events driven by these distinguishable pump photons then generate distinguishable photon pairs, which, by definition cannot exhibit spatial entanglement as two-photon quantum states.

On the other hand, incoherence in a given DoF does not necessarily translate to non-entanglement in a different DoF. For instance, a light beam propagating through atmospheric turbulence may exhibit reduced spatial coherence while remaining perfectly polarized. Based on our earlier discussions, this perfectly polarized pump beam allows for the generation of maximum polarization entanglement via SPDC. However, the influence of its low spatial coherence on the generation of polarization entanglement remains unclear. Therefore, fully understanding the role of pump coherence in SPDC-based entanglement generation then requires answering a crucial question:

> Does the coherence of the pump beam in a given DoF affect the two-photon entanglement produced in a **different** DoF?

In this thesis, we present a series of experimental works that aim to address a specific aspect of this question, that is

> Can **spatially/temporally incoherent** light sources produce highly **polarization-entangled** two-photon state as lasers do ?

This chapter provides sufficient technical background for understanding the works presented in this thesis. In Section 1.1, we introduce the concept of quantum entanglement. In Section 1.2, we review common metrics for characterizing the entanglement in a two-photon state, including violation of local realism, concurrence, and Schmidt number, which can be generalized to characterize arbitrary bipartite systems. In Section 1.3, we discuss the principles of SPDC in the context of classical and quantum nonlinear optics. In Section 1.4, we derive the generation of a two-photon state from the quantum mechanical model of SPDC. In Section 1.5, we discuss the relation between the degree of polarization of the pump beam and the two-photon polarization entanglement generated from SPDC, which serves as an example of the influence of pump coherence on the entanglement of the down-converted photons. In Section 1.6, we summarize the structure of this thesis.

1.1 Introduction to quantum entanglement

In 1935, Einstein, Podolsky, and Rosen (EPR) conceived a thought experiment, which is now known as the "EPR paradox", to challenge the completeness of the quantum-mechanical description of physical reality [38]. To EPR, a sufficient condition for reality states that one should be able to predict with certainty the value of a physical quantity, without disturbing a system. One can now consider two systems, A and B, that have undergone some initial interactions, so that their joint position and momentum can be predicted with certainty. The two systems are then separated so they can no longer interact, and their individual positions and momenta can be determined only from subsequent measurements. As a result, by taking measurements on the system A in the position basis, one can predict, through the initial joint position of A and B, the position of B, x_B, with certainty. Since the two systems no longer interact, measuring A does not disturb B. Therefore, according to EPR's definition for reality, x_B must be the physical reality of B. Alternatively, one can also choose to measure system A in the momentum basis, thereby assigning the momentum of B, p_B, as the physical reality of B. However, since the position and momentum of the same system correspond to two noncommuting observables, the quantum theory also requires that system B cannot have x_B and p_B simultaneously as its physical reality. This paradox has led EPR to believe that quantum theory cannot account for every element of reality, namely, that quantum-mechanical descriptions of physical reality are incomplete. Inspired by these arguments, Erwin Schrödinger coined the term "entanglement", which he translated from the original German word "Verschränkung", to refer to the phenomena that give rise to the EPR paradox [39]. In Chapter 3, we have used the uncertainty in the joint measurements of position and momentum bases to observe a EPR-type entanglement between photons.

In 1964, Bell discussed the EPR paradox in the context of local hidden-variable theories, which had been proposed to supplement the quantum theory [40]. Bell identified an implicit yet crucial assumption in the EPR argument: that operations on system A do not instantaneously affect a distant system B. This is commonly known as the principle of locality. It then follows that the results of any measurements are predetermined by an additional parameter that locally influences the system. Bell showed that, if the correlations between two systems are modelled with a local hidden-variable theory, the expectation values of joint measurements on these two systems must satisfy a certain inequality. However, quantum entanglement between different systems can allow the results of joint measurements to violate this inequality. In the existing literature, such a violation is sometimes also referred to as a violation of "local realism" because satisfying Bell's inequality means respecting both the principle of locality and EPR's definition of reality. Violation of Bell's inequality has since been widely used as a test of quantum nonlocality and as a witness of quantum entanglement.

1.2 Metrics for characterizing quantum entanglement

1.2.1 Violation of Bell's inequality

The original inequality derived by Bell has been reformulated in various ways to facilitate experimental studies. One of the most commonly used forms of Bell's inequality is due to Clauser, Horne, Shimony, and Holt (CHSH) [41].

Consider a simplified version of the EPR scenario in which the systems A and B are both defined in a two-dimensional Hilbert space (e.g., the spin states of electrons or the polarization states of photons). One can measure system A using either one of two observables, a or a', while another observer can measure system B using b or b'. Suppose that the outcomes of measuring a, a', b, b' take values in $\{\pm 1\}$, we can define the random variable S:

$$S = ab + a'b + ab' - a'b', \tag{1.1}$$

such that in any local hidden variable theory, the expectation value of this quantity is bounded by:

$$|\langle S \rangle| = |\langle ab \rangle + \langle a'b \rangle + \langle ab' \rangle - \langle a'b' \rangle| \leq 2. \tag{1.2}$$

However, for a quantum-entangled state, the expectation value can violate this bound. The maximum possible violation is given by Cirel'son's inequality [42]:

$$|\langle S \rangle| \leq 2\sqrt{2}. \tag{1.3}$$

In Chapters 4 and 5, we have adopted the CHSH formalism of Bell's inequality to characterize the polarization entanglement generated from SPDC.

1.2.2 Concurrence

It is important to note that the violation of a Bell-type inequality is a sufficient but unnecessary condition for entanglement. For instance, some mixed quantum states, such as the Werner state, can exhibit entanglement while being compatible with a local hidden variable model [43]. In contrast, concurrence $C(\rho)$ unambiguously quantifies the entanglement of an arbitrary two-qubit state with a density matrix written as ρ [44]. The concurrence is defined as:

$$C(\rho) = \max\{0, \sqrt{\Lambda_1} - \sqrt{\Lambda_2} - \sqrt{\Lambda_3} - \sqrt{\Lambda_4}\}, \tag{1.4}$$

where Λ_i's are the eigenvalues of the matrix $R = \rho\tilde{\rho}$ in descending order. Here, $\tilde{\rho}$ is defined as

$$\tilde{\rho} = (\sigma_y \otimes \sigma_y)\rho^*(\sigma_y \otimes \sigma_y), \tag{1.5}$$

where ρ^* is the complex conjugate of ρ and σ_y is the Pauli-Y matrix. The concurrence ranges from 0 to 1, where $C(\rho) = 0$ indicates that the state is separable (unentangled) and $C(\rho) = 1$ represents maximum entanglement. The following intuition may help understand the concept of concurrence. The operation in Eq. 1.5 conducts a "spin-flip" on each constituent qubit of the two-qubit state described by ρ, which converts each qubit into its orthogonal state. R can then be seen as characterizing the overlap between ρ and its spin-flipped counterpart $\tilde{\rho}$. If a two-qubit state is separable, the overlap of the two density matrices is equivalent to the product of the overlap between each qubit and its spin-flipped counterpart, which is 0 due to orthogonality. In contrast, if the two-qubit state is completely non-separable (maximally entangled), performing a spin-flip on each constituent qubit converts the two-qubit state into an identical one, which indicates complete overlap between ρ and $\tilde{\rho}$. We have used concurrence $C(\rho)$ in Chapters 2-5 to quantify the polarization entanglement generated from SPDC.

While violation of Bell's inequality mostly acts as a "witness" for entanglement, concurrence reveals the "degree of entanglement" and thus allows for a more accurate quantification of the entanglement in a two-qubit state. On the other hand, since violation of Bell's inequality can certify the security of quantum communication protocols [5], it can often serve as a more practical metric than concurrence for benchmarking the performance of experimental quantum devices.

1.2.3 Schmidt number

We have shown that Bell-type inequalities and the concurrence are excellent metrics for characterizing the entanglement of two-qubit states. While they can be generalized to characterize entangled states with dimensionalities larger than 2, the Schmidt number provides a more intuitive picture for quantifying the entanglement of a bipartite pure state with arbitrary dimensionality. Consider two systems A and B defined in Hilbert spaces $\mathcal{H}_A$ and $\mathcal{H}_B$, respectively. Then for any pure bipartite state $|\psi\rangle_{AB}$ defined in the tensor product space $\mathcal{H}_A \otimes \mathcal{H}_B$, there exist orthonormal bases $\{|i\rangle_A\}$ and $\{|i'\rangle_B\}$ for $\mathcal{H}_A$ and $\mathcal{H}_B$, respectively, such that the state can be expressed in the Schmidt decomposition:

$$|\psi\rangle_{AB} = \sum_i \sqrt{\lambda_i} |i\rangle_A \otimes |i'\rangle_B, \tag{1.6}$$

where $\lambda_i \geq 0$ are real coefficients satisfying $\sum \lambda_i = 1$.

The Schmidt number is defined as the effective number of non-zero coefficients in this decomposition. A state is entangled if and only if its Schmidt number is greater than 1. Furthermore, the Schmidt number characterizes the *dimensionality* of the entanglement. If the Schmidt number is K, the state effectively resides in a $K \times K$ Hilbert space. At $K > 2$, the system behaves as a pair of K-dimensional qudits rather than simple qubits ($K = 2$). This is particularly relevant for spatially and temporally entangled states that typically reside in high-dimensional Hilbert spaces. In Chapter 3, we certify the dimensionality of spatial entanglement generated from SPDC by estimating a lower bound for the Schmidt number.

1.3 Principles of SPDC

We begin this chapter by clarifying the relations between different physical attributes of the pump photon and the down-converted photon pairs—signal and idler. The term "down-conversion" denotes the reduction in frequency, and thus energy, of individual photons after the interaction, while the total photon energy is conserved. Since the initial and final states of the nonlinear medium are identical, the SPDC process is considered "parametric", as opposed to "non-parametric" processes in which population in one energy level is transferred to another. A simple example of a non-parametric process is two-photon absorption, in which an atom is excited to a higher energy level after simultaneously absorbing the energy of two photons. In addition to energy conservation, the total photon momentum is also conserved in SPDC. Namely, the wavevector of the pump photon is equal to the vector sum of the wavevectors of the signal and the idler photons. Fig. 1.2 depicts the diagrams for energy and momentum conservation in SPDC.

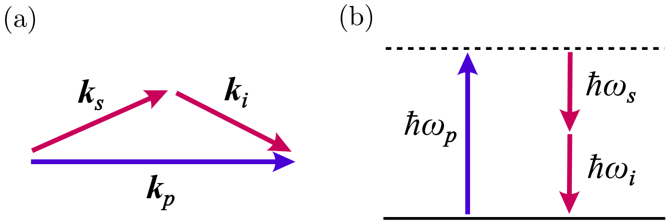

FIGURE 1.2: (a) Diagram of the relations between wavevectors of interacting photons in SPDC, where $\boldsymbol{k}_{s(i)}$ denotes the frequency of the signal(idler) photon (b) Energy-level diagram of SPDC, in which the solid and dashed lines represent real and virtual energy levels, respectively, and $\omega_{s(i)}$ denotes the frequency of the signal(idler) photon. When a photon in the pump beam is annihilated in SPDC, its energy is transferred to the generated signal and idler photons. As a result, the total photon energy is conserved, and the quantum state of the system remains unchanged.

The requirement for energy and momentum conservation in SPDC is often jointly referred to as the *phase-matching condition*. For a given nonlinear medium, the polarization, frequency, and propagation directions of the interacting photons must satisfy certain relations to achieve the phase-matching condition required for SPDC. Based on these relations, SPDC can be classified into several different categories. In terms of polarization relations, Type-0 phase-matching requires all interacting photons to be in the same polarization[1]; Type-I phase-matching demands that the polarization of the pump photon is orthogonal to that of the signal and the idler photons (which in turn requires

---

[1] It is important to note that Type-0 phase-matching is in general not possible in bulk nonlinear crystals but can be introduced in periodically poled crystals through quasi-phase-matching, see, for example, Myers et al. (1995)[45]

that the signal and idler photons have the same polarization); Type-II phase-matching dictates that the signal and idler have orthogonal polarizations. Regarding frequency relations, the phase-matching is "degenerate" when the signal and the idler have the same frequency; otherwise, it is "non-degenerate". With respect to propagation directions, the case in which the signal and idler propagate in the same direction is called "collinear" phase-matching; while the converse is termed "non-collinear". We have summarized these phase-matching categories in Table 1.1.

Table 1.1: Categories of SPDC based on polarization and frequency relations between interacting beams. "$a \parallel b$" and "$a \perp b$" denote that the polarization of a and b are parallel or orthogonal, respectively; $\hat{\kappa}_{s(i)}$ represents the unit vector in the propagation direction of the siganl(idler) photon.

Category	**Condition**	**Term**
Polarization	pump $\parallel$ signal $\parallel$ idler	Type-0
	pump $\perp$ (signal $\parallel$ idler)	Type-I
	signal $\perp$ idler	Type-II
Frequency	$\omega_s = \omega_i$	Degenerate
	$\omega_s \neq \omega_i$	Non-degenerate
Direction	$\hat{\kappa}_s = \hat{\kappa}_i$	Collinear
	$\hat{\kappa}_s \neq \hat{\kappa}_i$	Non-collinear

Having established the conceptual understandings of SPDC, we now present its analytical description using the theories of nonlinear optics.

1.3.1 Fundamentals of nonlinear optics

When an optical field is incident on an atom, the electrons in this atom experience two competing forces: the Coulomb force from the nucleus and that from the external optical field. These forces displace the electrons from their equilibrium positions, resulting in a net electric dipole moment in the atom. In an ensemble of such atoms, the volumetric density of these electric dipole moments is defined as the electric polarization[2]. The founding principle of nonlinear optics states that, in general, the induced electric polarization $\mathbf{P}(\mathbf{r}, t)$ at position $\mathbf{r}$ and time t is described by a power series expansion in terms of the external optical field $\mathbf{E}(\mathbf{r}, t)$. Each constituent component of the vectorial electric polarization field is written as [46]

$$P_j(\mathbf{r}, t) = \epsilon_0 \Big[\chi^{(1)}_{jk} E_k(\mathbf{r}, t) + \chi^{(2)}_{jkl} E_k(\mathbf{r}, t) E_l(\mathbf{r}, t) + \chi^{(3)}_{jklm} E_k(\mathbf{r}, t) E_l(\mathbf{r}, t) E_m(\mathbf{r}, t) + \dots \Big], \tag{1.7}$$

---

[2] This term is commonly referred to as just "polarization". To avoid confusion with the polarization of light, which describes the oscillation direction of an optical field, we have explicitly written it as "electric polarization" to clarify the distinction.

where ϵ_0 is the permittivity of free space, $\chi^{(n)}$ represents the n-th order susceptibility tensor, which characterizes the anisotropic nature of commonly used nonlinear crystals. Subscripts of P and E represent field components oscillating along different principal axes of the crystal.

At weak field strengths, second- and higher-order terms in Eq. 1.7 are much smaller compared to the first-order one, so that the induced polarization can be seen as linearly proportional to the applied optical field. This regime is thus called the linear optics regime. In this case, the induced electric polarization is written as

$$P_j^{(1)}(\mathbf{r},t) = \epsilon_0 \chi_{jk}^{(1)} E_k(\mathbf{r},t), \tag{1.8}$$

where $\chi_{jk}^{(1)}$ is explicitly referred to as linear susceptibility.

At sufficiently strong field strengths, the higher-order terms in Eq. 1.7 become non-negligible. Consequently, the induced polarization displays a nonlinear response to the applied optical field. In this thesis, we shall focus on the nonlinear response that is governed by the second-order term of Eq. 1.7, namely,

$$P_j^{(2)}(\mathbf{r},t) = \epsilon_0 \chi_{jkl}^{(2)} E_k(\mathbf{r},t) E_l(\mathbf{r},t), \tag{1.9}$$

Here, $\chi_{jkl}^{(2)}$ is explicitly referred to as the second-order nonlinear optical susceptibility. It is important to note that second-order nonlinear effects only appear in non-centrosymmetric materials since the inversion symmetry in materials results in $\chi^{(2)} = 0$.

In classical electromagnetic theories, the contribution of a second-order nonlinear interaction, such as SPDC, to the energy of an electromagnetic field $H(t)$ is given by integrating the product of $\mathbf{P}^{(2)}(\mathbf{r},t)$ and $\mathbf{E}(\mathbf{r},t)$ over the volume $\mathcal{V}$ of the nonlinear medium, which can be explicitly written as

$$H(t) = \epsilon_0 \int_{\mathcal{V}} d\mathbf{r}\, \chi_{jkl}^{(2)} E_k(\mathbf{r},t) E_l(\mathbf{r},t) E_m(\mathbf{r},t). \tag{1.10}$$

While certain studies have successfully explained the second-order correlations within the signal (idler) field by modelling SPDC as classical difference-frequency generation between a pump beam and a stochastic "vacuum" seed field [47], studying the correlations between the signal and idler photons requires a quantum-mechanical description of SPDC.

1.3.2 Quantum mechanical description of SPDC

In the quantum model of SPDC, describing the creation of signal and idler photons requires that the corresponding electric fields become quantized and are written as field operators $\hat{E}(\mathbf{r},t)$. In general, $\hat{E}(\mathbf{r},t)$ can be decomposed into positive-frequency components $\hat{E}^{(+)}(\mathbf{r},t)$ and negative-frequency components $\hat{E}^{(-)}(\mathbf{r},t)$:

$$\hat{E}(\mathbf{r},t)=\hat{E}^{(+)}(\mathbf{r},t)+\hat{E}^{(-)}(\mathbf{r},t), \tag{1.11}$$

where $\hat{E}^{(+)}(\mathbf{r},t)$ and $\hat{E}^{(-)}(\mathbf{r},t)$ are associated with the annihilation and the creation of a photon, respectively. The interaction Hamiltonian accounting for the SPDC process, which describes the annihilation of a pump photon for the creation of a signal photon and an idler photon, is thus rewritten from Eq. 1.10 as:

$$\hat{H}(t)=\epsilon_0\chi^{(2)}\int_{\mathcal{V}}d\mathbf{r}\,E_p(\mathbf{r},t)\hat{E}_s^{(-)}(\mathbf{r},t)\hat{E}_i^{(-)}(\mathbf{r},t)+H.c., \tag{1.12}$$

where $H.c.$ denotes the Hermitian conjugate, and we have assigned well-defined polarizations to each field and thus written them in the scalar form, with subscripts p, s, and i denoting pump, signal, and idler, respectively. We have also assumed that $\chi^{(2)}$ can be approximated as a constant over the frequency range of interest so that it can be taken out of the integral. Additionally, we have further simplified the expressions by describing the pump field using the classical field amplitude $E_p(\mathbf{r},t)$ instead of a field operator $\hat{E}_p(\mathbf{r},t)$. We reached this approximation by assuming the pump beam remains strong before and after the nonlinear interaction, since only a small fraction of the pump photons are down-converted into signal-idler photon pairs. In the limit that the quantization volume goes to infinity, we can write the summations of discrete spatiotemporal modes of electric fields as an integral. The electric fields are thus explicitly given as [48]

$$E_p(\mathbf{r},t)=A_p\iint d\boldsymbol{q}_p d\omega_p E(\boldsymbol{q}_p,\omega_p)e^{i(\boldsymbol{q}_p\cdot\boldsymbol{\rho}+k_{pz}z-\omega_p t)}, \tag{1.13}$$

$$\hat{E}_s^{(-)}(\mathbf{r},t)=A_s^*\iint d\boldsymbol{q}_s d\omega_s \hat{a}^\dagger(\boldsymbol{q}_s,\omega_s)e^{-i(\boldsymbol{q}_s\cdot\boldsymbol{\rho}+k_{sz}z-\omega_s t)}, \tag{1.14}$$

$$\hat{E}_i^{(-)}(\mathbf{r},t)=A_i^*\iint d\boldsymbol{q}_i d\omega_i \hat{a}^\dagger(\boldsymbol{q}_i,\omega_i)e^{-i(\boldsymbol{q}_i\cdot\boldsymbol{\rho}+k_{iz}z-\omega_i t)}, \tag{1.15}$$

where we have separated the position vector into transverse and longitudinal components, $\mathbf{r}=(\boldsymbol{\rho},z)$; similarly, $\boldsymbol{q}_j$ and k_{jz} represent the transverse components of wavevectors, longitudinal components of wavevectors and optical frequencies, respectively, and ω_j's are optical frequencies, with $j=p,s,i$. In the experimental situations studied in this thesis, the coefficients of quantized electric fields A_j vary slowly over the frequency range of interest. Therefore, we have approximated them as constants and moved them out of the integrals. By substituting Eq. 1.13, 1.14 and 1.15 into Eq. 1.12, we obtain

$$\begin{aligned}\hat{H}(t)=&\,\epsilon_0\chi^{(2)}A_pA_s^*A_i^*\iint d\boldsymbol{\rho}dz\iiint d\omega_p d\omega_s d\omega_i\iiint d^2\boldsymbol{q}_p d^2\boldsymbol{q}_s d^2\boldsymbol{q}_i\\&\times E(\boldsymbol{q}_p,\omega_p)\hat{a}^\dagger(\boldsymbol{q}_s,\omega_s)\hat{a}^\dagger(\boldsymbol{q}_i,\omega_i)\\&\times\exp\left[i(\boldsymbol{q}_p-\boldsymbol{q}_s-\boldsymbol{q}_i)\boldsymbol{\rho}+i(k_{pz}-k_{sz}-k_{iz})z+i(\omega_s+\omega_i-\omega_p)t\right]+H.c.,\end{aligned} \tag{1.16}$$

where we have substituted $\int_{\mathcal{V}} d\mathbf{r} = \iint d\boldsymbol{\rho} dz$.

1.4 Two-photon state generated from SPDC

We now derive the expression of the two-photon state generated from SPDC. We consider a nonlinear crystal with length L. Before the nonlinear interaction, which starts at $t = 0$, the initial two-photon state of the signal-idler photon pair is given by a joint vacuum state $|\psi(t = 0)\rangle = |vac\rangle_s |vac\rangle_i$. After the interaction ends at $t = t_0$, the evolution of this two-photon state due to the nonlinear interaction is described by the Schrödinger equation and given by:

$$\begin{aligned} |\psi(t_0)\rangle &= \exp\left[\frac{1}{i\hbar}\int_0^{t_0} dt \hat{H}(t)\right] |vac\rangle_s |vac\rangle_i \\ &\approx \left[1 + \frac{1}{i\hbar}\int_0^{t_0} dt \hat{H}(t)\right] |vac\rangle_s |vac\rangle_i, \end{aligned} \tag{1.17}$$

where we have approximated the perturbation expansion using its first two terms, assuming that the nonlinear interactions governing SPDC are weak. The first term is the initial vacuum state. The second term describes the resulting two-photon state generated from SPDC, which, by substituting Eq. 1.16 into Eq. 1.17, is written as

$$\begin{aligned} |\psi\rangle = A &\int_0^{t_0} dt \iint d\boldsymbol{\rho} dz \iiint d\omega_p d\omega_s d\omega_i \iiint d\boldsymbol{q}_p d\boldsymbol{q}_s d\boldsymbol{q}_i \\ &\times \exp\left[i(\boldsymbol{q}_p - \boldsymbol{q}_s - \boldsymbol{q}_i)\boldsymbol{\rho} + i(k_{pz} - k_{sz} - k_{iz})z + i(\omega_s + \omega_i - \omega_p)t\right] \\ &\times E(\boldsymbol{q}_p, \omega_p)\hat{a}^\dagger(\boldsymbol{q}_s, \omega_s)\hat{a}^\dagger(\boldsymbol{q}_i, \omega_i)|vac\rangle_s |vac\rangle_i, \end{aligned} \tag{1.18}$$

where we have absorbed all constants into the normalization factor A. Note that we have omitted the contribution from the Hermitian conjugate term in Eqn. 1.16 since $\hat{a}|vac\rangle = 0$. To simplify the above expression, we also make the following approximations:

Firstly, we assume that the interaction time t_0 is much longer than the time required for a single SPDC event and much shorter than the time interval between consecutive SPDC events. Doing so allows us to extend the time integration limits to $-\infty$ and $+\infty$, so that

$$\int_0^{t_0} dt \exp\left[i(\omega_s + \omega_i - \omega_p)t\right] \approx \int_{-\infty}^{+\infty} dt \exp\left[i(\omega_s + \omega_i - \omega_p)t\right] = \delta(\omega_s + \omega_i - \omega_p). \tag{1.19}$$

Secondly, we assume that the transverse area of the nonlinear crystal is much larger than that of the pump field, so that the transverse space integral is written as

$$\int_{-\infty}^{+\infty} d\boldsymbol{\rho} \exp\left[i(\boldsymbol{q}_p - \boldsymbol{q}_s - \boldsymbol{q}_i)\boldsymbol{\rho}\right] = \delta(\boldsymbol{q}_p - \boldsymbol{q}_s - \boldsymbol{q}_i). \tag{1.20}$$

We now evaluate the result of the longitudinal space integral as

$$\int_{-L/2}^{+L/2} dz \exp\left[i\Delta k_z z\right] = L\mathrm{sinc}\left(\frac{\Delta k_z L}{2}\right), \tag{1.21}$$

where we have substituted $\Delta k_z = k_{pz} - k_{sz} - k_{iz}$. Eq. 1.21 is called the phase-matching function. The action of creation operators on vacuum states is given by

$$\hat{a}^{\dagger}(\boldsymbol{q}_s, \omega_s)\hat{a}^{\dagger}(\boldsymbol{q}_i, \omega_i)|vac\rangle_s|vac\rangle_i = |\boldsymbol{q}_s, \omega_s\rangle|\boldsymbol{q}_i, \omega_i\rangle, \tag{1.22}$$

where we have omitted the subscripts of the resulting state vectors since the signal and idler photons are now explicitly labelled by their transverse wavevectors and frequencies. By substituting the results in Eq. 1.19- 1.22 into Eq. 1.18 and take the integration over $(\boldsymbol{q}_p, \omega_p)$, we write the resulting two-photon state as

$$|\psi\rangle = A\iint d\omega_s d\omega_i \iint d\boldsymbol{q}_s d\boldsymbol{q}_i \mathrm{sinc}\left(\frac{\Delta k_z L}{2}\right) E(\boldsymbol{q}_p, \omega_p)|\boldsymbol{q}_s, \omega_s\rangle|\boldsymbol{q}_i, \omega_i\rangle \tag{1.23}$$

where $\boldsymbol{q}_p = \boldsymbol{q}_s + \boldsymbol{q}_i, \omega_p = \omega_s + \omega_i$, and we have absorbed the constant crystal length L from Eq. 1.21 into A. This state is now written explicitly in the spatial (transverse momenta) and temporal-spectral (frequency) DoFs, while the polarization relations between pump, signal, and idler are implied by the phase-matching type, which is given in Table 1.1. For instance, consider a nonlinear crystal made for Type-I phase-matching, such that a vertically (V) polarized pump photon is down-converted into a pair of horizontally (H) polarized photons. The two-photon state is then written as

$$|\psi\rangle = A\iint d\omega_s d\omega_i \iint d\boldsymbol{q}_s d\boldsymbol{q}_i \mathrm{sinc}\left(\frac{\Delta k_z L}{2}\right) E_V(\boldsymbol{q}_p, \omega_p)|H, \boldsymbol{q}_s, \omega_s\rangle|H, \boldsymbol{q}_i, \omega_i\rangle. \tag{1.24}$$

Alternatively, a H-polarized pumped photon can be down-converted into a pair of V-polarized photons. Summing up the two alternatives in the polarization DoF, the two-photon state is now written as

$$\begin{aligned}|\psi\rangle = A\iint d\omega_s d\omega_i \iint d\boldsymbol{q}_s d\boldsymbol{q}_i \mathrm{sinc}\left(\frac{\Delta k_z L}{2}\right) \\ \times \left[E_V(\boldsymbol{q}_p, \omega_p)|H, \boldsymbol{q}_s, \omega_s\rangle|H, \boldsymbol{q}_i, \omega_i\rangle + E_H(\boldsymbol{q}_p, \omega_p)|V, \boldsymbol{q}_s, \omega_s\rangle|V, \boldsymbol{q}_i, \omega_i\rangle\right].\end{aligned} \tag{1.25}$$

Eq. 1.25 then allows us to study the influence of coherence of the pump on the entanglement between down-converted photons across any two DoFs. The quantum mechanical properties of this two-photon state, including entanglement, are fully described by its density matrix $\rho := \langle|\psi\rangle\langle\psi|\rangle$, where $\langle\cdots\rangle$ denotes an ensemble average over many realizations of the pump field. The density matrix is written as

$$
\begin{aligned}
\rho = |A|^2 \iiiint d\boldsymbol{q}_s d\boldsymbol{q}_i d\boldsymbol{q}'_s d\boldsymbol{q}'_i \iiiint d\omega_s d\omega_i d\omega'_s d\omega'_i \, \mathrm{sinc}\left(\frac{\Delta k_z L}{2}\right)\mathrm{sinc}\left(\frac{\Delta k'_z L}{2}\right) \\
\times \Big[\langle E_V(\boldsymbol{q}_p,\omega_p)E^*_V(\boldsymbol{q}'_p,\omega'_p)\rangle |H,\boldsymbol{q}_s,\omega_s\rangle|H,\boldsymbol{q}_i,\omega_i\rangle\langle H,\boldsymbol{q}'_s,\omega'_s|\langle H,\boldsymbol{q}'_i,\omega'_i| \\
+ \langle E_V(\boldsymbol{q}_p,\omega_p)E^*_H(\boldsymbol{q}'_p,\omega'_p)\rangle |H,\boldsymbol{q}_s,\omega_s\rangle|H,\boldsymbol{q}_i,\omega_i\rangle\langle V,\boldsymbol{q}'_s,\omega'_s|\langle V,\boldsymbol{q}'_i,\omega'_i| \\
+ \langle E_H(\boldsymbol{q}_p,\omega_p)E^*_V(\boldsymbol{q}'_p,\omega'_p)\rangle |V,\boldsymbol{q}_s,\omega_s\rangle|V,\boldsymbol{q}_i,\omega_i\rangle\langle H,\boldsymbol{q}'_s,\omega'_s|\langle H,\boldsymbol{q}'_i,\omega'_i| \\
+ \langle E_H(\boldsymbol{q}_p,\omega_p)E^*_H(\boldsymbol{q}'_p,\omega'_p)\rangle |V,\boldsymbol{q}_s,\omega_s\rangle|V,\boldsymbol{q}_i,\omega_i\rangle\langle V,\boldsymbol{q}'_s,\omega'_s|\langle V,\boldsymbol{q}'_i,\omega'_i|\Big].
\end{aligned} \tag{1.26}
$$

1.5 Influence of pump coherence on two-photon entanglement

The optical coherence describes the stability of the relative phase between two field components. In the spatial and temporal-spectral DoF, this is quantified by the cross-correlation between electric field components at different positions and time $(\mathbf{r},\mathbf{r}';t,t')$, which is written as

$$\Gamma(\mathbf{r},\mathbf{r}';t,t') = \langle E(\mathbf{r},t)E^*(\mathbf{r}',t')\rangle. \tag{1.27}$$

We recall that, similar to Eqn. 1.13-1.15, $E(\mathbf{r},t)$ can be written as a Fourier integral with respect to the transverse momenta and frequency variables:

$$E(\mathbf{r},t) = \iint d\boldsymbol{q}d\omega E(\boldsymbol{q},\omega)e^{i(\boldsymbol{q}\cdot\boldsymbol{\rho}+k_z z-\omega t)}. \tag{1.28}$$

Therefore, the elements of the density matrix in Eqn. 1.26 $\langle E(\boldsymbol{q}_p,\omega_p)E^*(\boldsymbol{q}'_p,\omega'_p)\rangle$ characterize the coherence of the pump beam in its spatial and temporal-spectral DoFs.

In the polarization DoF, the coherence of the pump field can be described by a covariance matrix in terms of its horizontal and vertical electric field components, which is given by [22]

$$J = \begin{bmatrix} \langle E_V E^*_V\rangle & \langle E_V E^*_H\rangle \\ \langle E_H E^*_V\rangle & \langle E_H E^*_H\rangle \end{bmatrix} = \begin{bmatrix} |E_V|^2 & J_{VH} \\ J^*_{VH} & |E_H|^2 \end{bmatrix}, \tag{1.29}$$

where we have substituted $\langle E_k E^*_k\rangle = \langle |E_k|^2\rangle = |E_k|^2$ and $J_{HV} = \langle E_H E^*_V\rangle = \langle E_V E^*_H\rangle^* = J^*_{VH}$. Note that, in principle, E_H, E_V can be replaced by any two mutually orthogonal electric field components, and we have used the horizontal and vertical components to align the notations with the derivations in this section.

The degree of polarization P, which is the “polarization coherence”, of the pump beam can then be calculated from J using [49]

$$P = \sqrt{1 - \frac{4\mathrm{Det}(J)}{[\mathrm{Tr}(J)]^2}}, \tag{1.30}$$

where $\mathrm{Det}(J) = |E_V|^2|E_H|^2 - |J_{VH}|^2$ denotes the determinant of J, and $\mathrm{Tr}(J) = |E_V|^2 + |E_H|^2 = 1$ denotes its trace. Consequently, Eq. 1.30 can be explicitly written as

$$P = \sqrt{(|E_V| - |E_H|)^2 + 4|J_{VH}|^2}. \tag{1.31}$$

In the following discussions, we give a detailed example of how the coherence of the pump beam in a given DoF puts an upper bound on the entanglement in that same DoF. Since this thesis primarily considers the generation of polarization entanglement, we demonstrate this principle by deriving the relation between the degree of polarization of the pump and the polarization entanglement of the down-converted photons, and the cases for spatial and temporal-spectral DoFs should follow. For detailed treatments of the analytical relations between the spatial(temporal-spectral) coherence of the pump and the spatial(temporal-spectral) entanglement of the down-converted photons, one may refer to Ref. [28, 29, 30, 34, 35].

In most experimental studies regarding the generation of polarization entanglement, the target state contains only one of the two possible correlation patterns: (i) correlation in parallel polarizations $\{|H\rangle_s|H\rangle_i, |V\rangle_s|V\rangle_i\}$, which is produced from Type-I or Type-0 SPDC, or (ii) correlations in orthogonal polarizations $\{|H\rangle_s|V\rangle_i, |V\rangle_s|H\rangle_i\}$, which is produced from Type-II SPDC. Therefore, it is sufficient to focus our discussion on two-qubit states displaying only one of these correlation types. For a detailed treatment of the general case of the two-qubit polarization entanglement, one may refer to Ref. [35].

Consider a case in which the two-photon state Eq. 1.25 has well-defined transverse momenta $(\boldsymbol{q}_s, \boldsymbol{q}_i)$ and frequencies (ω_s, ω_i), such that the integration over $\boldsymbol{q}_s, \boldsymbol{q}_i, \omega_s, \omega_i$ can be ignored. Additionally, we can reduce the phase-matching function to a constant, which can be absorbed into the electric field amplitudes of the pump beam E_H and E_V, together with the normalization factor A. The normalized two-photon polarization state is thus written as

$$|\psi\rangle = E_V|HH\rangle + E_H|VV\rangle, \quad |E_V|^2 + |E_H|^2 = 1 \tag{1.32}$$

where we have used a compact notation of a joint signal-idler state $|si\rangle := |s\rangle|i\rangle$.

We quantify the polarization entanglement of Eq. 1.32 by calculating the concurrence $C(\rho)$ of its density matrix ρ, which is reduced from Eqn. 1.26 to

$$\begin{aligned}\rho = {} & \langle E_V E_V^*\rangle|HH\rangle\langle HH| + \langle E_V E_H^*\rangle|HH\rangle\langle VV| \\ & + \langle E_H E_V^*\rangle|VV\rangle\langle HH| + \langle E_H E_H^*\rangle|VV\rangle\langle VV|.\end{aligned} \tag{1.33}$$

Note that we can perform similar substitutions as in Eq. 1.29 and write the matrix form of Eq. 1.33 in the computational basis $\{|HH\rangle, |HV\rangle, |VH\rangle, |VV\rangle\}$ as

$$\rho = \begin{bmatrix} |E_V|^2 & 0 & 0 & J_{VH} \\ 0 & 0 & 0 & 0 \\ 0 & 0 & 0 & 0 \\ J_{VH}^* & 0 & 0 & |E_H|^2 \end{bmatrix}. \tag{1.34}$$

We can now calculate the concurrence of this density matrix using the definitions given in Section 1.2.2. The product of ρ and its "spin-flipped" counterpart $\tilde{\rho}$ is written as

$$R = \rho\tilde{\rho} = \begin{bmatrix} |E_V|^2|E_H|^2+|J_{VH}|^2 & 0 & 0 & 2|E_V|^2 J_{VH} \\ 0 & 0 & 0 & 0 \\ 0 & 0 & 0 & 0 \\ 2|E_H|^2 J_{VH}^* & 0 & 0 & |E_V|^2|E_H|^2+|J_{VH}|^2 \end{bmatrix}. \tag{1.35}$$

Such a matrix has the following eigenvalues, which we write in descending order

$$\begin{aligned} \Lambda_1 &= (|E_V||E_H|+|J_{VH}|)^2, \\ \Lambda_2 &= (|E_V||E_H|-|J_{VH}|)^2, \\ \Lambda_3 &= 0, \\ \Lambda_4 &= 0. \end{aligned} \tag{1.36}$$

Therefore, the concurrence of a two-photon polarization state given by Eq. 1.35 is calculated to be

$$C(\rho) = \max\{0, (|E_V||E_H|+|J_{VH}|) - (|E_V||E_H|-|J_{VH}|)\} = 2|J_{VH}|. \tag{1.37}$$

Comparing with Eq. 1.31, we observe that

$$P = \sqrt{(|E_V|-|E_H|)^2 + 4|J_{VH}|^2} \geq \sqrt{4|J_{VH}|^2} = 2|J_{VH}| = C(\rho), \tag{1.38}$$

where the equality holds when $|E_V| = |E_H|$, namely, when the horizontal and vertical components of the pump beam have equal magnitudes, the degree of polarization of the pump beam equals the concurrence of the two-photon polarization state. Therefore, we have shown that, at least for the two-qubit states with only two nonzero diagonal elements, the degree of polarization of the pump beam sets an upper bound for the attainable polarization entanglement of the down-converted photons in SPDC. It is important to note that the relation derived in the section does not necessarily translate to the case in which the pump and down-converted photons are considered in different DoFs. The influence of pump coherence in a given DoF on the entanglement of down-converted photons in a different DoF is derived in Chapter 2, where we have specifically considered the influence of spatial coherence of the pump on the polarization entanglement of the down-converted photons.

1.6 The structure of the thesis

This thesis consists of six chapters, including this introduction.

Chapter 2 presents my published work on the first experimental generation of two-photon polarization entanglement from SPDC pumped by a spatiotemporally incoherent light source—a light-emitting diode (LED). This is also among the first experimental studies of the influence of pump coherence on two-photon entanglement generated by SPDC. To theoretically model the experimental results, we showed that the dispersion and birefringence of the nonlinear medium couple different DoFs in SPDC-based entanglement generation. As a result, each spatiotemporal component of the pump can be mapped to a polarization-entangled state with distinct phase factors, leading to reduced overall polarization entanglement when multiple spatiotemporal modes of the SPDC field are detected.

Chapter 3 presents experimental characterization of SPDC-generated two-photon states that display spatially varying polarization entanglement. Specifically, we experimentally resolve the cross-influence between spatial and polarization DoFs by mapping the transverse momenta of the pump beam and the down-converted photons to corresponding two-photon polarization-entangled states, each with a distinct but well-defined relative phase between orthogonal polarization components. The spatial-polarization mapping obtained in this study agrees well with theoretical predictions in existing literature, including those presented in Chapter 2. These results confirm that the influence of the spatial properties of the pump beam on the polarization entanglement is deterministic and dependent on the technical design of the experimental setup. This has two important implications: (i) one can harness this spatial-polarization mapping to engineer structure entanglement in higher dimensions, which enables novel quantum information processing applications; (ii) one can compensate for the spatial distinguishabilities in polarization DoF so that high polarization entanglement can be generated using pump sources with arbitrary spatial properties, including low coherence.

Chapter 4 presents my published work on the first experimental violation of local realism with spatially multimode SPDC pumped by spatially incoherent light. By placing the nonlinear crystal at the center of a Sagnac-type polarization interferometer, we minimize the spatial and temporal walkoff that the pump photons and the down-converted photons might otherwise experience. As a result, we induce highly indistinguishable SPDC processes that generate near-identical polarization-entangled two-photon states across all spatial modes. This leads to the generation of high polarization entanglement that violates local realism in the CHSH formalism, which has not been achieved using a spatially multimode SPDC field pumped by spatially incoherent light. This work supplies strong evidence that the spatial incoherence of the pump does not place a fundamental constraint on the attainable polarization entanglement. Consequently, by optimizing the technical aspects of the experimental setup, one can generate high two-photon entanglement regardless of the pump's coherence. In other words, incoherent light sources are capable of producing entanglement comparable to that of lasers.

Chapter 5 presents the first experimental generation of entangled photon states using SPDC pumped by a natural source of light—sunlight. We have integrated a sunlight concentration module with the entangled photon source used in Chapter 4. The concentrated and filtered sunlight then drives SPDC and produces highly polarization-entangled two-photon states, and the entanglement is certified by a high concurrence and a violation of the CHSH inequality. These results demonstrate that natural sources of light, which are ubiquitous and nearly inexhaustible, can drive the nonlinear optical processes and generate entangled photon states. We believe that with optimized sunlight concentration and nonlinear conversion efficiency, this technology can replace laser-driven entangled photon sources in many photonic quantum devices. Therefore, this work marks a defining step towards environmentally friendly and energy-efficient photonic quantum technologies.

Chapter 6 summarizes our work and suggests follow-up research directions.

Chapter 2

Experimental generation of polarization entanglement from spontaneous parametric down-conversion pumped by spatiotemporally highly incoherent light

I undertook this project when I joined Prof. Robert Boyd's group in late 2019. Prof. Robert Boyd proposed the idea that two-photon polarization entanglement can be generated from SPDC pumped by spatiotemporally incoherent light. With help from Dr. Boris Braverman and Dr. Girish Kulkarni, I built the experimental setup shown in Fig. 1 to study this subject. In the experiments, I observed that SPDC pumped by an LED, which is a spatiotemporally highly *incoherent* light source, produces consistently lower polarization entanglement than that pumped by a laser, which is a spatiotemporally highly *coherent* light source (as shown in Fig. 2 and Fig. 3).

Although it was tempting to superficially attribute the reduced entanglement directly to the spatial incoherence of the pump, I kept looking for an analytical explanation to quantify this effect. After carefully reviewing the theoretical backgrounds, I realized that the birefringence and dispersion of the nonlinear medium can couple the spatial, temporal, and polarization DoFs and lead to spatiotemporal distinguishability in the resulting two-photon polarization states, which manifests as entanglement degradation. Through extensive discussions with all co-authors, I formalized this conceptual understanding into a detailed theoretical model and conducted numerical simulations to show that this model accurately explains the experimental results (as shown in Fig. 2 and supplemental materials). Dr. Kulkarni helped me refine the mathematical derivations. I wrote the first draft of the manuscript, which had undergone multiple rounds of revision by Dr. Kulkarni. All co-authors subsequently contributed to the writing. Prof. Robert Boyd supervised the research. This work has been published in Physical Review A.

Letter

Experimental generation of polarization entanglement from spontaneous parametric down-conversion pumped by spatiotemporally highly incoherent light

Cheng Li,[1,*] Boris Braverman,[1] Girish Kulkarni,[1] and Robert W. Boyd[1,2,†]
[1]*Department of Physics, University of Ottawa, Ottawa, Ontario, Canada K1N 6N5*
[2]*Institute of Optics, University of Rochester, Rochester, New York 14627, USA*

(Received 31 October 2022; accepted 20 March 2023; published 10 April 2023; corrected 20 April 2023)

We investigate the cross influence of the pump coherence on the entanglement produced from spontaneous parametric down-conversion (SPDC) in different degrees of freedom (DOFs). We experimentally demonstrate the generation of polarization entanglement from SPDC pumped by a spatiotemporally highly incoherent (STHI) light-emitting diode. Our quantum state tomography measurements using multimode collection fibers to avoid postselection yield a two-qubit state with the concurrence of 0.531 ± 0.006 and purity of 0.647 ± 0.005, in excellent agreement with our theoretically predicted concurrence of 0.552 and purity of 0.652. We find that using an STHI pump reduces the entanglement and purity of the output polarization two-qubit state due to a coupling between the spatiotemporal and polarization DOFs introduced by the birefringence and dispersion of the nonlinear crystal. The viability of SPDC with STHI pumps is important for two reasons: (i) STHI sources are ubiquitous and available at a wider range of wavelengths than lasers, and (ii) the generated STHI polarization-entangled two-photon states could potentially be useful in long-distance quantum communication schemes due to their robustness to scattering.

DOI: 10.1103/PhysRevA.107.L041701

In the last few decades, entangled photon pairs produced from spontaneous parametric down-conversion (SPDC) [1–3] have become a ubiquitous resource for fundamental experiments in quantum optics [4–10] and practical realizations of quantum communication protocols [11–13]. In the context of SPDC, a number of studies have sought to understand the fundamental origin of the nonlocal correlations of the entangled photons, and how those correlations can be precisely tailored for various quantum applications [14–24]. In particular, the influence of the pump field's coherence properties on the generated two-photon entanglement has been investigated in the spatial [14–19], temporal [20–22], and polarization [23,24] degrees of freedom (DOFs). In each DOF, it was shown that in the absence of postselection, the pump's coherence sets an upper bound on the generated entanglement in the same DOF. For instance, in the polarization DOF, if the setup is a closed system that does not involve postselection, the pump's polarization coherence determines the maximum achievable polarization entanglement of the generated two-qubit signal-idler state [23]. However, such studies implicitly ignore or assume perfect pump coherence in every DOF other than the specific DOF under consideration. As a result, the cross influence of the pump coherence in a given DOF on the entanglement generated in a different DOF is not well understood. For instance, it is not well understood if a lack of spatial or temporal coherence in a perfectly polarized pump field would prevent or somehow influence the two-qubit polarization entanglement between the signal and idler photons. In this context, a theoretical study predicts that polarization entanglement decreases with decreasing pump spatial coherence [25], whereas an experimental study concludes the exact opposite [26]. However, the conclusion of Ref. [26] is dubious because their detection employs single-mode fibers (SMFs) that effectively postselect for a spatially highly coherent pump.

In this Letter, we experimentally investigate the polarization entanglement produced from SPDC pumped by a perfectly polarized spatiotemporally highly incoherent (STHI) beam from a light-emitting diode (LED). In contrast with Ref. [26], we collect the entangled photons using large-aperture multimode fibers (MMFs) to significantly reduce the influence of postselection. The output two-qubit state is measured to have a concurrence of 0.531 ± 0.006 and a purity of 0.647 ± 0.005, in excellent agreement with our theoretically predicted concurrence of 0.552 and purity of 0.652. In essence, we find that the birefringence and dispersion of the crystal medium couple the spatiotemporal and polarization degrees of freedom in the experiment. Consequently, the lack of spatiotemporal coherence in the pump results in a degradation of the entanglement and purity of the output polarization two-qubit signal-idler state when measured in a nonpostselective manner. In what follows, we describe the theory and then present the experimental results of our quantum state tomography and polarization correlation measurements.

We consider SPDC pumped by spatiotemporally partially coherent light in the type-I double-crystal configuration outlined in Ref. [27]. We define $\boldsymbol{q}_j$ and ω_j for $j = p, s, i$ as the transverse wave vectors and frequencies corresponding to the pump, signal, and idler, respectively. From conservation of transverse momentum and energy, it follows that $\boldsymbol{q}_p = \boldsymbol{q}_s + \boldsymbol{q}_i$

---

[*] cli221@uottawa.ca
[†] rboyd@uottawa.ca

and $\omega_p = \omega_s + \omega_i$. The state vector describing the far-field spatiotemporal and polarization correlations of a given element in the generated two-photon ensemble can be written as (see Supplemental Material [28])

$$\begin{aligned}|\psi\rangle = A \iiiint & d\boldsymbol{q}_s d\boldsymbol{q}_i d\omega_s d\omega_i\, \Phi(\Delta k_z L)\\ & \times [E_V(\boldsymbol{q}_p, \omega_p)|H, \boldsymbol{q}_s, \omega_s\rangle |H, \boldsymbol{q}_i, \omega_i\rangle\\ & + E_H(\boldsymbol{q}_p, \omega_p) e^{i\chi(\boldsymbol{q}_s, \omega_s, \boldsymbol{q}_i, \omega_i)} |V, \boldsymbol{q}_s, \omega_s\rangle |V, \boldsymbol{q}_i, \omega_i\rangle], \quad (1)\end{aligned}$$

where A is a normalization factor, Δk_z is the longitudinal wave-vector mismatch, L is the length of each individual crystal, $\Phi(\Delta k_z L) = \mathrm{sinc}[\Delta k_z L/2] e^{i\Delta k_z L/2}$ is the phase-matching function, $E_{H(V)}(\boldsymbol{q}_p, \omega_p)$ denotes the horizontal (vertical) polarization component of the pump spectral amplitude inside the crystal, and $|H(V), \boldsymbol{q}_j, \omega_j\rangle$ for $j = s, i$ denotes the basis vector for the horizontal (vertical) polarization of the corresponding spatiotemporal mode of the signal and idler photon, respectively. The quantity $\chi(\boldsymbol{q}_s, \omega_s, \boldsymbol{q}_i, \omega_i)$ represents a relative phase acquired due to spatial and temporal walk-off between the two-photon state amplitudes generated in the two crystals. However, we assume that by using temporal and spatial walk-off compensation elements in the setup, one can ensure $\chi(\boldsymbol{q}_s, \omega_s, \boldsymbol{q}_i, \omega_i) \approx 0$ (see Supplemental Material [28]). For a pump field with spectral amplitude $E_0(\boldsymbol{q}_p, \omega_p)$ that is linearly polarized at 45° or −45° before entering the crystal, we have $|E_H(\boldsymbol{q}_p, \omega_p)| = |E_V(\boldsymbol{q}_p, \omega_p)| = |E_0(\boldsymbol{q}_p, \omega_p)|/\sqrt{2}$ and the relative phase between $E_H(\boldsymbol{q}_p, \omega_p)$ and $E_V(\boldsymbol{q}_p, \omega_p)$ is 0 or π, respectively. However, inside the crystal, the birefringence and dispersion properties of the medium induce a relative phase $\phi(\boldsymbol{q}_p, \omega_p)$ between $E_H(\boldsymbol{q}_p, \omega_p)$ and $E_V(\boldsymbol{q}_p, \omega_p)$. Using these relations, the final measured polarization two-qubit state ρ can be written in the computational basis $\{|HH\rangle, |HV\rangle, |VH\rangle, |VV\rangle\}$ as

$$\rho = \mathrm{Tr}_{\mathrm{spat,temp}}(\langle|\psi\rangle\langle\psi|\rangle) = \begin{bmatrix} 1/2 & 0 & 0 & \mu/2 \\ 0 & 0 & 0 & 0 \\ 0 & 0 & 0 & 0 \\ \mu^*/2 & 0 & 0 & 1/2 \end{bmatrix}, \quad (2)$$

where $\mathrm{Tr}_{\mathrm{spat,temp}}$ denotes a partial trace over the spatial and temporal degrees of freedom, $\langle\cdot\rangle$ denotes an ensemble average over many realizations of the pump field, and $|A|^2$ is chosen such that $\mathrm{Tr}(\rho) = 1$. The quantity μ is then written as (see Supplemental Material [28])

$$\mu = |A|^2 \int_{\Delta\boldsymbol{q}_p} d\boldsymbol{q}_p \int_{\Delta\omega_p} d\omega_p\, |E_0(\boldsymbol{q}_p, \omega_p)|^2\, e^{i\phi(\boldsymbol{q}_p, \omega_p)}, \quad (3)$$

where $\Delta\boldsymbol{q}_p = \Delta\boldsymbol{q}_s + \Delta\boldsymbol{q}_i$, and $\Delta\omega_p = \Delta\omega_s + \Delta\omega_i$; $\Delta\boldsymbol{q}_{s(i)}$ denotes the angular bandwidth corresponding to the detection aperture in the signal (idler) arm, and $\Delta\omega_{s(i)}$ denotes the bandwidth of the spectral filter in the signal (idler) arm. It may be verified that $|\mu|$ satisfies $0 \leqslant |\mu| \leqslant 1$, with $|\mu| \to 0$ when $\phi(\boldsymbol{q}_p, \omega_p)$ varies rapidly, and $|\mu| \to 1$ when $\phi(\boldsymbol{q}_p, \omega_p)$ is constant, in the integration region. Moreover, $|\mu|$ determines the purity $\mathrm{Tr}(\rho^2) = \{1 + |\mu|^2\}/2$ and the concurrence $C(\rho) = |\mu|$ of the measured two-qubit state. In this work, we use concurrence to quantify the entanglement because, in contrast with the Bell-Clauser-Horne-Shimony-Holt parameter, which is only a sufficient but not necessary entanglement witness [29], the concurrence can be used to quantify the degree of entanglement of an arbitrary two-qubit state [30].

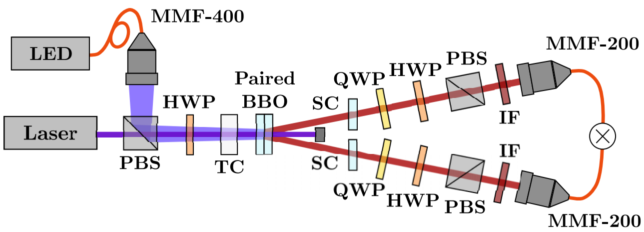

FIG. 1. Schematic diagram of the experimental setup. LED: light-emitting diode; PBS: polarizing beam splitter; HWP: half-wave plate; TC: temporal compensator; BBO: β-barium borate; SC: spatial compensator; QWP: quarter-wave plate; IF: interference filter; MMF-400 (200): multimode fiber with a core diameter of 400 (200) µm.

We now consider the effect of the pump's spatiotemporal coherence on the measured two-qubit state. For a spatiotemporally highly coherent pump such as a laser, the function $E_0(\boldsymbol{q}_p, \omega_p)$ is highly narrow. Consequently, the averaging of $e^{i\phi(\boldsymbol{q}_p, \omega_p)}$ in Eq. (3) effectively occurs over a very small integration region, which leads to $|\mu|$ being close to unity, irrespective of $\Delta\boldsymbol{q}_{s(i)}$ and $\Delta\omega_{s(i)}$. This predicts high measured values of concurrence and purity of two-qubit states produced from a laser pump, regardless of the detection system. However, for an STHI pump such as an LED, the function $E_0(\boldsymbol{q}_p, \omega_p)$ has support over a broad range of q_p and ω_p, and, consequently, the role of $\Delta\boldsymbol{q}_{s(i)}$ and $\Delta\omega_{s(i)}$ in the integrations in Eq. (3) becomes significant. For a detection system that employs SMFs and narrow-band spectral filters, $\Delta\boldsymbol{q}_{s(i)}$ and $\Delta\omega_{s(i)}$ are small. As a result, the averaging of $e^{i\phi(\boldsymbol{q}_p, \omega_p)}$ in Eq. (3) again effectively occurs over a small integration region constrained by the relations $\boldsymbol{q}_p = \boldsymbol{q}_s + \boldsymbol{q}_i$ and $\omega_p = \omega_s + \omega_i$. This leads to a high value of $|\mu|$, implying high values of purity and concurrence. In other words, the detection postselection obscures the effect of the pump's lack of coherence. However, for a detection system that employs MMFs and broad-band spectral filters, $\Delta\boldsymbol{q}_{s(i)}$ and $\Delta\omega_{s(i)}$ are large. Consequently, the averaging of $e^{i\phi(\boldsymbol{q}_p, \omega_p)}$ in Eq. (3) occurs over a much larger range, and the effect of postselection is significantly reduced. In this case, Eq. (3) would yield a reduced value of $|\mu|$, implying a degradation in the purity and concurrence of the measured state. Thus, our theory predicts that an STHI pump results in a degradation of the entanglement and purity of the output polarization two-qubit state, but to observe this degradation, it is necessary to use MMFs to collect the entangled photons.

In Fig. 1, we depict our experimental setup. The optical field from a Thorlabs M405L3 LED of center wavelength 405 nm, and full width at half maximum (FWHM) bandwidth of 20 nm, is butt-coupled into an MMF with core diameter 400 µm and numerical aperture 0.39, and coupled out into free space using a microscope objective. The LED light at the output of the fiber is measured to be 6 mW. The resulting collimated LED beam is then made linearly polarized at 45° by passing it through a polarizing beam splitter (PBS) and a half-wave plate (HWP), and then made incident onto a paired

β-barium borate (BBO) double crystal cut for noncollinear emission with a half-opening angle of 3° for perpendicular pump incidence. The double crystal consists of two identically cut 0.5-mm-thick type-I BBO crystals attached to each other with their optic axes oriented perpendicularly to one another. An ultraviolet continuous-wave laser with center wavelength 405 nm, bandwidth 2 nm, and power 20 mW is made linearly polarized at -45° and aligned as a pump for benchmarking purposes such that experiments performed with the LED pump can be compared with those performed with the laser pump for the same setup. In both cases, the pump photons are propagated through a 5-mm temporal compensation (TC) quartz crystal to precompensate for the temporal walk-off that the two orthogonal polarizations subsequently experience inside the double crystal [31,32]. The conjugate signal and idler photons from two diametrically opposite regions of the noncollinear emission ring are each sent through a 0.25-mm-thick BBO spatial compensation (SC) crystal to compensate for spatial walk-off effects that the photons have experienced inside the double crystal [33]. The photons are then passed through combinations of a quarter-wave plate (QWP), HWP, and PBS to measure their joint two-photon state. Note that we choose all the waveplates in the setup to be zero order and the optics axes of all the waveplates are carefully aligned before taking measurements. This ensures that our results are not influenced by spectral dispersion or manufacturing imperfections of the waveplates. The diameters of waveplates are chosen to be much larger than the beam size to avoid postselection. The photons are sent through bandpass filters with center wavelength 810 nm and FWHM bandwidth of 10 nm. Subsequently, the photons are coupled into MMFs with core diameter 200 μm and numerical aperture 0.39 placed in the far field. Finally, the photons from the MMFs are detected using PerkinElmer SPCM-QRH-14-FC avalanche photodiodes and their coincidence count rates are extracted using the Universal Quantum Devices (UQD) Logic-16 data-acquisition unit with a coincidence time resolution window of one nanosecond.

We record coincidence rates for different rotation angles of the QWP and HWP in each arm, both for performing quantum state tomography (QST) of the two-photon polarization state and for measuring polarization correlation fringes in mutually unbiased bases. For the former purpose of QST, we record the coincidence rates with 16 different projective measurements, subtract the theoretical accidental count rates, and use the maximum likelihood state estimation (MLSE) algorithm outlined in Ref. [34] to infer the two-qubit density matrix ρ. We then calculate the concurrence $C(\rho)$ [30] and purity $\mathrm{Tr}[\rho^2]$. For the latter purpose of recording polarization correlation fringes, we fix the polarization in the signal arm and record the coincidence rate as a function of the linear polarization in the idler arm, which is defined by an angle θ with respect to the H polarization. For laser-pumped SPDC, we set an acquisition time of 10 s for each basis and the maximum coincidence rate is $\sim$700 s^{-1}. In contrast, for LED-pumped SPDC, we set an acquisition time of 60 min per basis, and the maximum coincidence rate was $\sim$0.04 s^{-1}. Thus, the coincidence rate for LED-pumped SPDC is much smaller than that of laser-pumped SPDC, which could perhaps be explained by the following two reasons: (i) the LED has a lower power than the laser and (ii) the down-conversion efficiency for the LED pump could be lower than that for the laser pump due to the lack of coherent phase matching [35].

In Fig. 2(a), we depict the theoretically computed relative phase $\phi(\boldsymbol{q}_p, \omega_p)$. Since the relative phase has only negligible dependence on the wavelength of the pump (see Supplemental Material [28]), we mainly focus on the dependence on the pump transverse wave vector and depict only the relative phase $\phi(\boldsymbol{q}_p, \omega_{p0} = 2\pi c/\lambda_{p0})$ for the central pump wavelength $\lambda_{p0} = 405$ nm. Figures 2(b) and 2(c) depict the theoretically predicted and experimentally measured two-photon density matrices for laser- and LED-pumped SPDC, respectively. For laser-pumped SPDC, the experimentally measured two-qubit state has a concurrence of 0.955 ± 0.003 and purity of 0.957 ± 0.003, in close agreement with the theoretically predicted concurrence 0.999 and purity 0.999. We verify that these results are highly stable over multiple measurements performed at different times. For LED-pumped SPDC, the experimentally measured two-qubit state has a concurrence of 0.531 ± 0.006 and purity of 0.647 ± 0.005, in close agreement with the theoretically predicted concurrence of 0.552 and purity of 0.652. The fidelity of the experimentally measured density matrices to the theoretically predicted ones for laser-pumped and LED-pumped SPDC is 96.07% and 94.92%, respectively.

In Fig. 3, we depict the polarization correlation fringes in horizontal-vertical (H-V) and antidiagonal-diagonal (A-D) bases. Figures 3(a) and 3(b) depict the case of laser-pumped SPDC, whereas Figs. 3(c) and 3(d) depict the case of LED-pumped SPDC. The scatter plots and solid lines represent the experimentally measured data points and the theoretically predicted correlation fringes, respectively. We notice that for laser-pumped SPDC, the fringes in Figs. 3(a) and 3(b) exhibit high contrast in the H-V and A-D bases simultaneously. For quantitative characterization, we calculate the experimental fringe visibility values from sinusoidal fit curves of the measured counts. The fringe visibility in the H-V basis is $98.8 \pm 1.2\%$ and the visibility in the A-D basis is $93.7 \pm 1.8\%$. This presence of strong correlations in two mutually unbiased bases is the characteristic feature of entanglement. In contrast, for LED-pumped SPDC, the fringes in Fig. 3(c) corresponding to the H-V basis exhibit high contrast, but the fringes in Fig. 3(d) exhibit diminished contrast. In particular, the fringe visibility in the H-V basis is $95.9 \pm 6.7\%$, but the fringe visibility in the A-D basis is $39.4 \pm 3.9\%$. In other words, the polarization correlations in the H-V basis remain high, but those in the A-D basis are degraded, which is consistent with the entanglement reduction observed in our QST measurements.

In summary, we experimentally demonstrated the generation of polarization entanglement from SPDC pumped by an STHI LED source. We first presented a theoretical analysis that shows how the birefringence and dispersion of the crystal medium couple the spatiotemporal and polarization degrees of freedom in the experiment. This analysis predicts a degradation in the purity and entanglement of the two-qubit state produced from an STHI LED pump compared to that produced from a coherent laser pump. We then performed the experiment, both with an STHI LED pump and with a laser pump on the same setup for benchmarking purposes. In both cases, we showed that our experimental measurements of the two-qubit state using MMFs to reduce

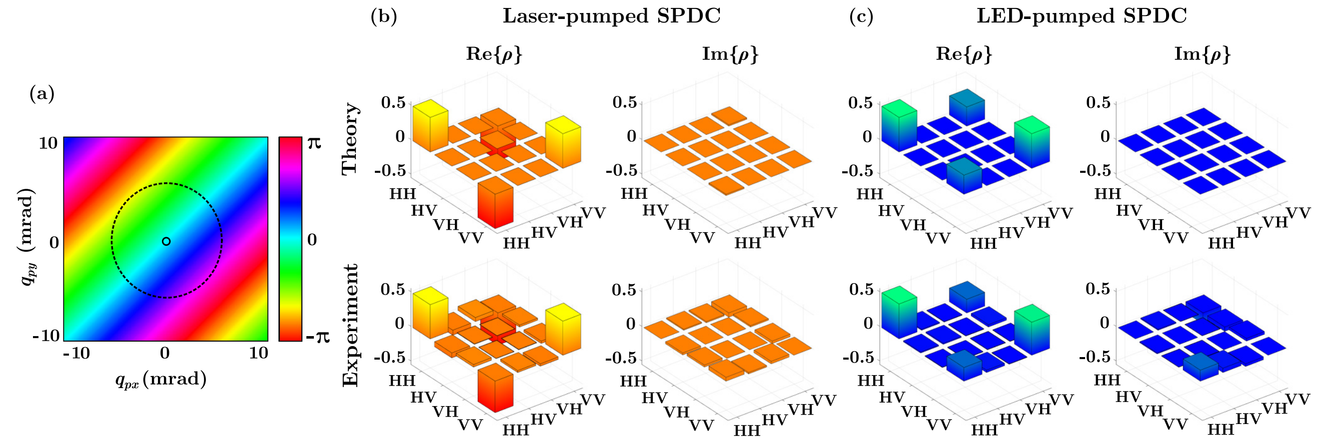

FIG. 2. (a) Theoretical two-dimensional (2D) color plot of $\phi(\boldsymbol{q}_p, \omega_{p0} = 2\pi c/\lambda_{p0})$ for β-barium borate (BBO), where $\lambda_{p0} = 405$ nm. The solid and dashed circles indicate the effective angular bandwidths of laser and LED pumps, respectively. (b),(c) The theoretically predicted and experimentally measured density matrices for laser-pumped and LED-pumped SPDC, respectively. Note that the laser pump and the LED pump at the PBS output are linearly polarized at -45° and 45°, respectively, because they are coupled into the crystal from different ports of the PBS as shown in Fig. 1.

the influence of postselection are in excellent agreement with our theoretical predictions. For laser-pumped SPDC, the output two-qubit state has a concurrence of 0.955 ± 0.003 and purity of 0.957 ± 0.003, whereas for LED-pumped SPDC, the two-qubit state has a concurrence of 0.531 ± 0.006 and a purity of 0.647 ± 0.005. Thus, the entanglement and purity of the polarization-entangled signal-idler state are lower for LED-pumped SPDC compared to laser-pumped SPDC. We also argue that setup instabilities cannot be the primary cause of this reduction because other studies employing highly efficient, periodically poled crystals demonstrate that detection using SMFs yields high purity and entanglement despite the long acquisition times [36]. We were unable to perform such measurements using SMFs ourselves because of the poor efficiency of our bulk-crystal-based SPDC setup.

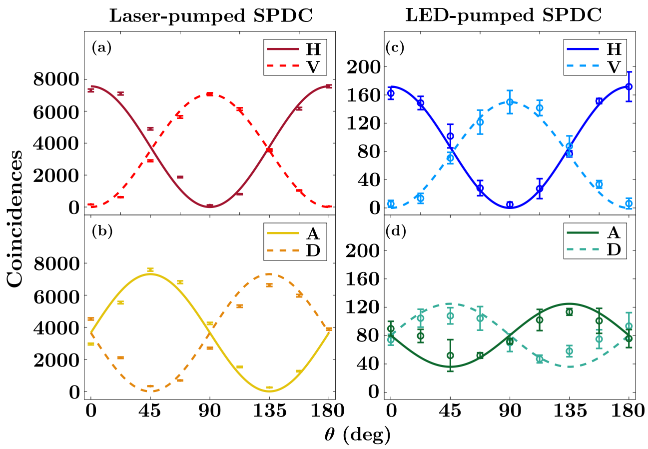

FIG. 3. Polarization correlation fringes in horizontal-vertical (H-V) basis and antidiagonal-diagonal (A-D) basis measured by fixing the signal photon's polarization and varying the idler photon's polarization represented by an angle θ with respect to the horizontal polarization. (a) and (b) correspond to laser-pumped SPDC, whereas (c) and (d) correspond to LED-pumped SPDC. The scatter plots represent the experimentally measured coincidence counts. The solid lines represent the theoretically predicted correlation fringes.

In the future, our work might inspire further studies on SPDC with STHI sources. For instance, it may be possible to compensate for $\phi(\boldsymbol{q}_p, \omega_p)$ and enhance the polarization entanglement produced from a spatiotemporally incoherent pump. Moreover, the analysis in our study is restricted to type-I double-crystal SPDC, which employs critical phase matching. However, there are also noncritical phase-matching methods that do not rely on birefringence, and therefore do not couple the spatial and polarization degrees of freedom [3,37–40]. Using such methods, it may be possible to generate polarization two-qubit states with higher purity and entanglement with an STHI pump. Regardless, our study demonstrates the viability of using SPDC pumped by STHI sources for producing STHI polarization-entangled two-qubit states, which could have two important implications. First, STHI sources such as LEDs and sunlight are ubiquitous and available at a wider range of wavelengths than their coherent counterparts such as lasers. Second, the STHI polarization-entangled two-qubit states produced from SPDC pumped by STHI sources might be well suited for long-distance quantum communication schemes due to their robustness to scattering and turbulence [41–43].

Note added. Recently, we became aware of a similar study being simultaneously carried out by Zhang and coworkers [36]. We believe that our studies complement each other.

We acknowledge useful discussions with W. Zhang, E. Giese, J. Upham, J. Rioux, and S. Lemieux. We also acknowledge funding from the Canada First Research Excellence Fund (Transformative Quantum Technologies). B.B. acknowledges support from the Banting Postdoctoral Fellowship. R.W.B. acknowledges support through the Natural Sciences and Engineering Research Council (NSERC) of Canada, the Canada Research Chairs program, by U.S. DARPA Award No. W911NF-18-1-0369, U.S. ARO Award No. W911NF-

18-1-0337, U.S. Office of Naval Research MURI Award No. N00014-20-1-2558, U.S. National Science Foundation Award No. 2138174, and the U.S. Department of Energy Award No. FWP 76295.

---

[1] D. C. Burnham and D. L. Weinberg, Observation of Simultaneity in Parametric Production of Optical Photon Pairs, Phys. Rev. Lett. **25**, 84 (1970).
[2] C. K. Hong and L. Mandel, Theory of parametric frequency down conversion of light, Phys. Rev. A **31**, 2409 (1985).
[3] R. W. Boyd, *Nonlinear Optics* (Academic Press, San Diego, CA, 2020).
[4] C. K. Hong, Z. Y. Ou, and L. Mandel, Measurement of Subpicosecond Time Intervals between Two Photons by Interference, Phys. Rev. Lett. **59**, 2044 (1987).
[5] Z. Y. Ou and L. Mandel, Violation of Bell's Inequality and Classical Probability in a Two-Photon Correlation Experiment, Phys. Rev. Lett. **61**, 50 (1988).
[6] G. Weihs, T. Jennewein, C. Simon, H. Weinfurter, and A. Zeilinger, Violation of Bell's Inequality under Strict Einstein Locality Conditions, Phys. Rev. Lett. **81**, 5039 (1998).
[7] Y. H. Shih and C. O. Alley, New Type of Einstein-Podolsky-Rosen-Bohm Experiment Using Pairs of Light Quanta Produced by Optical Parametric Down Conversion, Phys. Rev. Lett. **61**, 2921 (1988).
[8] T. E. Kiess, Y. H. Shih, A. V. Sergienko, and C. O. Alley, Einstein-Podolsky-Rosen-Bohm Experiment Using Pairs of Light Quanta Produced by Type-II Parametric Down-Conversion, Phys. Rev. Lett. **71**, 3893 (1993).
[9] L. J. Wang, X. Y. Zou, and L. Mandel, Induced coherence without induced emission, Phys. Rev. A **44**, 4614 (1991).
[10] X. Y. Zou, L. J. Wang, and L. Mandel, Induced Coherence and Indistinguishability in Optical Interference, Phys. Rev. Lett. **67**, 318 (1991).
[11] R. Ursin, F. Tiefenbacher, T. Schmitt-Manderbach, H. Weier, T. Scheidl, M. Lindenthal, B. Blauensteiner, T. Jennewein, J. Perdigues, P. Trojek, B. Ömer, M. Fürst, M. Meyenburg, J. Rarity, Z. Sodnik, C. Barbieri, H. Weinfurter, and A. Zeilinger, Entanglement-based quantum communication over 144 km, Nat. Phys. **3**, 481 (2007).
[12] J. Yin, Y.-H. Li, S.-K. Liao, M. Yang, Y. Cao, L. Zhang, J.-G. Ren, W.-Q. Cai, W.-Y. Liu, S.-L. Li, R. Shu, Y.-M. Huang, L. Deng, L. Li, Q. Zhang, N.-L. Liu, Y.-A. Chen, C.-Y. Lu, X.-B. Wang, F. Xu *et al.*, Entanglement-based secure quantum cryptography over 1120 kilometres, Nature (London) **582**, 501 (2020).
[13] D. Bouwmeester, J.-W. Pan, K. Mattle, M. Eibl, H. Weinfurter, and A. Zeilinger, Experimental quantum teleportation, Nature (London) **390**, 575 (1997).
[14] A. K. Jha and R. W. Boyd, Spatial two-photon coherence of the entangled field produced by down-conversion using a partially spatially coherent pump beam, Phys. Rev. A **81**, 013828 (2010).
[15] E. Giese, R. Fickler, W. Zhang, L. Chen, and R. W. Boyd, Influence of pump coherence on the quantum properties of spontaneous parametric down-conversion, Phys. Scr. **93**, 084001 (2018).
[16] C. H. Monken, P. H. Souto Ribeiro, and S. Pádua, Transfer of angular spectrum and image formation in spontaneous parametric down-conversion, Phys. Rev. A **57**, 3123 (1998).
[17] H. Defienne and S. Gigan, Spatially entangled photon-pair generation using a partial spatially coherent pump beam, Phys. Rev. A **99**, 053831 (2019).
[18] W. Zhang, R. Fickler, E. Giese, L. Chen, and R. W. Boyd, Influence of pump coherence on the generation of position-momentum entanglement in optical parametric down-conversion, Opt. Express **27**, 20745 (2019).
[19] L. Hutter, G. Lima, and S. P. Walborn, Boosting Entanglement Generation in Down-Conversion with Incoherent Illumination, Phys. Rev. Lett. **125**, 193602 (2020).
[20] A. V. Burlakov, M. V. Chekhova, O. A. Karabutova, and S. P. Kulik, Biphoton interference with a multimode pump, Phys. Rev. A **63**, 053801 (2001).
[21] A. K. Jha, M. N. O'Sullivan, Kam Wai Clifford Chan, and R. W. Boyd, Temporal coherence and indistinguishability in two-photon interference effects, Phys. Rev. A **77**, 021801(R) (2008).
[22] G. Kulkarni, P. Kumar, and A. K. Jha, Transfer of temporal coherence in parametric down-conversion, J. Opt. Soc. Am. B **34**, 1637 (2017).
[23] G. Kulkarni, V. Subrahmanyam, and A. K. Jha, Intrinsic upper bound on two-qubit polarization entanglement predetermined by pump polarization correlations in parametric down-conversion, Phys. Rev. A **93**, 063842 (2016).
[24] N. Meher, A. S. M. Patoary, G. Kulkarni, and A. K. Jha, Intrinsic degree of coherence of two-qubit states and measures of two-particle quantum correlations, J. Opt. Soc. Am. B **37**, 1224 (2020).
[25] P. Sharma, N. K. Pathak, and B. Kanseri, Controlling polarization entanglement in biphotons generated with partially spatially coherent pump beam, Results Phys. **27**, 104506 (2021).
[26] Y. Ismail, S. Joshi, and F. Petruccione, Polarization-entangled photon generation using partial spatially coherent pump beam, Sci. Rep. **7**, 12091 (2017).
[27] P. G. Kwiat, E. Waks, A. G. White, I. Appelbaum, and P. H. Eberhard, Ultrabright source of polarization-entangled photons, Phys. Rev. A **60**, R773 (1999).
[28] See Supplemental Material at http://link.aps.org/supplemental/10.1103/PhysRevA.107.L041701 for a detailed derivation of the two-photon density matrix, a detailed derivation of the relative phase, estimation method of the effective angular bandwidth of the pump, and a comparison between theoretical and experimental results for LED-pumped SPDC, including Refs. [22,27,32,33,44–47].
[29] R. F. Werner, Quantum states with Einstein-Podolsky-Rosen correlations admitting a hidden-variable model, Phys. Rev. A **40**, 4277 (1989).
[30] W. K. Wootters, Entanglement of Formation of an Arbitrary State of Two Qubits, Phys. Rev. Lett. **80**, 2245 (1998).
[31] Y. Nambu, K. Usami, Y. Tsuda, K. Matsumoto, and K. Nakamura, Generation of polarization-entangled photon pairs in a cascade of two type-I crystals pumped by femtosecond pulses, Phys. Rev. A **66**, 033816 (2002).

[32] R. Rangarajan, M. Goggin, and P. Kwiat, Optimizing type-I polarization-entangled photons, Opt. Express **17**, 18920 (2009).

[33] J. B. Altepeter, E. R. Jeffrey, and P. G. Kwiat, Phase-compensated ultra-bright source of entangled photons, Opt. Express **13**, 8951 (2005).

[34] D. F. V. James, P. G. Kwiat, W. J. Munro, and A. G. White, Measurement of qubits, Phys. Rev. A **64**, 052312 (2001).

[35] X. Zhao, L. Ji, D. Liu, Y. Gao, D. Rao, Y. Cui, W. Feng, F. Li, H. Shi, C. Shan, W. Ma, and Z. Sui, Second-harmonic generation of temporally low-coherence light, APL Photon. **5**, 091301 (2020).

[36] W. Zhang, D. Xu, and L. Chen, Polarization entanglement from parametric down-conversion with a LED pump, arXiv:2211.00841.

[37] H. Wang, T. Horikiri, and T. Kobayashi, Polarization-entangled mode-locked photons from cavity-enhanced spontaneous parametric down-conversion, Phys. Rev. A **70**, 043804 (2004).

[38] F. Steinlechner, P. Trojek, M. Jofre, H. Weier, D. Perez, T. Jennewein, R. Ursin, J. Rarity, M. W. Mitchell, J. P. Torres, H. Weinfurter, and V. Pruneri, A high-brightness source of polarization-entangled photons optimized for applications in free space, Opt. Express **20**, 9640 (2012).

[39] F. Steinlechner, S. Ramelow, M. Jofre, M. Gilaberte, T. Jennewein, J. P. Torres, M. W. Mitchell, and V. Pruneri, Phase-stable source of polarization-entangled photons in a linear double-pass configuration, Opt. Express **21**, 11943 (2013).

[40] F. Steinlechner, M. Gilaberte, M. Jofre, T. Scheidl, J. P. Torres, V. Pruneri, and R. Ursin, Efficient heralding of polarization-entangled photons from type-0 and type-II spontaneous parametric downconversion in periodically poled KTiOPO$_4$, J. Opt. Soc. Am. B **31**, 2068 (2014).

[41] A. Bhattacharjee and A. K. Jha, Experimental demonstration of structural robustness of spatially partially coherent fields in turbulence, Opt. Lett. **45**, 4068 (2020).

[42] Y. Qiu and W. She, The influence of atmospheric turbulence on partially coherent two-photon entangled field, Appl. Phys. B **108**, 683 (2012).

[43] S. P. Phehlukwayo, M. L. Umuhire, Y. Ismail, S. Joshi, and F. Petruccione, Influence of coincidence detection of a biphoton state through free-space atmospheric turbulence using a partially spatially coherent pump, Phys. Rev. A **102**, 033732 (2020).

[44] C. K. Law and J. H. Eberly, Analysis and Interpretation of High Transverse Entanglement in Optical Parametric Down Conversion, Phys. Rev. Lett. **92**, 127903 (2004).

[45] M. P. van Exter, A. Aiello, S. S. R. Oemrawsingh, G. Nienhuis, and J. P. Woerdman, Effect of spatial filtering on the Schmidt decomposition of entangled photons, Phys. Rev. A **74**, 012309 (2006).

[46] S. Castelletto, I. P. Degiovanni, A. Migdall, and M. Ware, On the measurement of two-photon single-mode coupling efficiency in parametric down-conversion photon sources, New J. Phys. **6**, 87 (2004).

[47] B. E. Saleh and M. C. Teich, *Fundamentals of Photonics* (Wiley, New York, 2019).

Correction: The previously published Figure 1 contained three incorrect labels and has been replaced.

Supplementary material for: Experimental generation of polarization entanglement from spontaneous parametric down-conversion pumped by spatiotemporally highly incoherent light

Cheng Li,[1,*] Boris Braverman,[1] Girish Kulkarni,[1] and Robert W. Boyd[1,2,†]

[1]*Department of Physics, University of Ottawa, Ottawa, ON, Canada, K1N 6N5*

[2]*Institute of Optics, University of Rochester, Rochester, New York, USA, 14627*

I. DERIVATION OF THE TWO-PHOTON DENSITY MATRIX IN THE POLARIZATION BASIS

Consider a type-I double-crystal setup of the kind outlined in Ref. [S1]. We define $\boldsymbol{q}_j$ and ω_j for $j = p, s, i$ as the transverse wave-vectors and frequencies corresponding to the pump, signal, and idler, respectively. Due to energy and momentum conservation, we have $\boldsymbol{q}_p = \boldsymbol{q}_s + \boldsymbol{q}_i$ and $\omega_p = \omega_s + \omega_i$. In our analysis, the pump could be a general spatiotemporally partially coherent field, and consequently, the two-photon state generated from its SPDC will, in general, be a mixed state. Nevertheless, the final two-photon mixed state can be written as $\rho_{\text{spa,temp,pol}} = \langle |\psi\rangle\langle\psi| \rangle$, where $\langle \cdots \rangle$ denotes an ensemble average over many realizations of the pump field, and each two-photon pure state element in the ensemble is written as

$$|\psi\rangle = A \iiiint \mathrm{d}\boldsymbol{q}_s \mathrm{d}\boldsymbol{q}_i \mathrm{d}\omega_s \mathrm{d}\omega_i \, \Phi(\Delta k_z L) \\ \times \Big[E_V(\boldsymbol{q}_p, \omega_p) |H, \boldsymbol{q}_s, \omega_s\rangle |H, \boldsymbol{q}_i, \omega_i\rangle + E_H(\boldsymbol{q}_p, \omega_p) |V, \boldsymbol{q}_s, \omega_s\rangle |V, \boldsymbol{q}_i, \omega_i\rangle \Big], \quad \text{(S1.1)}$$

where A is a normalization factor, Δk_z is the longitudinal wavevector mismatch, L is the length of each individual crystal, $\Phi(\Delta k_z L) = \mathrm{sinc}[\Delta k_z L/2] e^{i \Delta k_z L / 4 k_p}$ is the phase-matching function, $E_{H(V)}(\boldsymbol{q}_p, \omega_p)$ denotes the horizontal (vertical) polarization component of the pump spectral amplitude inside the crystal, $|H(V), \boldsymbol{q}_j, \omega_j\rangle$ for $j = s, i$ denotes the basis vector for the horizontal (vertical) polarization of the corresponding spatiotemporal mode of the signal and idler photon, respectively. Since the pump polarization are always set at 45° or −45°, we can take $|E_H(\boldsymbol{q}_p, \omega_p)| = |E_V(\boldsymbol{q}_p, \omega_p)|$. Note that compared to Eq. (1) in the main text, here we have dropped the term $e^{i\chi(\boldsymbol{q}_s, \omega_s, \boldsymbol{q}_i, \omega_i)}$, where the quantity $\chi(\boldsymbol{q}_s, \omega_s, \boldsymbol{q}_i, \omega_i)$ represents a relative phase acquired due to spatial and temporal walk-off between the two-photon state amplitudes generated in the two crystals. This approximation of $\chi(\boldsymbol{q}_s, \omega_s, \boldsymbol{q}_i, \omega_i) \approx 0$ is valid only if the spatial and temporal compensation schemes employed are adequate.

In order to verify the assumed adequateness of our compensation schemes, we note the following: In our experiment, the laser has a longitudinal coherence length (~ 150 μm), which is shorter than the length of the crystal (~ 500 μm for each one of the double-crystal). Moreover, we employ multi-mode fibers (MMFs) instead of single-mode fibers

---

[*] cli221@uottawa.ca

[†] rboyd@uottawa.ca

(SMFs) to collect the down-converted photons in order to reduce spatial post-selection. Without adequate compensation, these experimental conditions cause temporal and spatial decoherence, which lead to degradation of entanglement and purity of the generated two-qubit state [S2, S3]. However, the fact that we measure two-qubit states with very high concurrence and purity for laser-pumped SPDC implies that our compensation schemes are adequate.

The two-photon density matrix in the joint basis of spatial, temporal and polarization degree of freedom is written as

$$\begin{aligned}\rho_{\text{spa,temp,pol}} = |A|^2 \iiiint \mathrm{d}\boldsymbol{q}_s \mathrm{d}\boldsymbol{q}_i \mathrm{d}\boldsymbol{q}'_s \mathrm{d}\boldsymbol{q}'_i \iiiint \mathrm{d}\omega_s \mathrm{d}\omega_i \mathrm{d}\omega'_s \mathrm{d}\omega'_i \; |\Phi(\Delta k_z L)|^2 \\ \times \Big[\langle E_V(\boldsymbol{q}_p,\omega_p) E^*_V(\boldsymbol{q}'_p,\omega'_p)\rangle |H,\boldsymbol{q}_s,\omega_s\rangle |H,\boldsymbol{q}_i,\omega_i\rangle \langle H,\boldsymbol{q}'_s,\omega'_s| \langle H,\boldsymbol{q}'_i,\omega'_i| \\ + \langle E_V(\boldsymbol{q}_p,\omega_p) E^*_H(\boldsymbol{q}'_p,\omega'_p)\rangle |H,\boldsymbol{q}_s,\omega_s\rangle |H,\boldsymbol{q}_i,\omega_i\rangle \langle V,\boldsymbol{q}'_s,\omega'_s| \langle V,\boldsymbol{q}'_i,\omega'_i| \\ + \langle E_H(\boldsymbol{q}_p,\omega_p) E^*_V(\boldsymbol{q}'_p,\omega'_p)\rangle |V,\boldsymbol{q}_s,\omega_s\rangle |V,\boldsymbol{q}_i,\omega_i\rangle \langle H,\boldsymbol{q}'_s,\omega'_s| \langle H,\boldsymbol{q}'_i,\omega'_i| \\ + \langle E_H(\boldsymbol{q}_p,\omega_p) E^*_H(\boldsymbol{q}'_p,\omega'_p)\rangle |V,\boldsymbol{q}_s,\omega_s\rangle |V,\boldsymbol{q}_i,\omega_i\rangle \langle V,\boldsymbol{q}'_s,\omega'_s| \langle V,\boldsymbol{q}'_i,\omega'_i|\Big], \quad \text{(S1.2)}\end{aligned}$$

where $\langle \cdots \rangle$ denotes an ensemble average over many realizations of the pump field. The two-photon density matrix ρ in the polarization degree of freedom can be obtained by taking the partial trace of $\rho_{\text{spa,temp,pol}}$ over the spatial and temporal degrees of freedom, i.e,

$$\begin{aligned}\rho = \rho_{\text{pol}} = \mathrm{Tr}_{\text{spa,temp}}(\rho_{\text{spa,temp,pol}}) = |A|^2 \iiiint \mathrm{d}\boldsymbol{q}_s \mathrm{d}\boldsymbol{q}_i \mathrm{d}\boldsymbol{q}'_s \mathrm{d}\boldsymbol{q}'_i \iiiint \mathrm{d}\omega_s \mathrm{d}\omega_i \mathrm{d}\omega'_s \mathrm{d}\omega'_i \\ \times \delta(\boldsymbol{q}_s - \boldsymbol{q}'_s)\, \delta(\boldsymbol{q}_i - \boldsymbol{q}'_i)\, \delta(\omega_s - \omega'_s)\, \delta(\omega_i - \omega'_i)\; |\Phi(\Delta k_z L)|^2 \\ \times \Big[\langle E_V(\boldsymbol{q}_p,\omega_p) E^*_V(\boldsymbol{q}'_p,\omega'_p)\rangle |HH\rangle\langle HH| + \langle E_V(\boldsymbol{q}_p,\omega_p) E^*_H(\boldsymbol{q}'_p,\omega'_p)\rangle |HH\rangle\langle VV| \\ + \langle E_H(\boldsymbol{q}_p,\omega_p) E^*_V(\boldsymbol{q}'_p,\omega'_p)\rangle |VV\rangle\langle HH| + \langle E_H(\boldsymbol{q}_p,\omega_p) E^*_H(\boldsymbol{q}'_p,\omega'_p)\rangle |VV\rangle\langle VV|\Big]. \quad \text{(S1.3)}\end{aligned}$$

Using the transverse momentum and energy conservation relations $\boldsymbol{q}_p^{(\prime)} = \boldsymbol{q}_s^{(\prime)} + \boldsymbol{q}_i^{(\prime)}$ and $\omega_p^{(\prime)} = \omega_s^{(\prime)} + \omega_i^{(\prime)}$, respectively, we obtain

$$\begin{aligned}\rho = |A|^2 \iint \mathrm{d}\boldsymbol{q}_p \mathrm{d}\boldsymbol{q}_- \iint \mathrm{d}\omega_p \mathrm{d}\omega_- \; |\Phi(\Delta k_z L)|^2 \\ \times \Big[\langle E_V(\boldsymbol{q}_p,\omega_p) E^*_V(\boldsymbol{q}_p,\omega_p)\rangle |HH\rangle\langle HH| + \langle E_V(\boldsymbol{q}_p,\omega_p) E^*_H(\boldsymbol{q}_p,\omega_p)\rangle |HH\rangle\langle VV| \\ + \langle E_H(\boldsymbol{q}_p,\omega_p) E^*_V(\boldsymbol{q}_p,\omega_p)\rangle |VV\rangle\langle HH| + \langle E_H(\boldsymbol{q}_p,\omega_p) E^*_H(\boldsymbol{q}_p,\omega_p)\rangle |VV\rangle\langle VV|\Big], \quad \text{(S1.4)}\end{aligned}$$

where we have changed to the integration variables $\boldsymbol{q}_p = \boldsymbol{q}_s + \boldsymbol{q}_i$, $\boldsymbol{q}_- = \boldsymbol{q}_s - \boldsymbol{q}_i$, $\omega_p = \omega_s + \omega_i$ and $\omega_- = \omega_s - \omega_i$. We note that in the integrand, the phase-matching term depends only on

$\boldsymbol{q}_-$ and ω_- [S4–S6], so that $\int \mathrm{d}\boldsymbol{q}_- \int \mathrm{d}\omega_- |\Phi(\Delta k_z L)|^2$ will just result in a scaling factor, which can be absorbed into $|A|^2$ together with other scaling factors resulting from the change of integration variables. Now Eqn. (S1.4) is reduced to

$$\begin{aligned}\rho = |A|^2 &\int_{\Delta \boldsymbol{q}_p} \mathrm{d}\boldsymbol{q}_p \int_{\Delta\omega_p} \mathrm{d}\omega_p \\ &\times \Big[\langle E_V(\boldsymbol{q}_p,\omega_p) E_V^*(\boldsymbol{q}_p,\omega_p)\rangle |HH\rangle\langle HH| + \langle E_V(\boldsymbol{q}_p,\omega_p) E_H^*(\boldsymbol{q}_p,\omega_p)\rangle |HH\rangle\langle VV| \\ &+ \langle E_H(\boldsymbol{q}_p,\omega_p) E_V^*(\boldsymbol{q}_p,\omega_p)\rangle |VV\rangle\langle HH| + \langle E_H(\boldsymbol{q}_p,\omega_p) E_H^*(\boldsymbol{q}_p,\omega_p)\rangle |VV\rangle\langle VV| \Big], \qquad \text{(S1.5)}\end{aligned}$$

where the integration regions $\Delta\boldsymbol{q}_p$ and $\Delta\omega_p$ are the angular and spectral bandwidth of the components of the pump beam that participate in the SPDC process, respectively. These terms are denoted by $\Delta\boldsymbol{q}_p = \Delta\boldsymbol{q}_s + \Delta\boldsymbol{q}_i$ and $\Delta\omega_p = \Delta\omega_s + \Delta\omega_i$, where $\Delta\boldsymbol{q}_{s(i)}$ and $\Delta\omega_{s(i)}$ correspond to the size of the collection apertures in the momentum space and the bandwidth of the spectral filters inserted into the signal and idler arms, respectively.

The terms $\langle E_V(\boldsymbol{q}_p,\omega_p) E_V^*(\boldsymbol{q}_p,\omega_p)\rangle$ and $\langle E_H(\boldsymbol{q}_p,\omega_p) E_H^*(\boldsymbol{q}_p,\omega_p)\rangle$ are simply the intensity of the corresponding spatiotemporal mode of the pump $E_0(\boldsymbol{q}_p,\omega_p)$ and they are written as

$$\langle E_V(\boldsymbol{q}_p,\omega_p) E_V^*(\boldsymbol{q}_p,\omega_p)\rangle = \langle E_H(\boldsymbol{q}_p,\omega_p) E_H^*(\boldsymbol{q}_p,\omega_p)\rangle = |E_0(\boldsymbol{q}_p,\omega_p)|^2/2. \qquad \text{(S1.6)}$$

The terms $\langle E_V(\boldsymbol{q}_p,\omega_p) E_H^*(\boldsymbol{q}_p,\omega_p)\rangle$ and $\langle E_H(\boldsymbol{q}_p,\omega_p) E_V^*(\boldsymbol{q}_p,\omega_p)\rangle$ characterize the relative phase ϕ between the V- and H-polarized components of the same spatiotemporal mode of the pump $E_0(\boldsymbol{q}_p,\omega_p)$ and they can be used to describe the polarization of that specific spatiotemporal mode. Although the pump polarization are set at 45° or −45°, the V- and H-polarized components can acquire different phases after entering the BBO crystals due to birefringence and dispersion. As a result, the relative phase become dependent on the spatiotemporal mode of the pump:

$$\langle E_V(\boldsymbol{q}_p,\omega_p) E_H^*(\boldsymbol{q}_p,\omega_p)\rangle = \langle E_H(\boldsymbol{q}_p,\omega_p) E_V^*(\boldsymbol{q}_p,\omega_p)\rangle^* = |E_0(\boldsymbol{q}_p,\omega_p)|^2 e^{i\phi(\boldsymbol{q}_p,\omega_p)}/2. \qquad \text{(S1.7)}$$

Now we normalize and rewrite Eqn. (S1.5) in the matrix form as

$$\rho = \begin{bmatrix} 1/2 & 0 & 0 & \mu/2 \\ 0 & 0 & 0 & 0 \\ 0 & 0 & 0 & 0 \\ \mu^*/2 & 0 & 0 & 1/2 \end{bmatrix}, \qquad \text{(S1.8)}$$

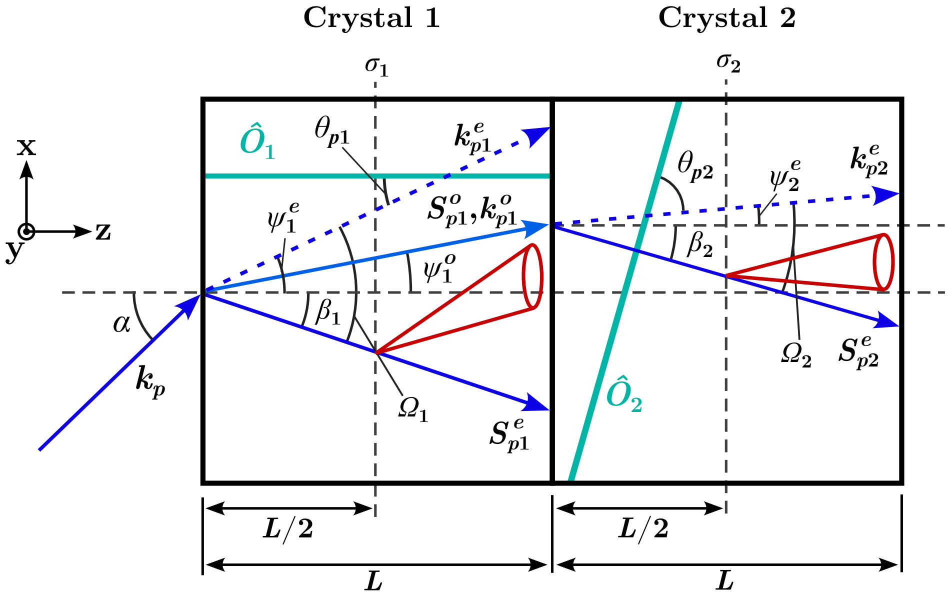

FIG. S1. Schematic diagram illustrating the theoretical model used to calculate relative phase $\phi(\boldsymbol{q}_p, \omega_p)$.

where we have taken $|A|^2 \int_{\Delta \boldsymbol{q}_p} \mathrm{d}\boldsymbol{q}_p \int_{\Delta\omega_p} \mathrm{d}\omega_p |E_0(\boldsymbol{q}_p, \omega_p)|^2 = 1$. The quantity μ is then written as

$$\mu = |A|^2 \int_{\Delta \boldsymbol{q}_p} \mathrm{d}\boldsymbol{q}_p \int_{\Delta\omega_p} \mathrm{d}\omega_p |E_0(\boldsymbol{q}_p, \omega_p)|^2 e^{i\phi(\boldsymbol{q}_p,\omega_p)}. \tag{S1.9}$$

$$C = \left| |A|^2 \int_{\Delta \boldsymbol{q}_p} \mathrm{d}\boldsymbol{q}_p \int_{\Delta\omega_p} \mathrm{d}\omega_p |E_0(\boldsymbol{q}_p, \omega_p)|^2 e^{i\phi(\boldsymbol{q}_p,\omega_p)} \right|, \tag{S1.10}$$

It can be shown that μ satisfies $0 \leq |\mu| \leq 1$, with $|\mu| \to 1$ when $\phi(\boldsymbol{q}_p, \omega_p)$ only has negligible variations over the entire integration region, and $|\mu| \to 0$ when $\phi(\boldsymbol{q}_p, \omega_p)$ varies rapidly within the integration region. Moreover, for a two-photon state in the form of (S1.8), μ determines its concurrence $C(\rho) = |\mu|$ and purity $\mathrm{Tr}(\rho^2) = \{1 + |\mu|^2\}/2$.

II. DERIVATION OF RELATIVE PHASE

In Fig. S1 we depict the theoretical model used to derive the expression for $\phi(\boldsymbol{q}_p, \omega_p)$. This model is adapted from the one proposed in Ref. [S2] and we expand it into the case of a pump beam with arbitrary incident angle. The paired-BBO crystal is placed in the x-y plane. The phase-matching condition denotes that in crystal 1, V-polarized component of the pump beam produces H-polarized PDC photon pairs; and in crystal 2, vice-versa. The relevant variables in this derivation are defined as follows:

$\boldsymbol{k}_p$ – Momentum vector of the pump beam outside of the crystal.

$\boldsymbol{q}_p$ – Transverse momentum vector of the pump beam outside of the crystal. Namely, $\boldsymbol{q}_p = k_{px}\hat{\boldsymbol{x}} + k_{py}\hat{\boldsymbol{y}}$.

$\hat{\boldsymbol{O}}_{1(2)}$ – Unit vector for the optics axis of crystal 1 (crystal 2).

$\boldsymbol{k}^e_{p1(2)}$ – Momentum vector of the **extraordinary** polarized pump beam inside crystal 1 (crystal 2).

$\boldsymbol{k}^o_{p1}$ – Momentum vector of the **ordinary** polarized pump beam inside crystal 1.

$\boldsymbol{S}^e_{p1(2)}$ – Poynting vector of the **extraordinary** polarized pump beam inside crystal 1 (crystal 2).

$\boldsymbol{S}^o_{p1}$ – Poynting vector of the **ordinary** polarized pump beam inside crystal 1.

α – Angle between $\boldsymbol{k}_p$ and $\hat{\boldsymbol{z}}$.

γ – Angle between $\boldsymbol{q}_p$ and $\hat{\boldsymbol{x}}$.

$\theta_{p1(2)}$ – Angle between $\boldsymbol{k}^e_{p1(2)}$ and $\hat{\boldsymbol{O}}_{1(2)}$.

$\psi^e_{p1(2)}$ – Angle between $\boldsymbol{k}^e_{p1(2)}$ and $\hat{\boldsymbol{z}}$.

ψ^o_{p1} – Angle between $\boldsymbol{S}^o_{p1}$, $\boldsymbol{k}^o_{p1}$ and $\hat{\boldsymbol{z}}$.

$\beta_{1(2)}$ – Angle between $\boldsymbol{S}^e_{p1(2)}$ and $\hat{\boldsymbol{z}}$.

$\Omega_{1(2)}$ – Angle between $\boldsymbol{S}^e_{p1(2)}$ and $\boldsymbol{k}^e_{p1(2)}$.

Θ – Angle between $\hat{\boldsymbol{O}}_{1(2)}$ and the x-y plane. This quantity is the same for both crystal since they are cut the same way.

L – Length of crystal 1 and crystal 2.

$\sigma_{1(2)}$ – The plane across the middle point of crystal 1 (crystal 2).

$\Phi_{1(2)}$ – The phase accumulated by the V(H)-polarized pump beam in crystal 1(2) until reaching $\sigma_{1(2)}$.

$n_{e(o)}$ – Refractive index of the extraordinary (ordinary) beam.

According to the laws of refraction and birefringence, some of the above variables will have the following relations [S7]:

$$\psi_{p1}^{o} = \sin^{-1}\left[\frac{\sin\alpha}{n_o(\omega_p)}\right] \tag{S2.1}$$

$$\psi_{p1}^{e} = \sin^{-1}\left[\frac{\sin\alpha}{n_e(\theta_1,\omega_p)}\right] \tag{S2.2}$$

$$n_e(\theta_1,\omega_p) = n_o(\omega_p)\sqrt{\frac{1+\tan^2\theta_1}{1+[n_o(\omega_p)\tan\theta_1/\bar{n_e}(\omega_p)]^2}} \tag{S2.3}$$

$$\Omega_1 = \theta_1 - \tan^{-1}\left[\frac{n_o^2(\omega_p)}{\bar{n_e}^2(\omega_p)}\tan(\theta_1)\right] \tag{S2.4}$$

$$\beta_1 = \Omega_1 - \psi_{p1}^{e} \tag{S2.5}$$

$$\psi_{p2}^{e} = \sin^{-1}\left[\frac{n_o(\omega_p)\sin\psi_{p1}^{o}}{n_e(\theta_2,\omega_p)}\right] \tag{S2.6}$$

$$n_e(\theta_2,\omega_p) = n_o(\omega_p)\sqrt{\frac{1+\tan^2\theta_2}{1+[n_o(\omega_p)\tan\theta_2/\bar{n_e}(\omega_p)]^2}} \tag{S2.7}$$

$$\Omega_2 = \theta_2 - \tan^{-1}\left[\frac{n_o^2(\omega_p)}{\bar{n_e}^2(\omega_p)}\tan(\theta_2)\right] \tag{S2.8}$$

$$\beta_2 = \Omega_2 - \psi_{p2}^{e} \tag{S2.9}$$

In addition, the vectors for pump beam momentum and optic axes are written in the Cartesian coordinate representation as:

$$\hat{\boldsymbol{k}}_p = (\sin\alpha\cos\gamma, \sin\alpha\sin\gamma, \cos\alpha) \tag{S2.10}$$

$$\hat{\boldsymbol{k}}_{p1}^{e} = (\sin\psi_{p1}^{e}\cos\gamma, \sin\psi_{p1}^{e}\sin\gamma, \cos\psi_{p1}^{e}) \tag{S2.11}$$

$$\hat{\boldsymbol{k}}_{p2}^{e} = (\sin\psi_{p2}^{e}\cos\gamma, \sin\psi_{p2}^{e}\sin\gamma, \cos\psi_{p2}^{e}) \tag{S2.12}$$

$$\hat{\boldsymbol{O}}_1 = (0, \cos\Theta, \sin\Theta) \tag{S2.13}$$

$$\hat{\boldsymbol{O}}_2 = (\cos\Theta, 0, \sin\Theta) \tag{S2.14}$$

from the above expressions, we have

$$\begin{aligned}\cos\theta_1 &= \hat{\boldsymbol{k}}_{p1}^{e}\cdot\hat{\boldsymbol{O}}_1 \\ &= \sin\psi_{p1}^{e}\sin\gamma\cos\Theta + \cos\psi_{p1}^{e}\sin\Theta \qquad \text{(S2.15)}\\ \cos\theta_2 &= \hat{\boldsymbol{k}}_{p2}^{e}\cdot\hat{\boldsymbol{O}}_2 \\ &= \sin\psi_{p2}^{e}\sin\gamma\cos\Theta + \cos\psi_{p2}^{e}\sin\Theta \qquad \text{(S2.16)}\end{aligned}$$

Since the down-converted photons are equally likely to be produced anywhere inside the region illuminated by the pump beam, in average, we can assume them to be produced in the middle plane of each crystal (σ_1 and σ_2).

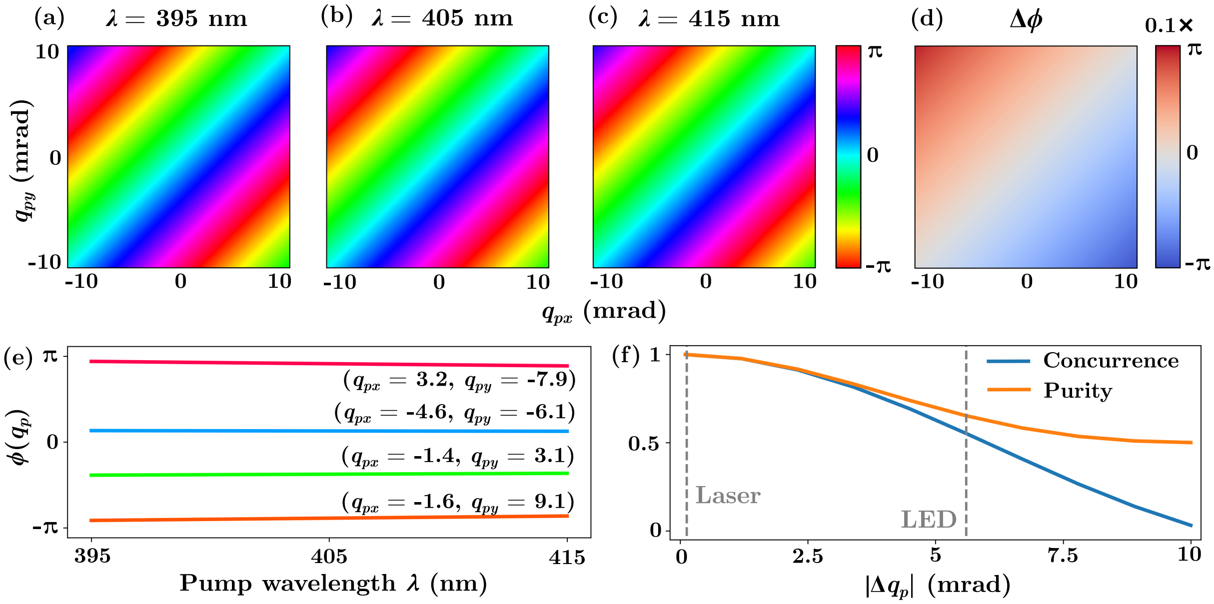

FIG. S2. Theoretical 2D color plot of $\phi(\boldsymbol{q}_p, \omega_p = 2\pi c/\lambda_p)$ for (a) $\lambda_p = 395$ nm (b) $\lambda_p = 405$ nm (c) $\lambda_p = 415$ nm. (d) Theoretical 2D color plot of $\Delta\phi = \phi(\lambda_p = 415 \text{ nm}) - \phi(\lambda_p = 395 \text{ nm})$. (e) Theoretical plots of $\phi(\boldsymbol{q}_p)$ at different pump wavelengths at four randomly chosen angular values. (f) Theoretical plots of concurrence and purity for different angular bandwidths of the pump. The grey dashed lines indicate the cases for laser and LED pump in our experiments.

Now $\phi(\boldsymbol{q}_p, \omega_p)$ is equivalent to the difference between Φ_1 and Φ_2, which is written as

$$\phi(\boldsymbol{q}_p, \omega_p) = \Phi_1 - \Phi_2 \tag{S2.17}$$

$$\Phi_1 = \frac{2\pi n_e(\theta_1, \omega_p)}{\lambda_p} \frac{\cos\Omega_1}{\cos\beta_1} \frac{L}{2} \tag{S2.18}$$

$$\Phi_2 = \frac{2\pi n_e(\theta_2, \omega_p)}{\lambda_p} \frac{\cos\Omega_2}{\cos\beta_2} \frac{L}{2} \tag{S2.19}$$

Now we can compute the dependence of $\phi(\boldsymbol{q}_p, \omega_p)$ on different spatiotemporal modes of the pump by varying the values of α, γ, ω_p.

In Fig. S2(a)-(c) we depict the relative phase $\phi(\boldsymbol{q}_p, \omega_p = 2\pi c/\lambda_p)$ for different values of λ_p. In Fig. S2(d) we depict the difference in ϕ between $\lambda_p = 395$ nm and $\lambda_p = 415$ nm. In Fig. S2(e) we depict the values of ϕ at different pump wavelengths for four randomly chosen angular values. It can be seen that the values of ϕ over the computed angular spectrum remain almost constant over the 20 nm wavelength bandwidth centered around 405 nm, with the maximum difference of ϕ being around 0.1π rad. This is because, for BBO crystals, the refractive index change introduced by birefringence is typically much larger than that

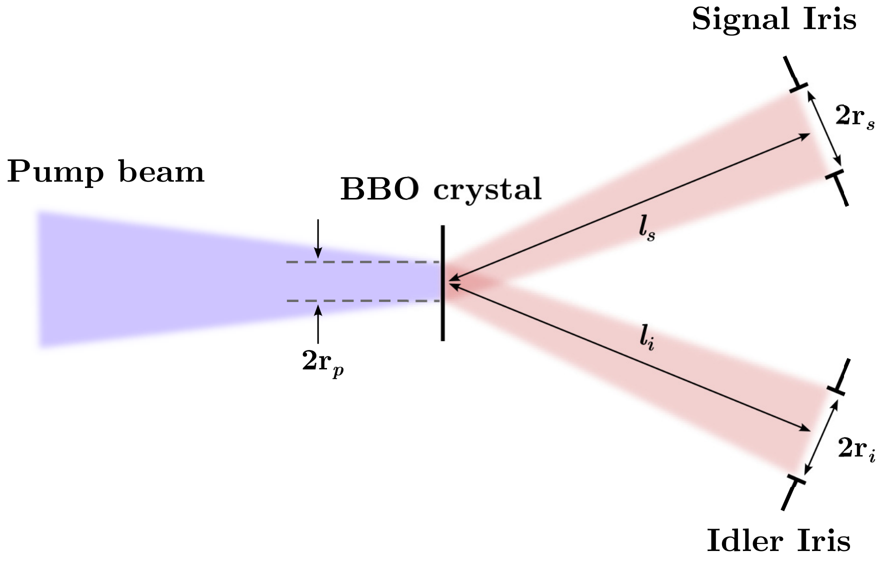

FIG. S3. Schematic diagram illustrating the theoretical model used to estimate the effective angular bandwidth of the LED pump $\Delta \boldsymbol{q}_p$.

introduced by dispersion near the 405 nm region. In Fig. S2(f) we depict the values of concurrence and purity at different angular bandwidths of the pump. As shown by the plot, the concurrence and purity decrease as the angular bandwidth of the pump increases. In other words, averaging over different spatiotemporal modes with different phases reduces the polarization entanglement of the two-photon state.

Since it has been shown that ϕ is basically independent of ω_p, we rewrite (S1.9) as

$$\mu = |A|^2 \int_{\Delta \boldsymbol{q}_p} \mathrm{d}\boldsymbol{q}_p e^{i\phi(\boldsymbol{q}_p, \omega_{p0}=2\pi c/\lambda_{p0})}, \tag{S2.20}$$

where $\lambda_{p0} = 405$ nm and by assuming that $E_0(\boldsymbol{q}_p, \omega_p)$ is slowly-varying over the integrated spatiotemporal bandwidth, $\int d\omega_p \ |E_0(\boldsymbol{q}_p, \omega_p)|^2$ results in a scaling factor that is absorbed into $|A|^2$. The integration region $\Delta \boldsymbol{q}_p$ is estimated according to the experimental conditions, as shown in the next section.

III. ESTIMATION OF THE EFFECTIVE ANGULAR BANDWIDTH OF THE PUMP

In Fig. S3 we depict an intuitive picture to estimate the effective angular bandwidth of the LED pump $\Delta \boldsymbol{q}_p$. We first place a variable iris in the signal arm and adjust the size

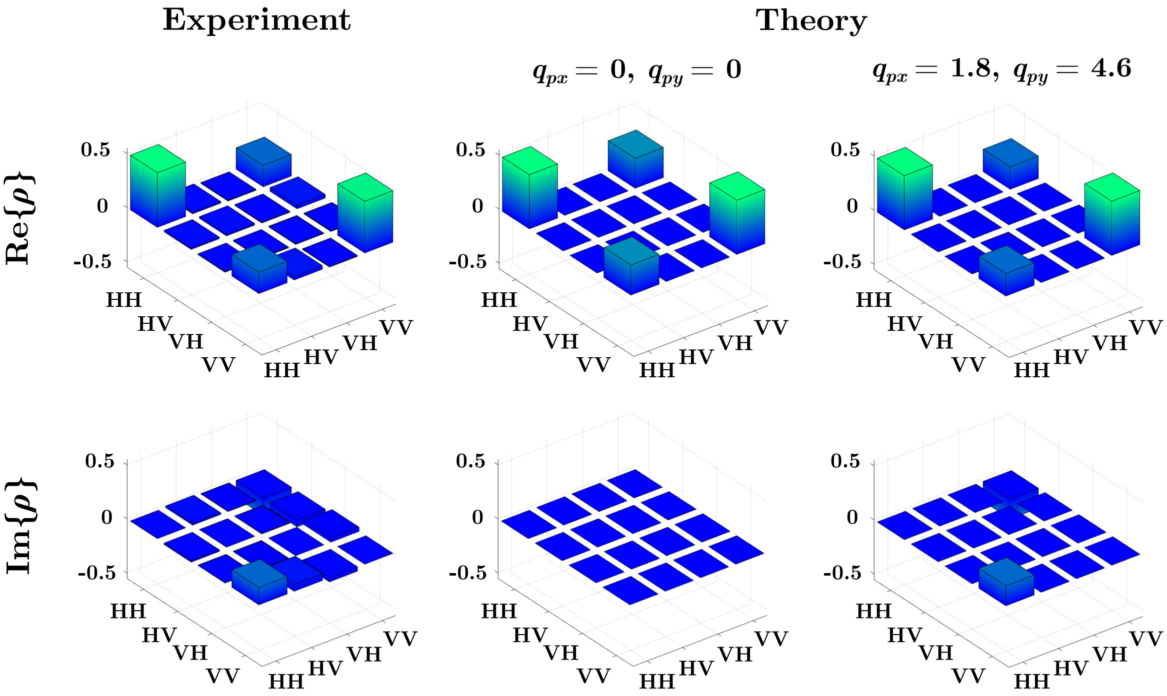

FIG. S4. Experimentally measured and theoretically predicted density matrices for LED-pumped SPDC. The theoretically predicted ones are estimated with integration regions centered at different angular positions represented by $(\boldsymbol{q}_{px},\ \boldsymbol{q}_{py})$. The units for $\boldsymbol{q}_{px}$ and $\boldsymbol{q}_{py}$ are both mrad.

until it barely blocks the down-conversion beam; we denote the radius of this iris as r_s and the distance between the crystal and the signal iris as l_s, respectively. Then the angular bandwidth of the signal beam can be estimated to be $|\Delta \boldsymbol{q}_s| = (\mathrm{r}_s - \mathrm{r}_p)/l_s$, where r_p is the diameter of the pump beam at the crystal plane. Similarly, to estimate the angular bandwidth of the idler beam, we have $|\Delta \boldsymbol{q}_s| = (\mathrm{r}_i - \mathrm{r}_p)/l_i$, where r_i and l_i are the size of the iris on the idler arm and the distance between the crystal and the idler iris. The effective angular bandwidth of the pump can now be estimated as $|\Delta \boldsymbol{q}_p| \approx |\Delta \boldsymbol{q}_s| + |\Delta \boldsymbol{q}_i|$.

In our setup, $|\Delta \boldsymbol{q}_p|$ is estimated to be 5.6 mrad. For a laser pump, one can calculate the integration upper limit by approximating it to the divergence half-angle of a Gaussian beam at the waist [S8], in our case, $|\Delta \boldsymbol{q}_p|_{\mathrm{laser}})$ is estimated to be 0.13 mrad.

IV. DIFFERENCES BETWEEN THE THEORETICAL AND EXPERIMENTAL RESULTS FOR LED-PUMPED SPDC

In the main text, we notice that the theoretically measured density matrix for LED-pumped SPDC contains non-zero off-diagonal elements in the imaginary part, while the theoretically predicted one does not. This can be explained by an alignment imperfection of the LED pump beam in the experimental setup.

In producing the results shown in Fig. 2 of the main text, we estimated μ using

$$\mu = |A|^2 \int_{0<|\boldsymbol{q}_p|<|\Delta\boldsymbol{q}_p|} \mathrm{d}\boldsymbol{q}_p e^{i\phi(\boldsymbol{q}_p,\omega_{p0}=2\pi c/\lambda_{p0})}, \tag{S4.1}$$

which assumes perfect alignment in the sense that the spatiotemporal modes of the pump beam that participate in the SPDC are centered around $(\boldsymbol{q}_{px} = 0, \boldsymbol{q}_{py} = 0)$. If the integration region is instead centered at $(\boldsymbol{q}_{px} = 1.8 \text{ mrad}, \boldsymbol{q}_{py} = 4.6 \text{ mrad})$, which corresponds to a 5 mrad angular deviation of the pump beam, we can obtain a density matrix that resembles the experimentally measured one. After accounting for the angular deviation, the theoretically predicted concurrence and purity are 0.553 and 0.653, respectively. Note that these results are close to those presented in the main text, which assumes perfect alignment and gives the theoretically predicted concurrence and purity as 0.552 and 0.652, respectively. The fidelity of the experimentally measured density matrix to the theoretically predicted one is now 97.92 % (see Fig. S4)

[S1] P. G. Kwiat, E. Waks, A. G. White, I. Appelbaum, and P. H. Eberhard, Ultrabright source of polarization-entangled photons, Physical Review A **60**, R773 (1999).

[S2] J. B. Altepeter, E. R. Jeffrey, and P. G. Kwiat, Phase-compensated ultra-bright source of entangled photons, Optics Express **13**, 8951 (2005).

[S3] R. Rangarajan, M. Goggin, and P. Kwiat, Optimizing type-I polarization-entangled photons, Optics Express **17**, 18920 (2009).

[S4] C. K. Law and J. H. Eberly, Analysis and interpretation of high transverse entanglement in optical parametric down conversion, Phys. Rev. Lett. **92**, 127903 (2004).

[S5] M. P. van Exter, A. Aiello, S. S. R. Oemrawsingh, G. Nienhuis, and J. P. Woerdman, Effect of spatial filtering on the schmidt decomposition of entangled photons, Phys. Rev. A **74**, 012309 (2006).

[S6] G. Kulkarni, P. Kumar, and A. K. Jha, Transfer of temporal coherence in parametric down-conversion, J. Opt. Soc. Am. B **34**, 1637 (2017).

[S7] S. Castelletto, I. P. Degiovanni, A. Migdall, and M. Ware, On the measurement of two-photon single-mode coupling efficiency in parametric down-conversion photon sources, New Journal of Physics **6**, 87 (2004).

[S8] B. E. Saleh and M. C. Teich, *Fundamentals of Photonics* (John Wiley & Sons, 2019).

Chapter 3

Imaging spatial-polarization structures in two-photon entanglement

Having realized that the spatial properties of the pump may only be deterministically mapped onto the resulting polarization entanglement, I proposed to experimentally characterize this spatial-polarization structure so that in the future, one can (i) engineer a high-dimensional entangled state with desired structure across multiple DoFs for the use of novel quantum information processing protocols; or (ii) completely compensate for any cross influence between different DoFs so that highly polarization-entangled two-photon states can be generated from SPDC pumped by light with arbitrary spatial and temporal bandwidths.

I formalized this research idea through discussions with Dr. Girish Kulkarni and Prof. Robert Boyd. During the discussion, I realized that such an experiment can be done more efficiently using Tpx3Cam. This device, which is developed by Prof. Andrei Nomerotski, is a data-driven camera capable of time-stamping single-photon events at each pixel. It allows resolving photon coincidences across all pixels illuminated by the SPDC field simultaneously, thereby significantly enhancing the speed of entanglement certification measurements. Through the work of Dr. Jeremy Upham and Prof. Robert Boyd, we established collaborations with Dr. Duncan England, Prof. Andrei Nomerotski, and Prof. Ebrahim Karimi to gain access to Tpx3Cam, including necessary accessories and software.

I re-designed the experimental setup based on the one used in Chapter 2. To achieve optimal spatial resolution, I designed lens-imaging systems that magnify the SPDC field for maximal fill of the Tpx3Cam sensor, while ensuring minimal overlap between signal and idler fields. I built the setup shown in Fig. 1 by myself, and the one shown in Fig. 4 with the assistance of Mr. Issac Soward, an undergraduate student whom I was mentoring at the time. With instructions and training from Prof. Andrei Nomerotski and Dr.

Yingwen Zhang, I integrated the Tpx3Cam system with the optical setup. Constrained partially by the software available at the time, I collected terabytes of raw data due to the substantial single-photon events detected by Tpx3Cam in each spatial and polarization measurement basis. To reduce memory burden, I developed a Python-based system that first filters and saves only the immediately relevant parameters, which significantly reduces the effective data size. Furthermore, I compiled Python programs with parallel processing functionality and adopted a two-pointer coincidence counting algorithm to accelerate data processing. It is worth mentioning that more exquisite software now exists for general-purpose Tpx3Cam detections. Nevertheless, my efforts at the time had significantly accelerated the completion of this work.

I analyzed the results through discussions with Dr. Girish Kulkarni and Dr. Jeremy Upham. I wrote the first draft of the manuscript, which had undergone extensive revisions with contributions from all co-authors. Dr. Duncan England, Prof. Andrei Nomerotski, Prof. Ebrahim Karimi, and Prof. Robert Boyd supervised the research. This work is currently under review at Physical Review Applied.

Full-field mapping of spatially varying polarization entanglement generated from spontaneous parametric down-conversion

Cheng Li,[1, *] Girish Kulkarni,[1, 2] Isaac Soward,[1] Yingwen Zhang,[1, 3] Jeremy Upham,[1]
Duncan England,[3] Andrei Nomerotski,[4, 5] Ebrahim Karimi,[1, 3, 6] and Robert Boyd[1, 7, †]
[1] *Department of Physics, University of Ottawa, Ottawa, ON K1N 6N5, Canada*
[2] *Department of Physics, Indian Institute of Technology Ropar, Rupnagar, Punjab 140001, India.*
[3] *National Research Council, Ottawa, ON K1A 0R6, Canada*
[4] *Faculty of Nuclear Sciences and Physical Engineering,*
Czech Technical University, Prague 115 19, Czech Republic
[5] *Department of Electrical and Computer Engineering,*
Florida International University, Miami, FL 33174, USA
[6] *Institute for Quantum Studies, Chapman University, Orange, CA 92866, USA*
[7] *Institute of Optics, University of Rochester, Rochester, NY 14627, USA*

Two-photon states generated from spontaneous parametric down-conversion (SPDC) can display entanglement in all degrees of freedom (DoFs) of light, including spatial, temporal, and polarization. The coupling between different DoFs of a two-photon state has been shown to display rich structures that enable novel and robust information processing schemes. While existing literature has studied these couplings by post-selecting the SPDC field, a comprehensive understanding of the inherent spatial-polarization coupling produced in the SPDC process is still lacking. This work produces a full spatial map of the polarization entanglement generated across the entire SPDC field. We observe an entire class of near-maximally polarization-entangled states with an average concurrence of 0.8303 ± 0.0004, which, together with a certified spatial dimensionality of 148, could potentially offer access to a 251-dimensional hyperentanglement. The spatial-polarization coupling manifests as radially or linearly varying polarization-entangled states, whose wavefunctions are dependent on the transverse momenta of the down-converted photons and the pump beam, respectively. Our study lays important groundwork for further exploiting the coupling between entanglement in different DoFs for future quantum technologies.

I. INTRODUCTION

Spontaneous parametric down-conversion (SPDC) has been a major workhorse for generating entangled tw-photon states [1–3], enabling numerous applications in quantum information processing. In SPDC, a photon from a pump beam, which has a higher optical frequency, interacts with a second-order nonlinear medium to be annihilated and produce a pair of down-converted photons with lower frequencies [2]. The down-converted photons, which are commonly referred to as signal and idler, can exhibit entanglement in all degrees of freedom (DoFs) of light, including spatial, temporal, and polarization.

Studying the coupling between different DoFs is a crucial step towards a comprehensive understanding of SPDC-based entanglement generation and engineering novel entangled photon states for practical applications [4, 5]. An important aspect of this subject is the coupling between spatial and polarization DoFs in SPDC. Such cross-DoF couplings can be exploited to enable novel and efficient quantum information applications. For instance, it was shown that quantum correlations across spatial and polarization DoFs can enable novel and more robust information encoding schemes and demonstrate topological resilience against environmental noise [6]. Moreover, the spatially varying polarization correlations in a photonic entangled state can also be harnessed to enable quantum holographic imaging [7] or engineer photonic cluster states for efficient quantum computation [8, 9]. From a fundamental perspective, studies have shown that spatial modes of the pump beam can influence the polarization entanglement of the down-converted photons [10, 11], indicating the opportunity of directly engineering the couplings between different DoFs in a photonic entangled state, or encoding phase images in the two-photon correlations [12] by shaping the pump beam.

The spatial-polarization coupling in SPDC commonly manifests as two-photon states with spatially varying polarization entanglement. Although one can readily produce these features from SPDC using a paired crystal configuration [13, 14], the large spatial dimensionality of the SPDC field hinders the efficient characterization of them. For instance, a full state tomography for a bipartite state with local dimensionality d in a single DoF requires $\mathcal{O}(d^4)$ single-outcome projective measurements [15–17]. Since the total dimensionality of a quantum state scales with the product of dimensionality in each constituent DoF, the need to address correlations, both within and between different DoFs, only adds to the complexity of the problem. Without comprehensively resolving the polarization entanglement produced in each spatial mode, the rich structures resulting from the

---

[*] cli221@uottawa.ca
[†] rboyd@uottawa.ca

coupling between different DoFs reduce to a mixture of distinguishable states. As a result, the full potential of SPDC-induced spatial-polarization coupling becomes inaccessible, limiting its application in practical quantum devices. For instance, a recent work indicates that even though each spatial mode in a multimode pump beam can generate maximum polarization entanglement through SPDC, detecting the two-photon states without resolving individual spatial modes can make the entanglement appear deteriorated [10].

Over the past decade, several studies have employed Tpx3Cam, a data-driven camera capable of time-stamping single photons [18–20], to enable rapid characterization of photonic entangled states produced from SPDC [21–23]. However, these works have not fully explored the coupling between different DoFs. Specifically, Ref. [21, 22] have focused only on the polarization DoF or the spatial DoF, respectively, while their photon pair sources are capable of producing spatially varying polarization-entangled states. As a result, the potential of the embedded spatial-polarization coupling has not been addressed. Furthermore, the entangled states produced in Ref. [21, 23] are first spatially postselected using single-mode fibers or polarization-maintaining fibers before being imaged onto the Tpx3Cam, and any spatial structures in the resulting polarization are imprinted by external modulation devices. Doing so effectively reduces the spatial dimensionality and obscures any spatial-polarization coupling imposed by the generation process.

In this work, we employ Tpx3Cam to comprehensively characterize the spatially varying polarization entanglement that is natively produced from SPDC. In contrast to earlier works, we image the full spatial field of SPDC without any post-processing on the resulting two-photon states. By performing spatially-resolved polarization state tomography, we confirm the generation of near-maximally polarization-entangled states across the entire spatial profile of the SPDC field, with an average concurrence of 0.8303 ± 0.0004. Importantly, we present a complete spatial map of the polarization state generated from SPDC, revealing how polarization entanglement depends on the transverse momenta of the down-converted photons throughout the entire spatial profile of the SPDC field. Moreover, using a weakly focused pump beam, we experimentally characterize the dependence of polarization entanglement on the angular spectrum of the pump beam. Additionally, we have estimated a maximum attainable dimensionality of spatial entanglement to be 148, which, combined with the effective dimensionality in the polarization DoF, indicates a total attainable dimensionality of 251. Our results advance the fundamental understanding of the interplay between different DoFs of a photonic entangled state, paving the way for novel applications in photonic quantum information processing.

II. EXPERIMENTAL SETUP

Fig. 1(a) depicts our experimental setup. An ultraviolet continuous-wave laser emits the pump beam with a center wavelength of 405 nm, a bandwidth of 2 nm, and a power of 20 mW. The pump beam is made polarized at 45° using a polarizing beam splitter (PBS) and a half-wave plate (HWP). A 5-mm temporal compensator (TC) quartz crystal introduces a time delay between the horizontal (H-) and vertical (V-) components of the pump beam, which pre-compensates for the temporal walk-off that the two orthogonal polarization components are expected to subsequently gather inside the BBO double-crystal [24]. The BBO crystals are each 0.5-mm-thick and identically cut for type-I phase-matching, with their optical axes oriented perpendicularly to one another [13]. A 45°-polarized photon from the pump beam can then be down-converted in either crystal with equal probability to produce a pair of H-polarized or V-polarized photons. In the experiment, we orient the double-crystal for near-collinear phase matching. The down-converted photons are separated from the pump beam using a dichroic mirror (DM), and then probabilistically split into two arms using a non-polarizing beam splitter (BS). We ignore the cases wherein both the down-converted photons exit the same port of the BS, and denote photons that are reflected as *signal* and those that are transmitted as *idler*. This beam-splitting scheme ensures that measuring the correlation between the signal arm and the idler arm resolves the full spatial profile of the SPDC. Although the probabilistic splitting reduces the coincidence rates by 50%, it does not affect the quality of entanglement or the measured spatial-polarization structure compared to those obtained with deterministic splitting, as can be seen later in Fig. 2 and Fig. 4. In the low-gain regime, the output state $|\Psi\rangle$ in the far-field can be written in the joint spatial-polarization basis as

$$|\Psi\rangle = \frac{1}{\sqrt{2}} \sum_{\boldsymbol{p}_s,\boldsymbol{p}_i} c_{\boldsymbol{p}_s,\boldsymbol{p}_i} \Big[|H,\boldsymbol{p}_s,H,\boldsymbol{p}_i\rangle + \mathrm{e}^{i\phi(\boldsymbol{p}_s,\boldsymbol{p}_i)} |V,\boldsymbol{p}_s,V,\boldsymbol{p}_i\rangle \Big], \tag{1}$$

where $\boldsymbol{p}_{s(i)}$ represents the transverse momentum of the signal (idler) photon and $c_{\boldsymbol{p}_s,\boldsymbol{p}_i}$ are complex coefficients. The quantity $\phi(\boldsymbol{p}_s,\boldsymbol{p}_i)$ represents a phase difference between the orthogonal polarization components of the state, which is dependent on the transverse momentum of the signal and the idler photons [25]. In what follows,

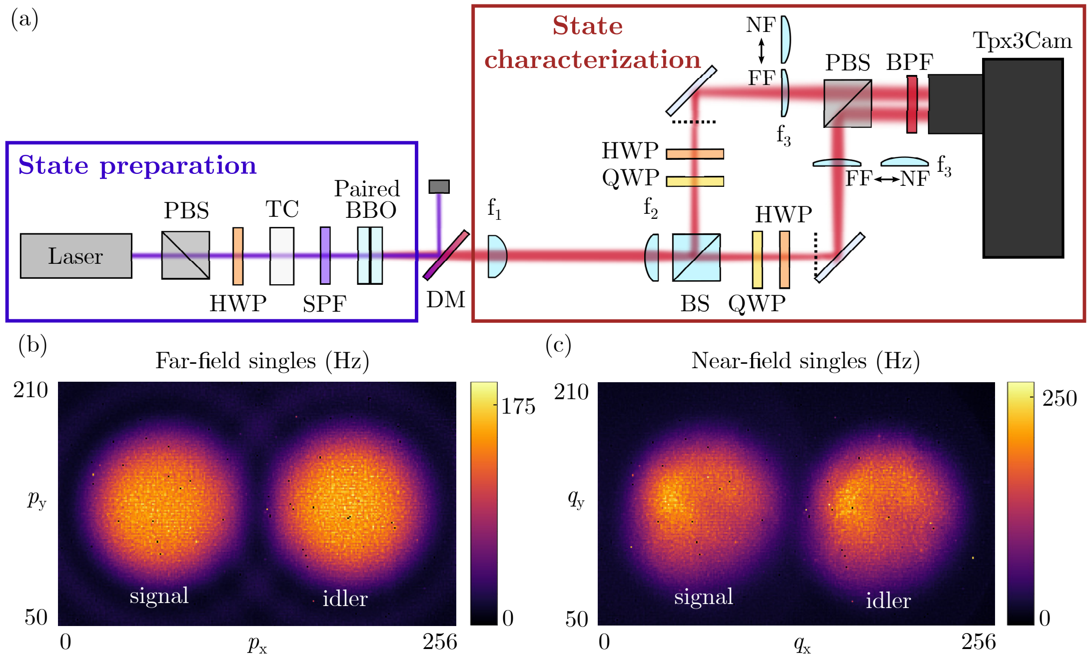

FIG. 1. (a) Schematic of the experimental setup. The β-barium borate (BBO) double-crystal produces a two-photon state, which exhibits spatially varying polarization entanglement. The Tpx3Cam captures the two-photon field in the momentum or position basis through different lens configurations and in different polarization bases through combinations of the quarter-wave plate (QWP), half-wave plate (HWP), and polarizing beam splitter (PBS). TC: temporal compensator, SPF: short-pass filter with cutoff wavelength at 500 nm, DM: dichroic mirror, BS: beam splitter, BPF: band-pass filter centered at 800 nm with a bandwidth of 40 nm. $f_1 = 50$ mm, $f_2 = 100$ mm. $f_3 = 150$ mm for far-field measurements or 75 mm for near-field measurements. Dashed lines represent the intermediate planes imaging the near-field of the crystal using f_1 and f_2. (b-c) Time-stamp histogram of photons detected in the far-field and near-field of the crystal, representing projection onto the momentum (p) and position (q) bases of the two-photon state.

we refer to ϕ as the *two-photon polarization phase*.

The signal and idler photons then propagate through a quarter-wave plate (QWP) and a HWP before they are either transmitted or reflected by a PBS. The photons finally pass through a bandpass filter with a center wavelength of 800 nm and full width at half maximum (FWHM) bandwidth of 40 nm before being detected by the Tpx3Cam. To characterize entanglement in the polarization DoF, we measure the polarization correlation between each pair of momentum-correlated signal and idler photons. We first image the far-field of the crystal onto the Tpx3Cam using the combination of $f_1 = 50$ mm, $f_2 = 100$ mm, and $f_3 = 150$ mm lenses, and then acquire data for 16 different combinations of orientations of HWPs and QWPs, each for 1 minute. These polarization measurements allow us to reconstruct the polarization density matrices corresponding to all pairs of momentum-anticorrelated photons through quantum state tomography, which characterizes polarization entanglement. To characterize the state dimensionality in the spatial DoF, we measure the spatial correlation of signal and idler photons in the position basis. We do so by replacing the $f_3 = 150$ mm lenses with $f_3 = 75$ mm ones, thereby imaging the crystal output face (near-field) onto the Tpx3Cam sensor. We then set the HWPs and QWPs to project the polarization in both arms into V and acquire data for 1 minute. Combined with the 16 measurements acquired in polarization characterization, the total required data acquisition time is thus $1 + 16 = 17$ minutes.

The imaging sensor in Tpx3Cam comprises a 256×256 pixel array with a pixel pitch of 55 μm. The pixels in Tpx3Cam are data-driven and individually trigger the registration of photon incidence events when the signal amplitude exceeds a predefined threshold. The camera can be single-photon sensitive with the addition of an image intensifier (Photonis Cricket) and has a single photon temporal resolution of 2 ns [20]. Time-stamping for individual photons can potentially allow for more versatility in data acquisition and analysis compared to frame-based imaging devices. During data acquisition, each incident photon could hit a cluster of pixels due to being amplified by the intensifier. To correct this, we apply a centroiding algorithm that identifies the amplitude-weighed center in each cluster as the true pixel coordinate. We use the time stamp of each centroided pixel as a reference to correct the time walk within the cluster. After centroiding and time walk correction, we apply a two-pointer technique to the sorted time stamps of signal and idler photons and identify events detected within a 10-ns time window as photon coincidences [21]. Although the time walk correction algorithm can reduce the temporal resolution to 8 ns [26, 27], it should not significantly affect the efficiency of the subsequent coincidence counting with our choice of a longer time window. As a result, we obtain an average coincidence rate of approximately 2.7 Hz between two spatially correlated 3 × 3-pixel regions, which have similar sizes with the correlation widths measured at the Tpx3Cam sensor plane (see Appendix A for details). Throughout this paper, we refer to each 3 × 3-pixel region as a superpixel. Moreover, we observe an overall coincidence rate of 3200 Hz between the full signal and idler fields. We note that although the experimentally measured coincidence rate is limited by the 8% overall photon detection efficiency of the Tpx3Cam system [26], our choice of 1-minute data acquisition time has allowed us to obtain enough counts for the relevant results to be statistically valid.

III. RESULTS AND DISCUSSIONS

A. Full spatial mapping of polarization entanglement

Using the setup depicted in Fig. 1(a), we perform quantum state tomography [15] using experimentally measured polarization correlation between each pair of momentum-anticorrelated (diametrically-opposite) superpixels in the far-field and reconstruct the corresponding polarization density matrix. We then compute the concurrence using $C = \max\{0, \lambda_1 - \lambda_2 - \lambda_3 - \lambda_4\}$, where λ's are the eigenvalues of a Hermitian matrix derived from applying Pauli-y operations on reconstructed density matrices [28]. The two-photon polarization phases ϕ are computed as the phase of the $|VV\rangle\langle HH|$ elements of the reconstructed density matrices.

Fig. 2 depicts the full spatial maps of the concurrence C and two-photon polarization phase ϕ in the far field. For illustration purposes, we have mapped all signal-idler pairs to the central coordinates of the superpixels of signal photons. In Fig. 2(c), we also display a two-photon polarization density matrix, which is reconstructed at the center of the SPDC field, with the corresponding signal-idler pair indicated by a black square in Fig. 2(a-b). We calculate an average concurrence of 0.8303 ± 0.0004, which implies strong polarization entanglement with a spatially varying structure across the entire SPDC field.

It is important to note that in Fig. 2(b), the two-photon polarization phase ϕ is highly uniform along the azimuthal direction while displaying a gradient along the radial direction, indicating highly indistinguishable polarization entanglement at each circular region concentric with the SPDC field. Consequently, if each corresponding spatial mode is also highly indistinguishable from one another, the two-photon state can be seen as being hyperentangled [14, 29], which is a tensor product of (i) spatially entangled discrete momentum modes occupying the full spatial field of SPDC; and (ii) polarization-entangled states with a well-defined two-photon polarization phase ϕ. In the following discussions, we characterize the spatial distinguishability between all correlated spatial modes by certifying the spatial dimensionality of the two-photon state, thereby estimating an attainable total dimensionality of the full SPDC field in the joint spatial-polarization basis.

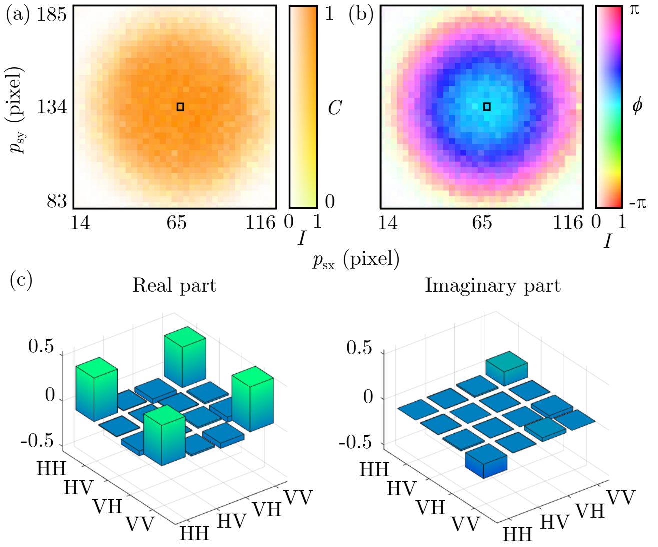

FIG. 2. (a) Concurrence C and (b) two-photon polarization phase ϕ of the two-photon states measured between momentum-correlated superpixels. The pixel coordinates correspond to the central position of the superpixels for signal photons. In the colormap, the saturation depicts the normalized pair generation rate, I, and the hue depicts C and ϕ in (a) and (b), respectively. (c) Real and imaginary parts of the density matrix reconstructed at the center of the SPDC field, the corresponding signal pixel is marked with a black square in (a) and (b).

B. Certifying total attainable dimensionality of in the joint spatial-polarization bases

We characterize the spatial dimensionality of a two-photon state using its Schmidt number. While past studies have estimated this number based on certain prior assumptions about the two-photon state [30–34], some recent studies have demonstrated assumption-free protocols for certifying high dimensionality [35, 36]. In particular, it was shown that measurements in two mutually unbiased bases (MUBs) can efficiently estimate a lower bound for the Schmidt number of an entangled state, thereby certifying high-dimensional entanglement without the need for prior assumptions [35]. In our case, we show that the entanglement dimensionality in the spatial DoF can be certified by measuring the photon correlation in the discrete position basis and the discrete momentum basis, similar to the approach implemented

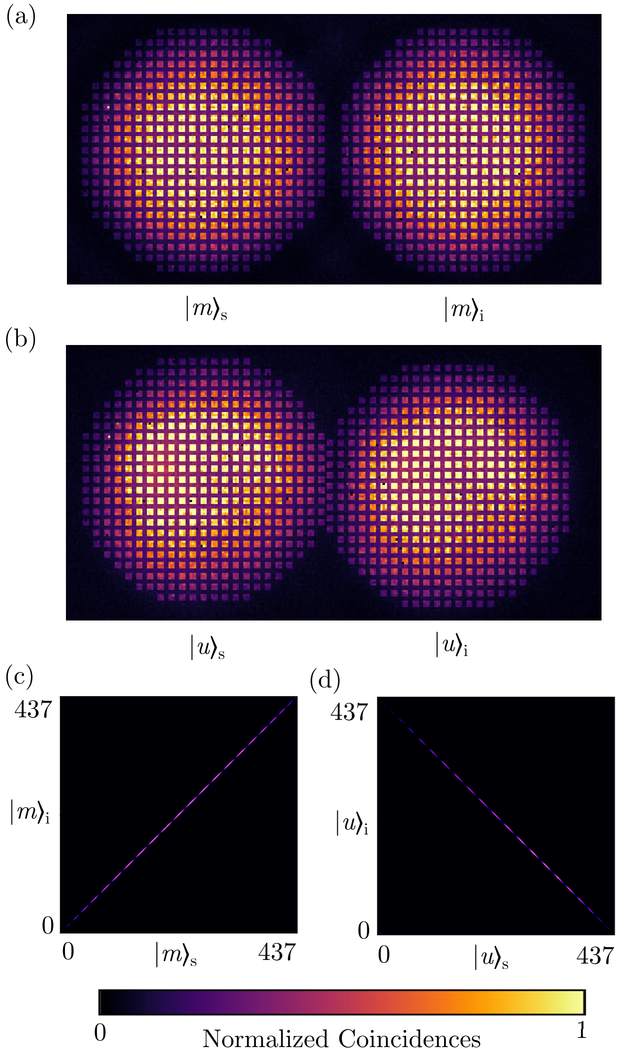

FIG. 3. Schematic depiction of (a) the discrete momentum basis in the far-field and (c) the discrete position basis in the near-field. The corresponding superpixels are depicted in a brightened color scale. Cross-correlations between the spatial modes of signal and idler photons in the (b) momentum basis and (d) position basis.

in Ref. [37].

We denote the spatial modes of the signal(idler) photons in the discrete momentum basis as $\{|m\rangle_{s(i)}\}_{m\in[1,d]}$ and in the discrete position basis as $\{|u\rangle_{s(i)}\}_{u\in[1,d]}$. Based on the experimentally measured spatial correlation widths (see Appendix B for details), individual discrete modes in the Tpx3Cam sensor plane are better approximated by 3×3-pixel large superpixels with 2-pixel separations between adjacent superpixels. We note that since this protocol is sensitive to noise introduced by cross-talk between non-conjugate modes, a different choice in the superpixel size and separation could lead to significant underestimation of the dimensionality. As shown in Fig. 3(a-b), we select two sets of $d = 437$ superpixels evenly distributed over the regions illuminated by signal and idler photons. The cross-correlations between spatial modes of signal and idler photons are used to calculate $\tilde{F}(\rho,\Psi)$, a lower bound for the fidelity of the experimentally measured state ρ to a maximally entangled state $|\Psi\rangle = \sum_{m=1}^{d}\frac{1}{\sqrt{d}}|mm\rangle$. The dimensionality of the spatial entanglement is certified to be at least $k+1$ if k satisfies [35]

$$\tilde{F}(\rho,\Psi) > B_k(\Psi) = \sum_{m=1}^{k}\lambda_m^2 = \frac{k}{d}. \tag{2}$$

Upon analyzing the cross-correlations between selected spatial modes of signal and idler photons, we obtain the correlation matrices shown in Fig. 3(c-d). The fidelity lower bound is then calculated to be $\tilde{F} = 0.3383 > B_{147} = 0.3363$ (see Appendix B for details). In other words, a maximally entangled state has to have more than 147 dimensions to be transformable into our measured state through local operations and classical communication (LOCC). Therefore, the entanglement dimensionality in the spatial DoF is certified to be at least 148, indicating high indistinguishability between all correlated spatial modes.

In principle, the polarization phase ϕ in Eq. 1 can be compensated using spatial light modulators (SLMs) so that it becomes uniform also across all radial positions without reducing the polarization entanglement [7]. Consequently, we expect the attainable total dimensionality of our state to be equal to that of a global hyperentangled state, which is a product of the average dimensionality in the polarization DoF and the certified dimensionality in the spatial DoF, as underscored by the tensor product postulate of quantum physics.

Although two-photon polarization states reside in a two-dimensional Hilbert space, the effective dimensionality may be smaller for non-maximally entangled states. Therefore, it is pertinent to estimate a lower bound of the dimensionality d in the polarization DoF using the relation $\log_2 d \leq E$ [38], where E stands for the entanglement of formation [39]. For two-photon polarization states, the entanglement of formation can be derived from concurrence using [28]

$$E(C) = h\left(\frac{1+\sqrt{1-C^2}}{2}\right), \tag{3}$$

where $h(x) = -x\log_2 x - (1-x)\log_2(1-x)$. The average entanglement of formation is then estimated to be $E = 0.7626 \pm 0.0003$. By multiplying the dimensionality lower bounds in spatial and polarization DoFs, we estimate the total attainable dimensionality of the entangled state to be $148 \times 2^E \approx 251$. We note that this result is likely to still be an underestimation of the actual dimensionality since the dimensionality certification protocol has limited resilience against the cross-talk noise [16, 35, 36], a more accurate estimation may be explored in a future work.

C. Native spatial-polarization coupling in SPDC processes

The spatial-polarization coupling in SPDC has two important aspects. First, the exact form of polarization entanglement depends on the transverse momenta of the *down-converted photons*. This effect, which is displayed in Fig. 2(b), occurs because down-converted photons emitted with different transverse momenta experience angle-dependent refractive indices inside the birefringent nonlinear medium and consequently accumulate different phase retardations between orthogonal polarization components. Consequently, a class of highly entangled states of the form of Eq. (1) with spatially varying ϕ is generated across the spatial profile of the field. While the spatial profile of polarization entanglement in SPDC has been studied for limited spatial regions or specific sets of spatial modes [14, 25], our results present the first full spatial distribution of polarization entanglement in the entire spatial profile of the field, laying the foundation for the controlled generation of desired photonic entangled states.

Phase-matching of the crystal also controls the relation between two-photon transverse momenta and the two-photon polarization phase. As may be noted from Fig. 2(b), the two-photon polarization phase ϕ does not vary over the full range of $-\pi$ to π in the present configuration as a consequence of the near-collinear phase matching condition. In what follows, we modify the experimental setup to show that by tuning the crystal orientation, an altered phase matching condition leads to ϕ varying over the full parameter space in the spatial profile of the field, which allows access to a much wider class of polarization-entangled states.

We depict our modified setup in Fig. 4(a). In order to capture the enlarged far-field image profile in its entirety, we deterministically split the SPDC field into two half-circles using a prism mirror (PM) and recombine the fields onto the Tpx3Cam sensor. We retain the same far-field imaging scheme, such that the two-photon correlation width remains unchanged from the earlier setup, and we again perform spatially resolved polarization state tomography using the same procedure as discussed previously. In Fig. 4(b),(c), and (d), we depict the far-field intensity Tpx3Cam image, concurrence C, and two-photon polarization phase ϕ, respectively. We again observe a strong polarization entanglement in the entire spatial extent of the field with an average concurrence of 0.8847 ± 0.0006. We notice a marginal increase in the average concurrence compared to the result in Sec. III B. This is likely a result of the lower polarization cross-talk since now both signal and idler photons are detected through the transmission port of the PBS. The distribution of ϕ again displays a gradient along the radial direction, but this time with ϕ having an enlarged parameter space spanning from $-\pi$ to π. In other words, the setup produces near-maximally entangled states of Eq. (1) with all possible ϕ. Thus, our setup can be configured to supply any specific state with a desired value of ϕ by post-selecting the corresponding pair of far-field pixels and tuning the phase-matching of the crystal. Such a mechanism can enable encoding spatial mode information in polarization correlations or vice versa, which could have important implications for quantum key distribution protocols using qudit-like states [40]. Furthermore, it is also possible to structure ϕ to have any desired profile by introducing additional phase differences between H- and V-polarized down-converted photons using SLMs to enable holographic quantum imaging [7] with much higher speed. We note that such phase structures are not limited to only manifesting in momentum space. One can observe similar effects in the near field by exploring different SPDC setup geometries. We may explore near-field phase structuring in future work.

The second important aspect of spatial-polarization structure is between the polarization DoF of the down-converted photons and the spatial DoF of the *pump beam*. Specifically, the two-photon polarization phase $\phi(\boldsymbol{p}_s, \boldsymbol{p}_i)$ in Eqn. (1) depends on the transverse momentum of the pump beam since $\boldsymbol{p}_\mathrm{p} = \boldsymbol{p}_s + \boldsymbol{p}_i$ [10]. This relation is first theoretically quantified by Li et al. [10]. Here, to experimentally characterize this influence, we introduce a broader angular spectrum in the pump beam by weakly focusing it using a lens with focal length $f_0 = 100$ mm placed before the crystal. In Fig. 5, we present the influence of the angular spectrum of the pump beam on the spatial structure of the polarization states. In Fig. 5(a) and (b), we show the far-field intensity profile of the pump and the two-photon momentum correlation profile for the cases of a collimated pump and a focused pump, respectively. In Fig. 5(b), a single superpixel for the signal photons is spatially correlated with multiple superpixels for the idler photons centered around the conjugate superpixel. In other words, after focusing, the increased angular spectrum of the pump beam substantially widens the two-photon correlation width. In Fig. 5(c) and (e), we depict the results for polarization state tomography for the case of the collimated pump. To illustrate the influence of the transverse momentum of the pump beam on the polarization entanglement of the down-converted photons, we map the concurrence and phase onto pixel coordinates of the joint momentum of signal and idler, which is essentially the transverse momentum of the pump beam $\boldsymbol{p}_\mathrm{p}$. Here, the polarization entanglement is found in a few superpixels within the narrower correlation profile, and ϕ displays little variation within the narrow angular spectrum of the collimated pump. In Fig. 5(d) and (f), we depict the results for polarization state tomography for the case of the focused pump. The concurrence map indicates the presence of polarization entanglement in all superpixels within the widened correlation profile, with an average concurrence of 0.6930 ± 0.0034. The decrease in concurrence upon focusing the pump likely results from lower count rates and higher statistical

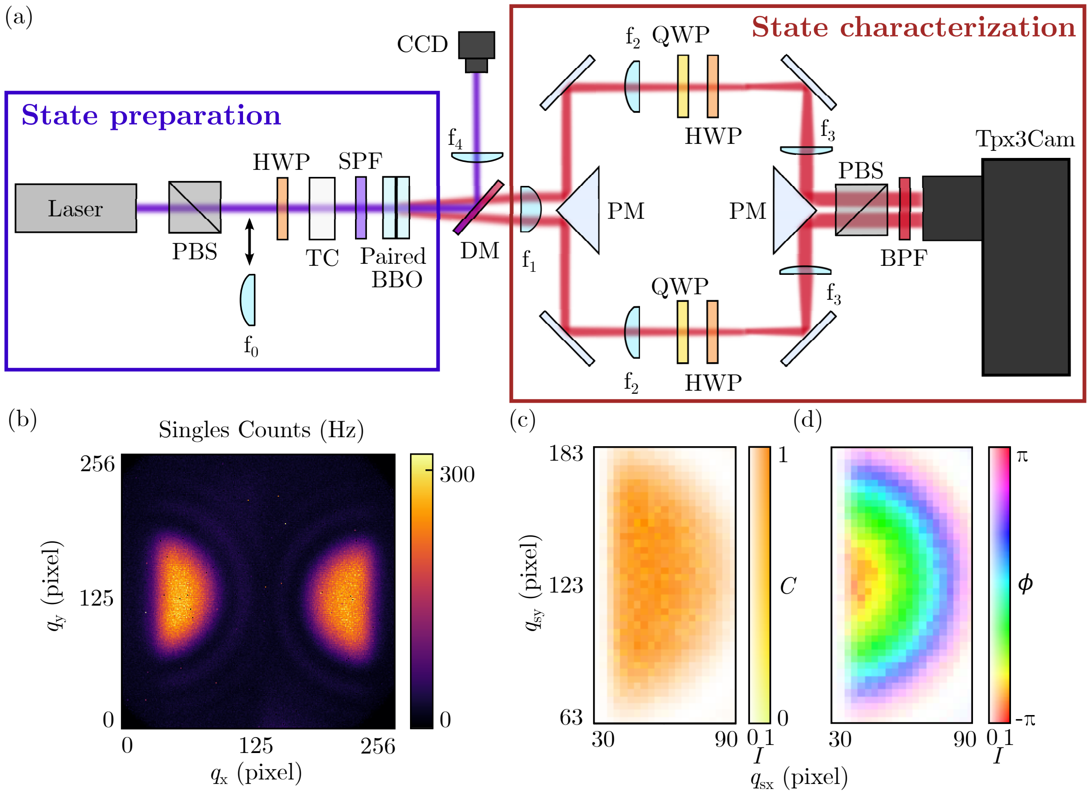

FIG. 4. (a) Schematic of the modified experimental setup. PM: prism mirror. Focal lengths of the lenses are f_0 = 100 mm, f_1 = 50 mm, f_2 = 100 mm f_3 = 150 mm and f_4 = 75 mm. The angular width of the pump beam is changed by inserting f_0 into the beam path. A CCD camera images the pump beam in the Fourier plane to analyze its angular width. (b) Far-field image of the SPDC field taken by the Tpx3Cam. (c) Concurrence and (d) relative phase of the two-photon states measured between momentum-correlated superpixels. Pixel coordinates correspond to the central position of the superpixels for signal photons.

fluctuations in individual pixels. In contrast to Fig. 5(e), the phase map illustrates a gradient of ϕ dependent on the transverse momentum of the pump beam, which is in good agreement with the theoretical predictions in Fig. 2(a) of [10]. To the best of our knowledge, this is the first direct measurement of the cross-influence between the spatial DoF of the pump beam and the polarization DoF of the down-converted photons. Our work opens up the opportunity to control the spatial structure of polarization states by jointly manipulating the polarization and spatial modes of the pump, which has implications in the study of topological structures of quantum light [4, 5, 41]. For instance, one can pump a paired crystal with a beam with spatially structured polarization and directly shape the correlation between spatial mode and polarization in the nonlocal optical skyrmions[6].

IV. CONCLUSION AND OUTLOOK

In this work, we image the spatially varying polarization entanglement in a two-photon state produced from SPDC using a data-driven camera capable of time-stamping single photons. In contrast to earlier studies that have imposed spatial-polarization structures by modulating a postselected subset of the full SPDC field, our work reveals those that are inherent to the SPDC process. By performing spatially-resolved polarization state tomography, we confirm the generation of an entire class of near-maximally polarization-entangled states with an average concurrence of 0.8303±0.0004 in the entire spatial profile of the SPDC field. Additionally, we certify an attainable entanglement dimensionality of 148 in the spatial DoF using the method discussed in Refs. [35, 36], which indicates a total attainable dimensionality of 251 in the joint spatial-polarization basis. We then present the experimentally characterized spatial-polarization structure. By producing the first complete spatial map of the polarization state generated from SPDC, we illustrate the dependence of polarization entanglement on the transverse momenta of the down-converted photons in the entire spatial profile of the SPDC field. Using a weakly focused pump beam, we, for the first time, experimentally characterize the cross-influence between the polarization DoF of the down-converted photons and the spatial DoF of the pump beam. Although the current Tpx3Cam system has a low overall photon detection efficiency of 8 % [26] and

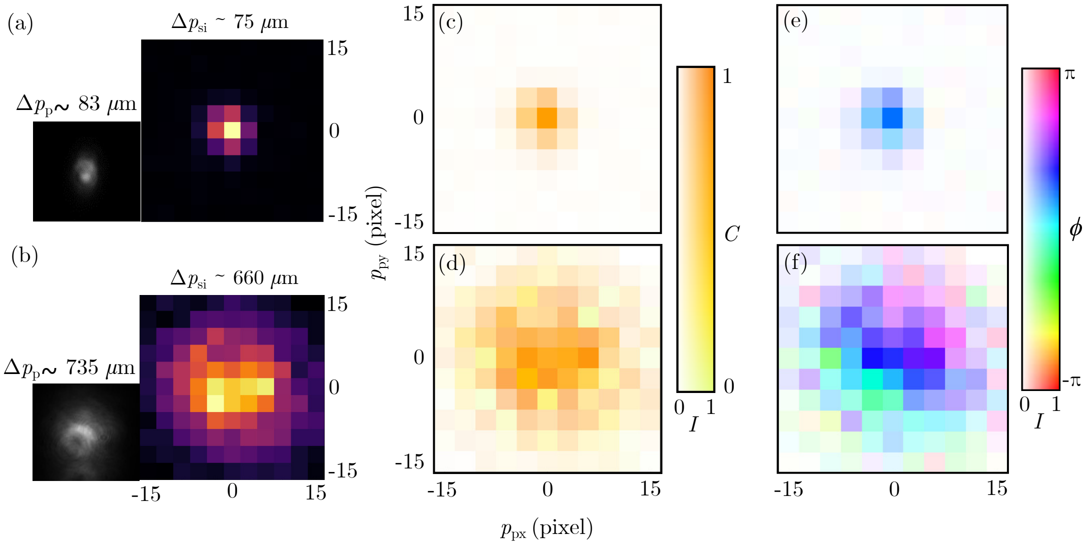

FIG. 5. Pump beam profile (greyscale image) and two-photon momentum correlation profile (colored image) for (a) collimated and (b) weakly focused pump beam. The inset captions state the beam width measured at the camera sensor plane. (c-d) Concurrence and (e-f) the two-photon polarization phase measured between a fixed signal superpixel and all momentum-correlated idler superpixels, where (c) and (e) correspond to collimated pumped beam while (d) and (f) correspond to weakly focused pump beam. Pixel coordinates indicate the transverse momenta of the pump beam $\boldsymbol{p}_{\rm p} = \boldsymbol{p}_s + \boldsymbol{p}_i$, in which the geometrical centers of two-photon momentum correlation profile are denoted $\boldsymbol{p}_{\rm px} = \boldsymbol{p}_{\rm py} = 0$

is thus not yet suited for studies involving Bell-type tests of nonlocality [42], its applicability could see further expansion by implementing an image intensifier with higher quantum efficiency and higher gain. For instance, a minimum detection efficiency of 2/3 is required to close the fair-sampling loophole in Bell tests [43].

Our results could be important for future work aimed at harnessing SPDC-based entanglement generation for high-dimensional quantum information processing applications [16, 44]. For instance, time-stamping single photons with a data-driven camera could significantly reduce the acquisition time requirements in polarization entanglement-enabled holography [7], potentially enabling fast super-resolution imaging and microscopy [45]. Our results on cross-influence between different DoFs could extend the recent demonstration of hiding images in quantum correlations [12] to hiding and rapidly reconstructing complex phase images in spatial and polarization correlations. On the fundamental side, our work can be extended to explore the spatial-polarization coupling in different entanglement generation schemes. For instance, it is possible to spatially resolve the polarization entanglement produced from post-selecting down-converted photons from a single Type-II nonlinear crystal [11, 46], thereby further deepening our understanding of the cross-DoF coupling in SPDC. Furthermore, our work could have important implications for studying and engineering hyperentangled photon states for various applications, such as noise-resilient quantum illumination [47], quantum key distribution with high secure key rates [48–50]. It may also be possible to build on existing work on exchange phases in Hong-Ou-Mandel interference involving high-dimensional hyperentangled photons [51] and spatially resolve such effects for a hyperentangled state.

ACKNOWLEDGMENTS

The authors thank X. Gao, A. D'Errico, B. Braverman, S. Karan, and M. Krenn for fruitful discussions. C. L. acknowledges P. Svihra for helpful advice on data processing. The portion of the work performed at the University of Ottawa was supported by the Canada Research Chairs program under Award 950-231657, the Natural Sciences and Engineering Research Council of Canada under Alliance Consortia Quantum Grant ALLRP 578468 - 22, Discovery Grant RGPIN/2017-06880, and the Canada First Research Excellence Fund Award 072623. In addition, R.W.B. acknowledges support through U.S. National Science Foundation Award No. 2138174 and U.S. Department of Energy Award No. FWP 76295.

Appendix A: Observation of spatial entanglement through the violation of Einstein-Podolsky-Rosen criteria

In Fig. 6, we depict the experimentally measured x- and y-components of the spatial correlation profile in both the position and momentum basis. We note the strong position correlations and momentum anti-correlations between the photons, which is a characteristic feature of spatial entanglement. Specifically, Fig. 6(c) and (f) depict the biphoton correlation profiles in the joint momentum and position coordinates of the down-converted photons. From these results, we conclude that in the Tpx3Cam sensor plane, individual discrete momentum and position modes are best approximated by 3×3-pixel large superpixels.

The results also allow us to quantitatively verify spatial entanglement by demonstrating violations of the Einstein-Podolsky-Rosen (EPR) criteria [52, 53]. We first obtain near-field (NF) and far-field (FF) correlation widths Δ_{NF} and Δ_{FF}, respectively, at the Tpx3Cam sensor plane by fitting Gaussians to the spatial correlation profiles of Fig. 6 in the x- and y-directions [30, 53, 54]. We then calculate the position and momentum uncertainties using the relations

$$\Delta(p_{ir}|p_{sr}) = \frac{k_{si}\hbar}{f_e}\Delta_{\mathrm{FF}}, \tag{A1a}$$

$$\Delta(q_{ir}|q_{sr}) = \frac{1}{M}\Delta_{\mathrm{NF}}, \tag{A1b}$$

where $p_{sr(ir)}$ and $q_{sr(ir)}$ stand for the momentum and position of the signal (idler) photons, respectively, $r = x, y$ represent the x- and y-components of the quantities, $k_{si} = (2\pi/810)\ \mathrm{nm}^{-1}$ is the wavevector of the signal and idler photons, $f_e = 75$ mm is the effective focal length of our far-field imaging system and $M = 2$ is the magnification of our near-field imaging system. We summarize our results in Table 1 and compute the conditional Heisenberg uncertainty products as

$$\Delta_{\min}p_x\Delta_{\min}q_x = (0.11 \pm 0.05)\hbar < \hbar/2, \tag{A2a}$$

$$\Delta_{\min}p_y\Delta_{\min}q_y = (0.12 \pm 0.03)\hbar < \hbar/2, \tag{A2b}$$

which clearly violates the EPR criteria in both the x- and y-directions. We note that the asymmetry observed in the x-components of the position correlation, which is depicted in Fig. 6(d), is likely a consequence of a distortion in the pump's intensity profile. As depicted in Fig. 1(c) in the main text, the near-field singles rates display a non-Gaussian spatial profile as a result of the distorted pump profile. Although this imperfection may affect the verification of spatial entanglement using the EPR criterion, which requires the pump beam to have a Gaussian profile [30], it does not refute our conclusions regarding the certification of hyperentanglement, as our entanglement certification protocol does not rely on Gaussian approximations of the SPDC field profiles [36].

TABLE I. Measurement uncertainties inferred from spatial correlation profiles

Quantity	Values	Units
$\Delta_{\min}p_x$	$(4.9 \pm 0.2) \times 10^{-3}$	$\hbar/\mu$m
$\Delta_{\min}p_y$	$(6.4 \pm 0.3) \times 10^{-3}$	$\hbar/\mu$m
$\Delta_{\min}q_x$	18.76 ± 9.49	μm
$\Delta_{\min}q_y$	18.18 ± 3.63	μm

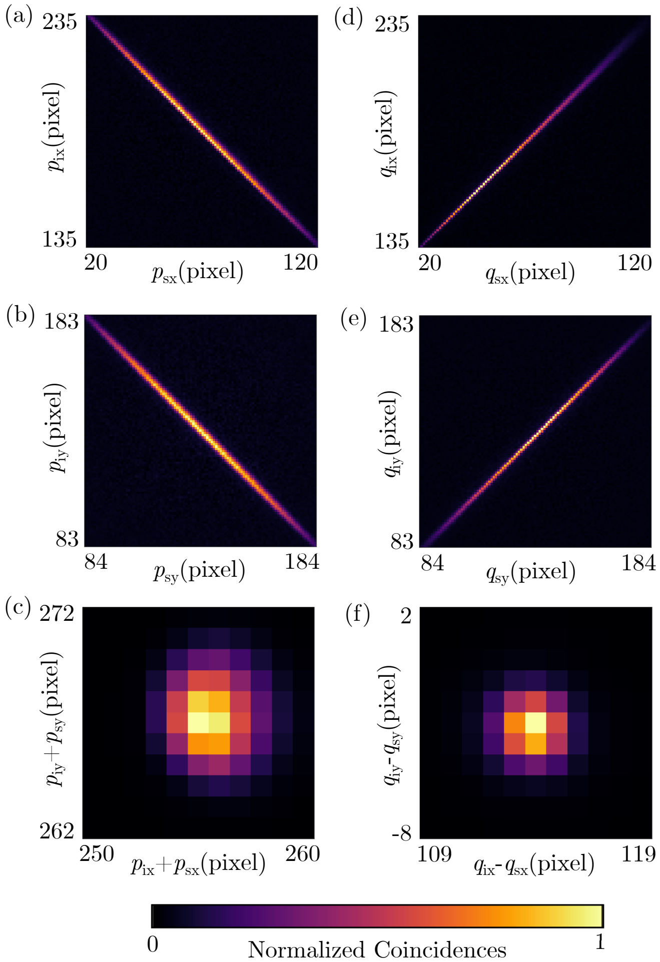

FIG. 6. Spatial correlation profiles measured in the x-components, y-components, and joint coordinates of the (a-c) momentum and (d-f) position of the signal-idler photons.

Appendix B: Estimation of fidelity lower bound

Following the approaches described in [37], we certify the dimensionality of entanglement in the spatial degree of freedom using correlations in two mutually unbiased bases (MUBs) [35, 36]. In the main text, we have defined the two MUBs to be the discrete momentum basis$\{|m\rangle_{s(i)}\}_{m\in[1,d]}$ and the discrete position basis $\{|u\rangle_{s(i)}\}_{u\in[1,d]}$.

The fidelity $F(\rho, \Psi)$ of the experimentally measured state ρ to a maximally entangled state $|\Psi\rangle = \sum_{m=1}^{d} \frac{1}{\sqrt{d}} |mm\rangle$ is defined as:

$$\begin{aligned} F(\rho,\Psi) &= \mathrm{Tr}\left(\left|\Psi\right\rangle\left\langle\Psi\right|\rho\right) \\ &= \sum_{m,n=1}^{d}\left\langle mm\right|\rho\left|nn\right\rangle \\ &= F_1(\rho,\Psi)+F_2(\rho,\Psi), \end{aligned} \tag{B1}$$

where

$$F_1(\rho,\Psi)=\frac{1}{d}\sum_{m=1}^{d}\left\langle mm\right|\rho\left|mm\right\rangle, \tag{B2}$$

$$F_2(\rho,\Psi)=\frac{1}{d}\sum_{m\neq n}\left\langle mm\right|\rho\left|nn\right\rangle. \tag{B3}$$

Since for an arbitrary state ρ with a Schmidt number of $k \leq d$, the fidelity satisfies

$$F(\rho,\Psi)\leq B_k(\Psi)=\frac{k}{d}, \tag{B4}$$

the entanglement dimensionality of a state with $F(\rho,\Psi) > B_k(\Psi)$ must be at least $k+1$. As we will show in the following, correlations in the two MUBs will allow us to obtain a lower bound for the fidelity via $\tilde{F}(\rho,\Psi) = F_1(\rho,\Psi)+\tilde{F}_2(\rho,\Psi) \leq F_1(\rho,\Psi)+F_2(\rho,\Psi) = F(\rho,\Psi)$

The coincidence counts N_{mn} measured in the discrete momentum basis allow us to calculate $F_1(\rho,\Psi)$ using

$$\left\langle mn\right|\rho\left|mn\right\rangle=\frac{N_{mn}}{\sum_{k,l}N_{kl}}. \tag{B5}$$

Supplementing the coincidence counts N_{uv} measured in the discrete position basis allows us to calculate $\tilde{F}_2(\rho,\Psi)$, the lower bound of $F_2(\rho,\Psi)$, via

$$\tilde{F}_2(\rho,\Psi)=\sum_{u=0}^{d-1}\langle uu|\rho|uu\rangle-\frac{1}{d}-\sum_{m\neq n',m\neq n,n\neq n',n'\neq m'}\gamma_{mnm'n'}\sqrt{\langle mn|\rho|mn\rangle\langle m'n'|\rho|m'n'\rangle}, \tag{B6}$$

where

$$\left\langle uv\right|\rho\left|uv\right\rangle=\frac{N_{uv}}{\sum_{k,l}N_{kl}}, \tag{B7}$$

$$\gamma_{mm'nn'}=\begin{cases}0 & \text{if } (m-m'-n+n') \bmod d\neq 0\\ 1/d & \text{otherwise.}\end{cases} \tag{B8}$$

[1] S. E. Harris, M. K. Oshman, and R. L. Byer, Observation of tunable optical parametric fluorescence, Phys. Rev. Lett. **18**, 732 (1967).

[2] D. C. Burnham and D. L. Weinberg, Observation of simultaneity in parametric production of optical photon pairs, Physical Review Letters **25**, 84 (1970), publisher: American Physical Society.

[3] Y. H. Shih and C. O. Alley, New type of Einstein-Podolsky-Rosen-Bohm experiment using pairs of light quanta produced by optical parametric down conversion, Phys. Rev. Lett. **61**, 2921 (1988).

[4] C. He, Y. Shen, and A. Forbes, Towards higher-dimensional structured light, Light: Science & Applications **11**, 205 (2022), number: 1 Publisher: Nature Publishing Group.

[5] I. Nape, B. Sephton, P. Ornelas, C. Moodley, and A. Forbes, Quantum structured light in high dimensions, APL Photonics **8**, 051101 (2023).

[6] P. Ornelas, I. Nape, R. de Mello Koch, and A. Forbes, Non-local skyrmions as topologically resilient quantum entangled states of light, Nature Photonics **18**, 258 (2024).

[7] H. Defienne, B. Ndagano, A. Lyons, and D. Faccio, Polarization entanglement-enabled quantum holography, Nature Physics **17**, 591 (2021), number: 5 Publisher: Nature Publishing Group.

[8] G. Vallone, G. Donati, R. Ceccarelli, and P. Mataloni, Six-qubit two-photon hyperentangled cluster states: Characterization and application to quantum computation, Phys. Rev. A **81**, 052301 (2010).

[9] M. Ciampini, A. Orieux, S. Paesani, *et al.*, Path-polarization hyperentangled and cluster states of photons on a chip, Light: Science & Applications **5**, e16064 (2016).

[10] C. Li, B. Braverman, G. Kulkarni, and R. W. Boyd, Experimental generation of polarization entanglement from spontaneous parametric down-conversion pumped by spatiotemporally highly incoherent light, Physical

Review A **107**, L041701 (2023), publisher: American Physical Society.

[11] W. Zhang, D. Xu, and L. Chen, Polarization entanglement from parametric down-conversion with an LED pump, Physical Review Applied **19**, 054079 (2023), publisher: American Physical Society.

[12] C. Vernière and H. Defienne, Hiding images in quantum correlations, Phys. Rev. Lett. **133**, 093601 (2024).

[13] P. G. Kwiat, E. Waks, A. G. White, I. Appelbaum, and P. H. Eberhard, Ultrabright source of polarization-entangled photons, Physical Review A **60**, R773 (1999), publisher: American Physical Society.

[14] J. T. Barreiro, N. K. Langford, N. A. Peters, and P. G. Kwiat, Generation of hyperentangled photon pairs, Physical Review Letters **95**, 260501 (2005), publisher: American Physical Society.

[15] D. F. V. James, P. G. Kwiat, W. J. Munro, and A. G. White, Measurement of qubits, Physical Review A **64**, 052312 (2001), publisher: American Physical Society.

[16] N. Friis, G. Vitagliano, M. Malik, and M. Huber, Entanglement certification from theory to experiment, Nature Reviews Physics **1**, 72 (2019), number: 1 Publisher: Nature Publishing Group.

[17] N. Herrera Valencia, V. Srivastav, M. Pivoluska, M. Huber, N. Friis, W. McCutcheon, and M. Malik, High-Dimensional Pixel Entanglement: Efficient Generation and Certification, Quantum **4**, 376 (2020).

[18] M. Fisher-Levine and A. Nomerotski, Timepixcam: a fast optical imager with time-stamping, Journal of Instrumentation **11** (03), C03016.

[19] A. Nomerotski, Imaging and time stamping of photons with nanosecond resolution in timepix based optical cameras, Nuclear Instruments and Methods in Physics Research Section A: Accelerators, Spectrometers, Detectors and Associated Equipment **937**, 26 (2019).

[20] A. Nomerotski, M. Chekhlov, D. Dolzhenko, R. Glazenborg, B. Farella, M. Keach, R. Mahon, D. Orlov, and P. Svihra, Intensified tpx3cam, a fast data-driven optical camera with nanosecond timing resolution for single photon detection in quantum applications, Journal of Instrumentation **18** (01), C01023.

[21] C. Ianzano, P. Svihra, M. Flament, A. Hardy, G. Cui, A. Nomerotski, and E. Figueroa, Fast camera spatial characterization of photonic polarization entanglement, Scientific Reports **10**, 6181 (2020), number: 1 Publisher: Nature Publishing Group.

[22] B. Courme, C. Vernière, P. Svihra, S. Gigan, A. Nomerotski, and H. Defienne, Quantifying high-dimensional spatial entanglement with a single-photon-sensitive time-stamping camera, Optics Letters **48**, 3439 (2023), publisher: Optica Publishing Group.

[23] X. Gao, Y. Zhang, A. D'Errico, A. Sit, K. Heshami, and E. Karimi, Full spatial characterization of entangled structured photons, Phys. Rev. Lett. **132**, 063802 (2024).

[24] Y. Nambu, K. Usami, Y. Tsuda, K. Matsumoto, and K. Nakamura, Generation of polarization-entangled photon pairs in a cascade of two type-i crystals pumped by femtosecond pulses, Physical Review A **66**, 033816 (2002), publisher: American Physical Society.

[25] J. B. Altepeter, E. R. Jeffrey, and P. G. Kwiat, Phase-compensated ultra-bright source of entangled photons, Optics Express **13**, 8951 (2005), publisher: Optica Publishing Group.

[26] V. Vidyapin, Y. Zhang, D. England, and B. Sussman, Characterisation of a single photon event camera for quantum imaging, Scientific Reports **13**, 1009 (2023).

[27] Y. Zhang, D. England, A. Nomerotski, P. Svihra, S. Ferrante, P. Hockett, and B. Sussman, Multidimensional quantum-enhanced target detection via spectrotemporal-correlation measurements, Phys. Rev. A **101**, 053808 (2020).

[28] W. K. Wootters, Entanglement of formation of an arbitrary state of two qubits, Physical Review Letters **80**, 2245 (1998), publisher: American Physical Society.

[29] P. G. Kwiat, Hyper-entangled states, Journal of Modern Optics **44**, 2173 (1997).

[30] C. K. Law and J. H. Eberly, Analysis and interpretation of high transverse entanglement in optical parametric down conversion, Physical Review Letters **92**, 127903 (2004), publisher: American Physical Society.

[31] H. Di Lorenzo Pires, C. H. Monken, and M. P. van Exter, Direct measurement of transverse-mode entanglement in two-photon states, Phys. Rev. A **80**, 022307 (2009).

[32] M. P. Edgar, D. S. Tasca, F. Izdebski, R. E. Warburton, J. Leach, M. Agnew, G. S. Buller, R. W. Boyd, and M. J. Padgett, Imaging high-dimensional spatial entanglement with a camera, Nature Communications **3**, 984 (2012), number: 1 Publisher: Nature Publishing Group.

[33] F. Devaux, A. Mosset, P.-A. Moreau, and E. Lantz, Imaging spatiotemporal hong-ou-mandel interference of biphoton states of extremely high schmidt number, Phys. Rev. X **10**, 031031 (2020).

[34] X. Gao, Y. Zhang, A. D'Errico, K. Heshami, and E. Karimi, High-speed imaging of spatiotemporal correlations in hong-ou-mandel interference, Opt. Express **30**, 19456 (2022).

[35] J. Bavaresco, N. Herrera Valencia, C. Klöckl, M. Pivoluska, P. Erker, N. Friis, M. Malik, and M. Huber, Measurements in two bases are sufficient for certifying high-dimensional entanglement, Nature Physics **14**, 1032 (2018), number: 10 Publisher: Nature Publishing Group.

[36] P. Erker, M. Krenn, and M. Huber, Quantifying high dimensional entanglement with two mutually unbiased bases, Quantum **1**, 22 (2017), publisher: Verein zur Förderung des Open Access Publizierens in den Quantenwissenschaften.

[37] B. Ndagano, H. Defienne, A. Lyons, I. Starshynov, F. Villa, S. Tisa, and D. Faccio, Imaging and certifying high-dimensional entanglement with a single-photon avalanche diode camera, npj Quantum Information **6**, 1 (2020), number: 1 Publisher: Nature Publishing Group.

[38] M. A. Nielsen and I. L. Chuang, *Quantum Computation and Quantum Information: 10th Anniversary Edition* (Cambridge University Press, 2010).

[39] W. K. Wootters, Entanglement of formation and concurrence, Quantum Info. Comput. **1**, 27–44 (2001).

[40] L. Scarfe, R. Abolhassani, F. Bouchard, A. Z. Goldberg, K. Heshami, F. Di Colandrea, and E. Karimi, High-dimensional quantum key distribution with qubit-like states, Communications Physics **8**, 472 (2025).

[41] Y. Shen, Q. Zhang, P. Shi, L. Du, X. Yuan, and A. V. Zayats, Optical skyrmions and other topological quasiparticles of light, Nature Photonics **18**, 15 (2024).

[42] C. K. Zeitler, J. C. Chapman, E. Chitambar, and P. G. Kwiat, Entanglement verification of hyperentangled photon pairs, Phys. Rev. Appl. **18**, 054025 (2022).

[43] N. Gisin and B. Gisin, A local hidden variable model of quantum correlation exploiting the detection loophole, Physics Letters A **260**, 323 (1999).

[44] M. Erhard, M. Krenn, and A. Zeilinger, Advances in high-dimensional quantum entanglement, Nature Reviews Physics **2**, 365 (2020), number: 7 Publisher: Nature Publishing Group.

[45] H. Defienne, P. Cameron, B. Ndagano, A. Lyons, M. Reichert, J. Zhao, A. R. Harvey, E. Charbon, J. W. Fleischer, and D. Faccio, Pixel super-resolution with spatially entangled photons, Nature Communications **13**, 3566 (2022).

[46] C. E. Kuklewicz, M. Fiorentino, G. Messin, F. N. C. Wong, and J. H. Shapiro, High-flux source of polarization-entangled photons from a periodically poled ktiopo$_4$ parametric down-converter, Phys. Rev. A **69**, 013807 (2004).

[47] A. V. Prabhu, B. Suri, and C. M. Chandrashekar, Hyperentanglement-enhanced quantum illumination, Phys. Rev. A **103**, 052608 (2021).

[48] F. Wu, G. Yang, H. Wang, J. Xiong, F. Alzahrani, A. Hobiny, and F. Deng, High-capacity quantum secure direct communication with two-photon six-qubit hyperentangled states, Science China Physics, Mechanics & Astronomy **60**, 120313 (2017).

[49] J.-H. Kim, Y. Kim, D.-G. Im, C.-H. Lee, J.-W. Chae, G. Scarcelli, and Y.-H. Kim, Noise-resistant quantum communications using hyperentanglement, Optica **8**, 1524 (2021).

[50] L. Nemirovsky-Levy, U. Pereg, and M. Segev, Increasing quantum communication rates using hyperentangled photonic states, Optica Quantum **2**, 165 (2024).

[51] Z.-F. Liu, C. Chen, J.-M. Xu, Z.-M. Cheng, Z.-C. Ren, B.-W. Dong, Y.-C. Lou, Y.-X. Yang, S.-T. Xue, Z.-H. Liu, W.-Z. Zhu, X.-L. Wang, and H.-T. Wang, Hong-ou-mandel interference between two hyperentangled photons enables observation of symmetric and antisymmetric particle exchange phases, Phys. Rev. Lett. **129**, 263602 (2022).

[52] M. D. Reid, Demonstration of the einstein-podolsky-rosen paradox using nondegenerate parametric amplification, Physical Review A **40**, 913 (1989), publisher: American Physical Society.

[53] A. Bhattacharjee, N. Meher, and A. K. Jha, Measurement of two-photon position–momentum einstein–podolsky–rosen correlations through single-photon intensity measurements, New Journal of Physics **24**, 053033 (2022).

[54] C. H. Monken, P. H. S. Ribeiro, and S. Pádua, Transfer of angular spectrum and image formation in spontaneous parametric down-conversion, Physical Review A **57**, 3123 (1998), publisher: American Physical Society.

Chapter 4

Violation of local realism with spatially multimode parametric down-conversion pumped by spatially incoherent light

Having experimentally characterized the spatially varying polarization entanglement generated by SPDC, I concluded that the pump's spatial components influence the polarization entanglement of the down-converted photons in a deterministic manner. In other words, it can be compensated for by optimizing the experimental setup. Consequently, I proposed that, by adopting a Sagnac-type polarization-entanglement source that automatically compensates for most spatiotemporal walk-offs, SPDC pumped by spatially incoherent light can produce highly polarization-entangled two-photon states. The significantly enhanced polarization entanglement manifests as a capability to violate local realism, which the results in Chapter 2 cannot demonstrate.

I built the experimental setup shown in Fig. 1, which had been optimized over several iterations through helpful discussions with Dr. Jeremy Upham and Dr. Boris Braverman. I performed measurements and developed Python-based data-processing programs that produced the results shown in Fig. 2-4. I analyzed the data through discussions with Dr. Jeremy Upham and Dr. Boris Braverman. I wrote the first draft of the manuscript, which had undergone several rounds of revisions with contributions from all co-authors. Prof. Robert Boyd supervised the research.

My presentation of this work at the Photonics North 2025 conference has been awarded the 1st place conference paper by the IEEE Photonics Society Ottawa Chapter. This work has been published in Physical Review A.

PHYSICAL REVIEW A **112**, 053726 (2025)

Violation of local realism with spatially multimode parametric down-conversion pumped by spatially incoherent light

Cheng Li,[1,*] Jeremy Upham,[1] Boris Braverman,[2] and Robert W. Boyd[1,3,†]
[1]*Department of Physics, University of Ottawa, Ottawa, Ontario, Canada K1N 6N5*
[2]*Department of Physics, University of Toronto, Toronto, Ontario, Canada M5S 1A7*
[3]*Institute of Optics, University of Rochester, Rochester, New York 14627, USA*

(Received 9 July 2025; accepted 10 November 2025; published 25 November 2025)

We experimentally demonstrate a violation of local realism with highly spatially multimode polarization-entangled two-photon states produced by spontaneous parametric down-conversion (SPDC) pumped by a spatially incoherent light source—a light-emitting diode (LED). While existing studies have observed such a violation only by postselecting the LED-pumped SPDC photons into a single spatial detection mode, we achieve a Clauser-Horne-Shimony-Holt inequality violation of $S = 2.532 \pm 0.069 > 2$ using a spatially multimode detection setup that collects nearly 4080 SPDC spatial modes. These results indicate that coherent pump sources, such as lasers, are not required for SPDC-based entanglement generation. Our work could enable novel and practical sources of entangled photons for quantum technologies such as device-independent quantum key distribution and quantum-enhanced sensing.

DOI: 10.1103/mxxf-ycdf

I. INTRODUCTION

Entangled quantum systems can violate local realism and exhibit correlations that local hidden variable theories cannot fully explain [1–3]. This feature is arguably a key distinction between classical and quantum systems. In many practical quantum applications, the violation of local realism benchmarks the performance of quantum systems over their classical counterparts. For instance, observing nonlocal correlations between quantum systems certifies the security of a quantum communication channel [4–6]. Recent studies have also shown that violation of local realism is a valuable resource for quantum-enhanced imaging and metrology [7–9]. Entangled photons produced from spontaneous parametric down-conversion (SPDC) [10–12] are excellent candidates for demonstrating such violation [13–15] and enabling practical quantum applications [16–20]. Coherent light beams, such as those emitted from lasers, have been almost universally employed to pump SPDC and are generally presumed to be indispensable for SPDC-based entanglement generation. Specifically, it has been shown that without postselection, the pump's coherence in a given degree of freedom sets an upper bound on the attainable two-photon entanglement in the *same* degree of freedom [21–30]. Recent studies have found that this requirement on the pump's coherence in a given degree of freedom does not necessarily apply to two-photon entanglement in a *different* degree of freedom [31], thus making incoherent light sources such as light-emitting diodes (LEDs) and sunlight possible alternatives to a laser pump. For instance, SPDC pumped by an LED, which is a spatiotemporally incoherent light source, has been shown to produce polarization-entangled photons if the LED light is polarization filtered [32,33].

However, unlike polarization-entangled photons produced from lasers, those produced from LEDs have not previously been shown to lead to a violation of local realism unless the down-converted photons were first postselected to reside in a narrow spatial bandwidth using single-mode fibers (SMFs) [32,33]. Conducting single-spatial-mode postselection on down-converted photons and detecting them in coincidence effectively projects the pump light into a single spatial mode, thereby defeating the purpose of using a spatially incoherent pump, which contains multiple spatial modes. On the other hand, rejecting photons in higher-order spatial modes effectively reduces detection efficiency and creates a security loophole in quantum communication systems that utilize such devices. We argue that the spatial coherence of the pump beam does not fundamentally limit the attainable polarization entanglement, and the reduced entanglement is a consequence of technical limitations such as uncompensated walk-offs within the nonlinear crystal that couple the spatial and polarization degrees of freedom [34–36]. In particular, the single-pass, double-crystal setup [37] employed in Ref. [32] introduces a transverse-momentum-dependent phase between orthogonal polarization components of the pump beam [38]. Since spatially incoherent light typically has a larger angular bandwidth than spatially coherent light, this phase variation reduces the effective degree of polarization of the pump beam, which limits the maximally attainable two-photon polarization entanglement [29]. On the other hand, the single-pass, single-crystal setup adapted by Zhang *et al.* [33,36] introduces a transverse-momentum-dependent phase between orthogonal polarization components of the down-converted photons, which increases their path distinguishability and results in a

---

[*] Contact author: cli221@uottawa.ca

[†] Contact author: rboyd@uottawa.ca

lower entanglement unless one performs single-spatial-mode postselection.

Here, we report a violation of local realism with a highly spatially multimode two-photon polarization-entangled state produced from SPDC pumped by the spatially incoherent light beam emitted from an LED. We place the nonlinear crystal inside a polarization Sagnac interferometer (PSI) [39]. The high degree of symmetry between the counterpropagating directions in the PSI setup can significantly mitigate for temporal and spatial walk-offs that the pump and down-converted photons experience within the crystal. We avoid postselection into a single spatial mode by coupling the down-converted photons into multimode fibers (MMFs) that can collect approximately 4080 spatial modes of the down-converted photons produced from LED-pumped SPDC. We detect a two-photon state that displays a Clauser-Horne-Shimony-Holt (CHSH) inequality violation of $S = 2.532 \pm 0.069 > 2$ [3]. We quantify the produced two-photon polarization entanglement by conducting quantum state tomography [40], from which we find a concurrence of $C = 0.834 \pm 0.038$ [41]. These results present direct evidence that the coherence of the pump beam in a given degree of freedom does not fundamentally limit the attainable entanglement in a different degree of freedom. In other words, strong entanglement can be produced from incoherent light sources with technical improvements on the setup design. This opens an avenue for developing novel quantum light sources for practical applications. As a comparison, the same setup pumped by a spatially coherent light beam emitted from a laser yields a CHSH-inequality violation of $S = 2.695 \pm 0.006$ and a concurrence of $C = 0.952 \pm 0.002$. The remaining differences between the CHSH-inequality violation and polarization entanglement produced from LED- and laser-pumped SPDC are likely due to wave-front distortions introduced by imperfect optical components.

II. EXPERIMENTAL SETUP

Figure 1 depicts the experimental setup. An LED (Thorlabs M405L3) emits a spatially incoherent pump field with a center wavelength of 405 nm. This light field is first butt-coupled into an MMF with a core diameter of 50 μm and numerical aperture (NA) of 0.22 (MMF-50-0.22), and subsequently collimated into a beam using a microscope objective with 20× magnification and 0.4 NA. We select the MMF parameters to match the size of the LED pump beam and the transverse dimensions of the nonlinear medium in the same plane, thereby maximizing the interaction region between the pump light and the nonlinear medium. For benchmarking the performance of the setup and comparing the results from pump sources with different coherence properties, a spatially coherent pump beam from an SMF-coupled laser with a center wavelength of 405 nm and a bandwidth of 0.01 nm (Integrated Optics 0405L-23A-NI-AT-NF) is coaligned with the LED beam into the setup. Using a combination of a polarizing beam splitter (PBS), a half-wave plate (HWP) and a quarter-wave plate (QWP), we can make both pump beams perfectly polarized with arbitrary polarizations, which allows us to maximize the attainable polarization entanglement and generate arbitrary two-photon polarization states residing in the $\{|HV\rangle, |VH\rangle\}$ subspace. To characterize LED- and laser-pumped SPDC, we can turn on only the LED or laser and adjust their polarizations to be the same. The pump beam is spectrally filtered using a bandpass filter with a center wavelength of 405 nm and a bandwidth of 1.5 nm (BPF-405) and focused into the nonlinear medium using a lens with a focal length of $f_1 = 200$ mm. After the spectral filtering, the LED beam retains a power of ∼1.2 μW while the laser beam has a power of ∼1.5 mW. At the center of the nonlinear medium, the LED pump beam has a diameter of ∼1 mm while the laser pump beam has a diameter of ∼100 μm. The estimated divergence half-angles for the LED and the laser pump beam are 11 mrad and 2.6 mrad, respectively.

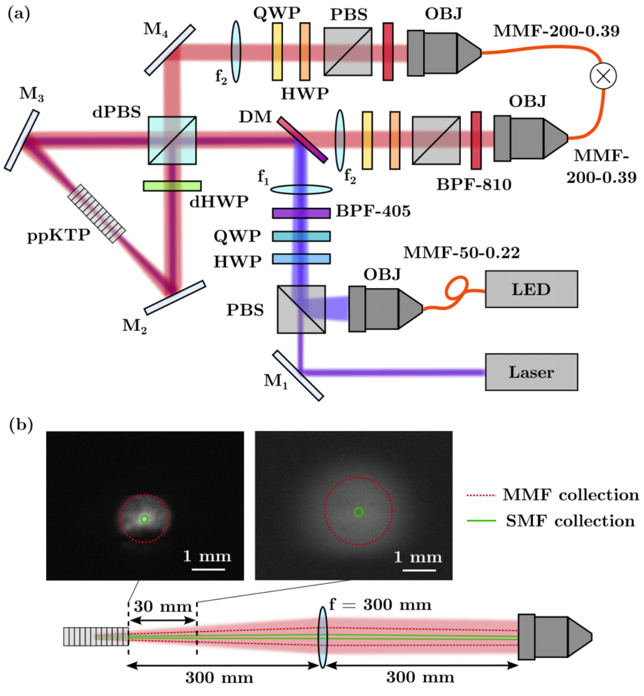

FIG. 1. (a) Schematic of the experimental setup. The SPDC processes for generating polarization-entangled photons occur in the ppKTP crystal, which is placed inside the PSI. M_{1-4}: silver mirrors; PBS: polarizing beam splitter; HWP: half-wave plate; dPBS and dHWP: dual-wavelength PBS and HWP; DM: dichroic mirror; ppKTP: periodically poled potassium titanyl phosphate; QWP: quarter-wave plate; BPF-810(405): band-pass filter centered at 810(405) nm with a bandwidth of 10(1.5) nm; MMF-200-0.39(50-0.22): multimode fiber with a core diameter of 200(50) μm and an NA of 0.39(0.22); OBJ: microscope objective with 20× magnification and 0.4 NA. (b) Schematic of the procedure for measuring the number of generated and detected spatial modes (not to scale). Inset images show the multimode-laser-pumped SPDC field intensity at z = 0 mm and 30 mm from the ppKTP crystal output face compared to the effective collection aperture using MMFs (dashed red circles). The solid green circles show the collection aperture of SMFs for comparison.

The nonlinear medium is a 10-mm-long, 2-mm-wide, 1-mm-thick periodically poled potassium titanyl phosphate (ppKTP) crystal with a grating period of 10 μm. It is quasi-phase-matched for Type-II collinear frequency-degenerate SPDC from 405 to 810 nm at 50 °C. We place this crystal inside a PSI comprised of a dual-wavelength PBS (dPBS, Newlight

PBS0025-405/810), a dual-wavelength HWP (dHWP, Newlight WPD03-H810-H405), and two silver mirrors. If pump beams propagating in clockwise and counterclockwise directions induce two SPDC processes that are indistinguishable by the detectors, the setup produces a polarization-entangled two-photon state

$$|\Psi\rangle = \frac{1}{\sqrt{2}}(|HV\rangle + e^{i\phi}|VH\rangle), \tag{1}$$

where ϕ is the two-photon polarization phase jointly determined by the initial polarization of the pump beam, the phase acquired passing through the dHWP, and the wave-front distortion of the dPBS [39].

The SPDC field is emitted into two distinct paths and collimated by a lens with a focal length of $f_2 = 300$ mm in each. We denote the down-converted photons emitted into the upper path in Fig. 1 as *signal* while those emitted into the lower path as *idler*. Their joint polarization state is analyzed using a set of QWP, HWP, and PBS in each path. Note that we have chosen all wave plates in the setup to be zero order (except for the dHWP inside the PSI) and have carefully aligned their optical axes before taking measurements. We use microscope objectives (OBJs) to couple down-converted photons into MMFs with core diameters of 200 μm and NAs of 0.39 (MMF-200-0.39), which support more than 45 000 spatial modes, and we detect them using avalanche photodiodes (PerkinElmer SPCM-QRH-14-FC).

Since our photon-collection setup has finite optical apertures, we use the scheme as depicted in Fig. 1(b) to estimate the number of spatial modes collected into the MMFs. To simulate the propagation parameters of LED-pumped SPDC, we couple the laser into the same MMF used for coupling the LED (MMF-50-0.22) and use the output beam from this MMF to pump the crystal. We acquire near-field images of the SPDC at two planes along its propagation path (indicated by vertical dashed lines), one at the output surface of the crystal and the other at 30 mm from the crystal plane. The acquired images are displayed as insets to Fig. 1(b). By fitting a Gaussian curve to the measured beam profiles, we estimate that LED-pumped SPDC has a diameter of $D_{\text{SPDC}}^{\text{crystal}} = 1.66$ mm and divergence half-angle of $\theta_{\text{SPDC}}^{\text{crystal}} = 45$ mrad at the crystal plane. After propagating through the lens $f_2 = 300$ mm, the SPDC profile has an estimated diameter of $D_{\text{SPDC}}^{\text{OBJ}} = 27.03$ mm and divergence half-angle of $\theta_{\text{SPDC}}^{\text{OBJ}} = 2.75$ mrad at the OBJ input plane. We estimate the mode field diameter accepted by MMF-200-0.39 at the input plane of OBJ from the numerical aperture of the MMF, which is 0.39, and the effective focal length (f_e) of the OBJ we used, which is 10 mm, to be $D_{\text{MMF}}^{\text{OBJ}} = 2f_e \tan(\arcsin(\text{NA})) = 8.47$ mm, and the corresponding divergence half-angle is $\theta_{\text{MMF}}^{\text{OBJ}} = 10$ mrad. We note that $D_{\text{MMF}}^{\text{OBJ}}$ is smaller than the diameter of the input aperture of the OBJ, which is 10 mm. Since the MMFs accept a larger divergence half-angle than the SPDC field has at the OBJ input plane, we estimate the number of spatial modes of SPDC light collected by each MMF to be $M = (\pi D\theta/\lambda)^2/2 = 4080$, which indicates that the collected two-photon states are highly spatially multimode. Although the sensor areas of the avalanche diodes (180 μm) are smaller than the core diameters of the MMFs, we expect to detect all collected spatial modes with approximately the same efficiency because they have undergone mode mixing in the 1-m-long, step-index MMFs. Therefore, our photon-collection setup detects highly spatially multimode SPDC emission in which the signal-idler correlations truly reflect the influence of the spatially incoherent pump. In contrast, the mode field diameter accepted by SMFs at the input plane of OBJ is approximately 2.62 mm and the corresponding half-angle is approximately 0.39 mrad, both of which are much smaller than those of the MMFs. For comparison, we depict in Fig. 1(b) the mode field collected by MMFs (dashed red lines) and SMFs (solid green lines).

We extract the photon coincidence rates using a Universal Quantum Devices Logic-16 data-acquisition unit with a coincidence time resolution window $\tau = 1$ ns. To test for violation of local realism using the CHSH criterion $S \leqslant 2$ [3], we measure the polarization correlation between signal and idler photons by fixing the polarization projection in the signal path while recording the coincidence rates as a function of different linear polarization projections of the idler arm. To characterize the resulting two-photon polarization state, we perform quantum state tomography by recording coincidence rates at 16 different polarization projection bases and reconstruct the two-photon density matrix ρ, from which we can infer the two-photon polarization phase ϕ and quantify the entanglement by calculating the concurrence $C(\rho)$ [41]. For LED-pumped SPDC, we set an acquisition time of 5 min for each projective measurement and observe a maximum coincidence rate of $\sim$100 min^{-1} with an accidental coincidence rate of $\sim$0.006 min^{-1}; for laser-pumped SPDC, we set the acquisition time for each projective measurement at 10 s and observe a maximum coincidence rate of $\sim$11 300 s^{-1} with an accidental coincidence rate of $\sim$50 s^{-1}. The accidental coincidence rates are estimated using $2S_sS_i\tau$, where $S_{s(i)}$ is the singles rate in the signal(idler) arm. The average singles rates are $\sim$220 s^{-1} and $\sim$155 000 s^{-1} for LED- and laser-pumped SPDC, respectively. We repeat each measurement ten times to estimate the average value and standard deviation and subtract accidental coincidence rates from the raw data prior to data analysis. The coincidence rate of LED-pumped SPDC is lower than that of the laser-pumped SPDC for two main reasons: (i) the input power of the LED pump is approximately 10^{-3} lower than that of the laser pump; (ii) we estimate the type-II ppKTP crystal to have a narrow phase-matching bandwidth of $\sim$0.3 nm and could only interact with a fraction of the power within the LED pump's 1.5-nm bandwidth to induce SPDC.

III. RESULTS AND DISCUSSIONS

Figure 2 shows the experimentally measured polarization correlation fringes of LED- and laser-pumped SPDC. We denote $\theta_{s(i)}$ as the angle between the horizontal polarization and the linear polarization bases into which the signal(idler) photons are projected. We then adjust the pump polarization to set $\phi = \pm\pi$ in Eq. (1), thereby targeting $|\psi\rangle = (|HV\rangle - |VH\rangle)/\sqrt{2}$, and measure the coincidence rates as a function of θ_i with the signal photons projected into four different bases. Specifically, we choose to project signal photons into the horizontal (H), vertical (V), antidiagonal (A), and diagonal (D) bases by setting $\theta_s = 0^\circ, 90^\circ, 135^\circ,$ and 45°, respectively.

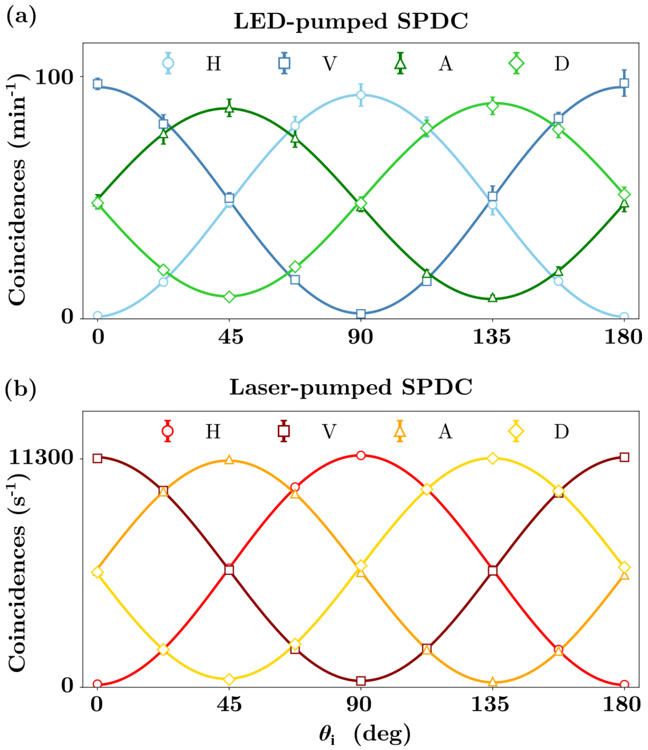

FIG. 2. Polarization correlation fringes of (a) LED-pumped SPDC and (b) laser-pumped SPDC measured by projecting the signal and idler photons into different linear polarization bases represented by angles $\theta_{s(i)}$ with the horizontal polarization. Specifically, we denote the cases of $\theta_s = 0^\circ, 45^\circ, 90^\circ, 135^\circ$ as measurements in the horizontal (H), diagonal (D), vertical (V), and antidiagonal (A) bases, respectively. The markers represent the experimentally measured coincidence rates in H (circles), V (squares), A (triangles), and D (diamonds) bases. The solid lines represent the sinusoidal fitting of the experimental data. The error bars in (b) are indiscernible since they are much smaller than the markers' sizes.

The fringe visibility is defined as $(N_{\max} - N_{\min})/(N_{\max} + N_{\min})$, where $N_{\max(\min)}$ represents the maximal(minimal) coincidence rate measured in each basis. As a result, the LED-pumped SPDC exhibits fringe visibilities of $98.07\% \pm 0.70\%$, $95.85\% \pm 0.78\%$, $81.45\% \pm 1.88\%$, and $81.31\% \pm 2.89\%$ in the H, V, A, and D bases, respectively. The high fringe visibility in the two mutually unbiased bases implies high indistinguishability between the orthogonal polarization components, indicating strong nonlocality, even with nearly all spatial modes detected.

Following a similar method as described in [37,39], we calculate the CHSH parameter S from the coincidence rates via

$$S = |E(\theta_s, \theta_i) - E(\theta_s, \theta_i') + E(\theta_s', \theta_i) + E(\theta_s', \theta_i')|, \tag{2}$$

and $E(\theta_s, \theta_i)$ is defined as

$$E(\theta_s, \theta_i) = \frac{N(\theta_s, \theta_i) + N(\theta_s^\perp, \theta_i^\perp) - N(\theta_s, \theta_i^\perp) - N(\theta_s^\perp, \theta_i)}{N(\theta_s, \theta_i) + N(\theta_s^\perp, \theta_i^\perp) + N(\theta_s, \theta_i^\perp) + N(\theta_s^\perp, \theta_i)}, \tag{3}$$

$$\theta^\perp = \theta + 90^\circ, \tag{4}$$

where $\theta_{s(i)}^\perp$ stands for an angle perpendicular to $\theta_{s(i)}$. Here, we choose $\theta_s = 0^\circ$, $\theta_s' = 45^\circ$, $\theta_i = 67.5^\circ$, $\theta_i' = 22.5^\circ$. Consequently, the LED-pumped SPDC yields $S = 2.532 \pm 0.069$, which exceeds the classical limit of $S = 2$ by more than seven standard deviations. It is significant that here a violation of local realism has been demonstrated with highly spatially multimode two-photon states produced from SPDC pumped by an incoherent light source. More importantly, the CHSH-inequality violation and two-photon polarization entanglement (as will be quantified later by concurrence) measured in this work are significantly higher than those reported in previous works with either MMF or SMF collection of the incoherent-light-pumped SPDC. Table I summarizes and compares our results with those reported in earlier literature.

In contrast, the laser-pumped SPDC exhibits fringe visibilities of $97.69\% \pm 0.07\%$, $94.62\% \pm 0.10\%$, $95.08\% \pm 0.07\%$, and $93.40\% \pm 0.09\%$ in the H, V, A, and D bases, respectively. The corresponding S parameter is calculated as $S = 2.695 \pm 0.006$, displaying a violation of local realism by more than 115 standard deviations. While LED- and laser-pumped SPDC exhibit comparably high fringe visibility in the H-V bases, the laser-pumped SPDC results in a notably higher fringe visibility in the A-D bases and a stronger violation of local realism compared to LED-pumped SPDC. A reduced fringe visibility in the mutually unbiased basis can be attributed to two potential reasons: (i) the produced state has an additional phase between the $|HV\rangle$ and $|VH\rangle$ components compared to the target state $|HV\rangle - |VH\rangle$ so that the fringes measured in the A-D bases have reduced visibilities; (ii) the produced state has reduced entanglement, which manifests as a reduced indistinguishability in the mutually unbiased bases. To fully characterize the resulting two-photon states produced from different pump sources, we conduct quantum state tomography to reconstruct their density matrices ρ and calculate $C(\rho)$ to quantify the entanglement.

In Figs. 3(a) and 3(b), we depict the real and imaginary parts of the two-photon density matrices for LED- and laser-pumped SPDC, respectively. By calculating the phase of the $|VH\rangle\langle HV|$ element, we infer that the LED-pumped SPDC produces a state with $\phi = (-0.941 \pm 0.024)\pi$ and the laser-pumped SPDC produces a state with $\phi = (-0.943 \pm 0.001)\pi$. The fidelity of the experimentally measured state to the target state is $89.88\% \pm 0.51\%$ for LED-pumped SPDC and $96.36\% \pm 0.04\%$ for laser-pumped SPDC, respectively. These results indicate that we have chosen a near-optimal set of polarization projection bases. The two-photon state produced from LED-pumped SPDC has a concurrence of $C = 0.834 \pm 0.038$, whereas the one produced from laser-pumped SPDC has a concurrence of $C = 0.952 \pm 0.002$. The lower value of C observed for the LED-pumped SPDC means the produced state has a reduced entanglement compared to laser-pumped SPDC, while both produce nonmaximal entanglement [41]. Therefore, the lower violation of local realism of LED-pumped SPDC is mainly due to the reduced entanglement in the generated state. The concurrence results are consistent with the differences in fringe visibilities measured in the A-D basis since the entanglement is sensitive to the indistinguishability between the SPDC processes induced by pump light traversing the PSI in the clockwise and counterclockwise directions.

TABLE I. Summary and comparison of results in the existing literature on two-photon polarization entanglement produced from SPDC pumped by spatially incoherent light.

Reference	Concurrence	CHSH-inequality violation	Photon-collection scheme
Li *et al.* (2023) [32]	0.531 ± 0.038	N/A	MMF (200-μm core diameter, 0.39 NA)
Zhang *et al.* (2023) [33]	0.63	$S = 2.33 \pm 0.097 > 2$	SMF
	0.54	N/A	MMF (50-μm core diameter)
	0.35	N/A	MMF (125-μm core diameter)
This work	0.834 ± 0.038	$S = 2.532 \pm 0.069 > 2$	MMF (200-μm core diameter, 0.39 NA)

The nonmaximal entanglement produced from both types of pump sources can be attributed to the wave-front distortions within the PSI. Specifically, the uneven distances between the two cemented prisms comprising the dPBS cause the H and V components of both the pump and the down-converted photons to acquire different relative phases across the transverse plane. This effect is analogous to a wave plate with a spatially nonuniform phase retardation, which alters the polarization state of the light in a position-dependent manner. The influence of wave-front distortion experienced by the down-converted photons is discussed in Ref. [39] in the context of laser-pumped SPDC. Collecting the down-converted photons using MMFs effectively mixes highly entangled states [Eq. (1)] with different ϕ, thereby reducing the overall polarization entanglement.

In the case of laser-pumped SPDC, the influence of wave-front distortion on the pump beam is negligible since the laser beam's spot size is sufficiently small that the phase change appears uniform across its transverse profile. However, this effect becomes more prominent for LED-pumped SPDC. We depict the effect of wave-front distortion on the LED pump beam in Fig. 4(a). Since the light beam from an LED has a larger spot size than that of a laser, the pump beam picks up spatially varying polarization phase across its transverse profile. For instance, as shown in the inset to Fig. 4(a), pump photons entering the PSI through path 1 (solid line) acquire a relative phase of ϕ_1 between their H and V components, while those entering through path 2 (dashed line) acquire ϕ_2, with $\phi_1 \neq \phi_2$ in general. As a result, the down-converted photons generated from different transverse components of the LED pump already carry different two-photon polarization phases ϕ before undergoing further distortions at the dPBS. Therefore, the LED-pumped SPDC is a mixture of two-photon states with different ϕ, which are generated from pump

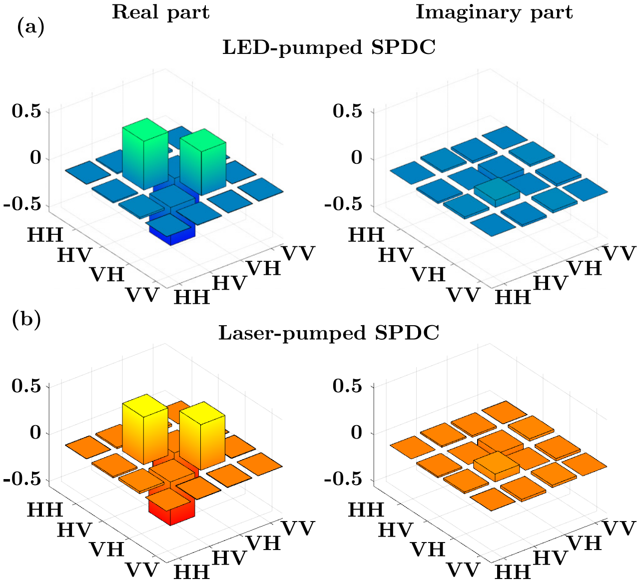

FIG. 3. Real and imaginary parts of the density matrices of the two-photon states produced with (a) LED-pumped SPDC and (b) laser-pumped SPDC. All elements of the density matrices have uncertainties less than 0.03 for LED-pumped SPDC and less than 0.003 for laser-pumped SPDC.

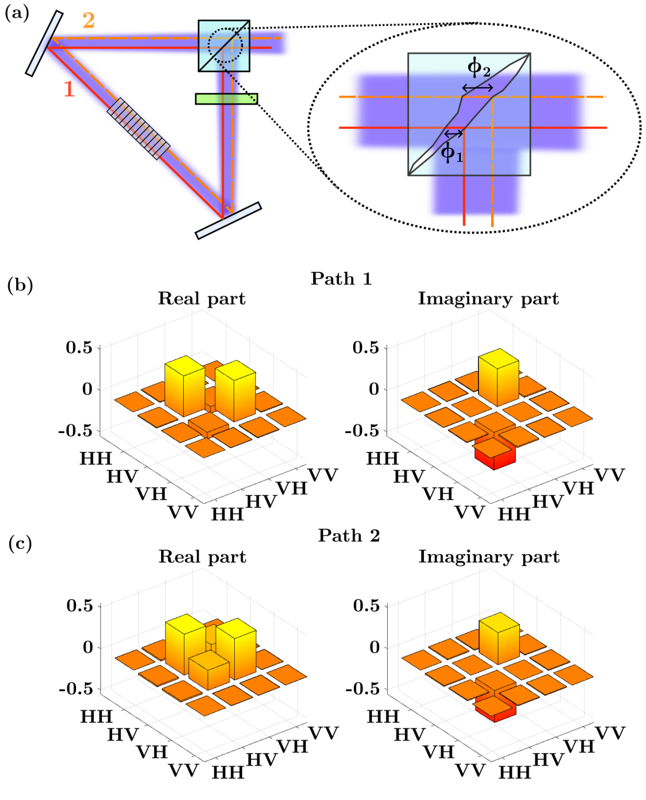

FIG. 4. (a) Schematic diagram of probing the effects of wave-front distortion on the produced two-photon state. The laser pump beam enters the PSI at two alternative paths with a horizontal shift of ~1 mm. The inset depicts the effect of wave-front distortion, which introduces different polarization phase retardation at different transverse positions of the pump beam. The uneven distances between the two cemented prisms are exaggerated for illustration purposes. The reconstructed density matrices of two-photon states produced in (b) path 1 and (c) path 2.

photons of different transverse positions. As a result, the detected states display reduced concurrence when averaging over all possible transverse positions. To characterize this effect, we adjust the alignment of the laser pump beam so that it can traverse the PSI in two alternative paths separated by ~1 mm in the horizontal direction, as depicted in Fig. 4(a). Consequently, the influence of wave-front distortion on the pump beam can be observed by comparing the resulting two-photon states produced from laser-pumped SPDC induced in different paths. In Figs. 4(b) and 4(c) we show the density matrices of the two-photon density matrices produced in paths 1 and 2, respectively. The two-photon state produced by the pump beam traversing path 1 yields $C = 0.933 \pm 0.001$ and $\phi = (0.5558 \pm 0.0002)\pi$, while that produced in path 2 exhibits $C = 0.916 \pm 0.001$ and $\phi = (0.3220 \pm 0.0001)\pi$. In both cases, the two-photon state displays strong ($C > 0.9$) entanglement, indicating that the SPDC processes induced in the clockwise and counterclockwise directions are sufficiently indistinguishable along either path. The observed nonmaximal entanglement is primarily due to the wave-front distortion experienced by the down-converted photons, which is similar to the results depicted in Fig. 3(b) and those reported in [39]. The two output states display a distinct two-photon polarization phase ϕ due to the pump beam entering the PSI at different transverse positions on the dPBS. Using a pump beam with a larger spot size effectively mixes the nonmaximal two-photon states with different ϕ produced in different paths from pump beams with smaller spot sizes, which further reduces the resulting entanglement. For instance, an equal mixture of the two states depicted in Figs. 4(b) and 4(c) has a lower concurrence of $C = 0.8558 \pm 0.0003$, which is comparable to that of the LED-pumped SPDC. These measurements suggest that the spatial coherence of the pump does not fundamentally limit the polarization entanglement produced from SPDC, and technical improvements can further enhance the produced entanglement.

IV. CONCLUSIONS AND PERSPECTIVES

In summary, we have demonstrated a violation of local realism with a highly spatially multimode two-photon state produced from SPDC pumped by a spatially incoherent light source—an LED. By collecting the down-converted photons with MMFs, we achieve a violation of the CHSH inequality $S = 2.532 \pm 0.069 > 2$ by more than seven standard deviations using a two-photon state containing nearly 4080 spatial modes. Tomography analysis shows that the two-photon state produced from LED-pumped SPDC has a concurrence of $C = 0.834 \pm 0.038$. These results represent the strongest violation of local realism and entanglement reported to date for incoherent-light-pumped SPDC. In contrast, SPDC pumped by a spatially coherent laser beam in the same setup results in $S = 2.695 \pm 0.006$ and $C = 0.952 \pm 0.002$. The reduced local realism violation and entanglement observed for LED-pumped SPDC are likely results of the wave-front distortion introduced by the imperfect optics parts within the PSI. We demonstrate this by observing that near-maximal entangled states produced from laser pump beams traversing different paths in the PSI are distinguishable by their two-photon polarization phase.

Our results inform future studies employing incoherent-light-pumped SPDC for practical entangled photon sources. For instance, one can compensate the wave-front distortions experienced by the pump and down-converted photons with additional phase masks or adaptive optics devices [42,43] to produce maximal entanglement from spatially incoherent light. The viability of producing high entanglement regardless of the pump's coherence opens up new opportunities for entanglement-based quantum information technologies. For instance, since incoherent light sources such as LEDs and sunlight are more ubiquitous and less power-consuming than most coherent light sources such as lasers, incoherent-light-pumped SPDC could be employed to build robust entangled photon sources without active electronics (other than temperature control of the nonlinear crystals), which extends the accessibility of quantum technologies in resource-restricted environments such as the Arctic region and satellites in space [19]. Furthermore, two-photon polarization-entangled states produced from SPDC pumped by incoherent light may be more suitable for free-space quantum key distribution due to their robustness against atmospheric turbulence [44–46]. In the broader context of entangled photon generation using nonlinear optical methods, a recent study demonstrated that four-wave mixing driven by amplified spontaneous emission can produce highly entangled two-photon states with enhanced pair generation rates [47], underscoring the potential of incoherent-light-driven quantum information technologies with nonlinear optical platforms.

ACKNOWLEDGMENTS

C.L. acknowledges useful discussions with Yingwen Zhang, Alessio D'Errico, Yang Xu, and Jiapeng Zhao. The portion of the work performed at the University of Ottawa was supported by the Canada Research Chairs Program under Award No. 950-231657, the Natural Sciences and Engineering Research Council of Canada under Alliance Consortia Quantum Grant No. ALLRP 578468-22, Discovery Grant No. RGPIN/2017-06880, and the Canada First Research Excellence Fund Award No. 072623. In addition, R.W.B. acknowledges support through the U.S. National Science Foundation through Award No. 2138174 and the U.S. Department of Energy through Award No. FWP 76295.

DATA AVAILABILITY

The data that support the findings of this article are not publicly available. The data are available from the authors upon reasonable request.

[1] A. Einstein, B. Podolsky, and N. Rosen, Can quantum-mechanical description of physical reality be considered complete? Phys. Rev. **47**, 777 (1935).

[2] J. S. Bell, On the Einstein Podolsky Rosen paradox, Phys. Phys. Fiz. **1**, 195 (1964).

[3] J. F. Clauser, M. A. Horne, A. Shimony, and R. A. Holt, Proposed experiment to test local hidden-variable theories, Phys. Rev. Lett. **23**, 880 (1969).

[4] C. H. Bennett and G. Brassard, Quantum cryptography: Public key distribution and coin tossing, *Proceedings of IEEE International Conference on Computers, Systems and Signal Processing* (IEEE, New York, 1984), pp. 175–179.

[5] A. K. Ekert, Quantum cryptography based on Bell's theorem, Phys. Rev. Lett. **67**, 661 (1991).

[6] D. Mayers and A. Yao, Quantum cryptography with imperfect apparatus, *Proceedings of the 39th Annual Symposium on Foundations of Computer Science (FOCS)* (IEEE, New York, 1998), pp. 503–509.

[7] P.-A. Moreau, E. Toninelli, T. Gregory, R. S. Aspden, P. A. Morris, and M. J. Padgett, Imaging Bell-type nonlocal behavior, Sci. Adv. **5**, eaaw2563 (2019).

[8] A. Niezgoda and J. Chwedeńczuk, Many-body nonlocality as a resource for quantum-enhanced metrology, Phys. Rev. Lett. **126**, 210506 (2021).

[9] B. Yadin, M. Fadel, and M. Gessner, Metrological complementarity reveals the Einstein-Podolsky-Rosen paradox, Nat. Commun. **12**, 2410 (2021).

[10] D. C. Burnham and D. L. Weinberg, Observation of simultaneity in parametric production of optical photon pairs, Phys. Rev. Lett. **25**, 84 (1970).

[11] C. K. Hong and L. Mandel, Theory of parametric frequency down conversion of light, Phys. Rev. A **31**, 2409 (1985).

[12] R. W. Boyd, *Nonlinear Optics* (Academic Press, San Diego, CA, 2020).

[13] Y. H. Shih and C. O. Alley, New type of Einstein-Podolsky-Rosen-Bohm experiment using pairs of light quanta produced by optical parametric down conversion, Phys. Rev. Lett. **61**, 2921 (1988).

[14] Z. Y. Ou and L. Mandel, Violation of Bell's inequality and classical probability in a two-photon correlation experiment, Phys. Rev. Lett. **61**, 50 (1988).

[15] T. E. Kiess, Y. H. Shih, A. V. Sergienko, and C. O. Alley, Einstein-Podolsky-Rosen-Bohm experiment using pairs of light quanta produced by type-II parametric down-conversion, Phys. Rev. Lett. **71**, 3893 (1993).

[16] T. Jennewein, C. Simon, G. Weihs, H. Weinfurter, and A. Zeilinger, Quantum cryptography with entangled photons, Phys. Rev. Lett. **84**, 4729 (2000).

[17] R. Ursin, F. Tiefenbacher, T. Schmitt-Manderbach, H. Weier, T. Scheidl, M. Lindenthal, B. Blauensteiner, T. Jennewein, J. Perdigues, P. Trojek, B. Ömer, M. Fürst, M. Meyenburg, J. Rarity, Z. Sodnik, C. Barbieri, H. Weinfurter, and A. Zeilinger, Entanglement-based quantum communication over 144 km, Nat. Phys. **3**, 481 (2007).

[18] A. N. Black, E. Giese, B. Braverman, N. Zollo, S. M. Barnett, and R. W. Boyd, Quantum nonlocal aberration cancellation, Phys. Rev. Lett. **123**, 143603 (2019).

[19] J. Yin, Y.-H. Li, S.-K. Liao, M. Yang, Y. Cao, L. Zhang, J.-G. Ren, W.-Q. Cai, W.-Y. Liu, S.-L. Li, R. Shu, Y.-M. Huang, L. Deng, L. Li, Q. Zhang, N.-L. Liu, Y.-A. Chen, C.-Y. Lu, X.-B. Wang, F. Xu *et al.*, Entanglement-based secure quantum cryptography over 1,120 kilometres, Nature (London) **582**, 501 (2020).

[20] H. Defienne, B. Ndagano, A. Lyons, and D. Faccio, Polarization entanglement-enabled quantum holography, Nat. Phys. **17**, 591 (2021).

[21] A. K. Jha and R. W. Boyd, Spatial two-photon coherence of the entangled field produced by down-conversion using a partially spatially coherent pump beam, Phys. Rev. A **81**, 013828 (2010).

[22] E. Giese, R. Fickler, W. Zhang, L. Chen, and R. W. Boyd, Influence of pump coherence on the quantum properties of spontaneous parametric down-conversion, Phys. Scr. **93**, 084001 (2018).

[23] C. H. Monken, P. H. S. Ribeiro, and S. Pádua, Transfer of angular spectrum and image formation in spontaneous parametric down-conversion, Phys. Rev. A **57**, 3123 (1998).

[24] H. Defienne and S. Gigan, Spatially entangled photon-pair generation using a partial spatially coherent pump beam, Phys. Rev. A **99**, 053831 (2019).

[25] W. Zhang, R. Fickler, E. Giese, L. Chen, and R. W. Boyd, Influence of pump coherence on the generation of position-momentum entanglement in optical parametric down-conversion, Opt. Express **27**, 20745 (2019).

[26] A. V. Burlakov, M. Chekhova, O. Karabutova, and S. P. Kulik, Biphoton interference with a multimode pump, Phys. Rev. A **63**, 053801 (2001).

[27] A. K. Jha, M. N. O'Sullivan, K. W. C. Chan, and R. W. Boyd, Temporal coherence and indistinguishability in two-photon interference effects, Phys. Rev. A **77**, 021801(R) (2008).

[28] G. Kulkarni, P. Kumar, and A. K. Jha, Transfer of temporal coherence in parametric down-conversion, J. Opt. Soc. Am. B **34**, 1637 (2017).

[29] G. Kulkarni, V. Subrahmanyam, and A. K. Jha, Intrinsic upper bound on two-qubit polarization entanglement predetermined by pump polarization correlations in parametric down-conversion, Phys. Rev. A **93**, 063842 (2016).

[30] N. Meher, A. S. M. Patoary, G. Kulkarni, and A. K. Jha, Intrinsic degree of coherence of two-qubit states and measures of two-particle quantum correlations, J. Opt. Soc. Am. B **37**, 1224 (2020).

[31] L. Hutter, G. Lima, and S. P. Walborn, Boosting entanglement generation in down-conversion with incoherent illumination, Phys. Rev. Lett. **125**, 193602 (2020).

[32] C. Li, B. Braverman, G. Kulkarni, and R. W. Boyd, Experimental generation of polarization entanglement from spontaneous parametric down-conversion pumped by spatiotemporally highly incoherent light, Phys. Rev. A **107**, L041701 (2023).

[33] W. Zhang, D. Xu, and L. Chen, Polarization entanglement from parametric down-conversion with an LED pump, Phys. Rev. Appl. **19**, 054079 (2023).

[34] J. B. Altepeter, E. R. Jeffrey, and P. G. Kwiat, Phase-compensated ultra-bright source of entangled photons, Opt. Express **13**, 8951 (2005).

[35] R. Rangarajan, M. Goggin, and P. Kwiat, Optimizing type-I polarization-entangled photons, Opt. Express **17**, 18920 (2009).

[36] C. E. Kuklewicz, M. Fiorentino, G. Messin, F. N. C. Wong, and J. H. Shapiro, High-flux source of polarization-entangled photons from a periodically poled KTiOPO$_4$ parametric down-converter, Phys. Rev. A **69**, 013807 (2004).

[37] P. G. Kwiat, E. Waks, A. G. White, I. Appelbaum, and P. H. Eberhard, Ultrabright source of polarization-entangled photons, Phys. Rev. A **60**, R773 (1999).

[38] C. Li, G. Kulkarni, I. Soward, Y. Zhang, J. Upham, D. England, A. Nomerotski, E. Karimi, and R. Boyd, Imaging cross-degree-of-freedom structures in biphoton spatial-polarization hyperentanglement, arXiv:2502.03586.

[39] T. Kim, M. Fiorentino, and F. N. C. Wong, Phase-stable source of polarization-entangled photons using a polarization Sagnac interferometer, Phys. Rev. A **73**, 012316 (2006).

[40] D. F. V. James, P. G. Kwiat, W. J. Munro, and A. G. White, Measurement of qubits, Phys. Rev. A **64**, 052312 (2001).

[41] W. K. Wootters, Entanglement of formation of an arbitrary state of two qubits, Phys. Rev. Lett. **80**, 2245 (1998).

[42] H. Defienne, M. Reichert, and J. W. Fleischer, Adaptive quantum optics with spatially entangled photon pairs, Phys. Rev. Lett. **121**, 233601 (2018).

[43] P. Cameron, B. Courme, C. Vernière, R. Pandya, D. Faccio, and H. Defienne, Adaptive optical imaging with entangled photons, Science **383**, 1142 (2024).

[44] A. Bhattacharjee and A. K. Jha, Experimental demonstration of structural robustness of spatially partially coherent fields in turbulence, Opt. Lett. **45**, 4068 (2020).

[45] Y. Qiu and W. She, The influence of atmospheric turbulence on partially coherent two-photon entangled field, Appl. Phys. B **108**, 683 (2012).

[46] S. P. Phehlukwayo, M. L. Umuhire, Y. Ismail, S. Joshi, and F. Petruccione, Influence of coincidence detection of a biphoton state through free-space atmospheric turbulence using a partially spatially coherent pump, Phys. Rev. A **102**, 033732 (2020).

[47] Y.-W. Song, H. Zhao, L. Chen, Y.-H. Li, E.-Z. Li, M.-Y. Gao, R.-H. Chen, Z.-Q.-Z. Han, M.-Y. Xie, G.-C. Guo, Z.-Y. Zhou, and B.-S. Shi, On chip quantum states generation by incoherent light, arXiv:2412.03802.

Chapter 5

Generating quantum entanglement from sunlight

The idea of generating entangled photons from sunlight-pumped SPDC comes up frequently during group discussions on my thesis topic. It started to materialize in October 2023 at the annual meeting of Max Planck—uOttawa Centre for Extreme and Quantum Photonics, which was hosted by the Max Planck Institute for the Science of Light (MPL) in Erlangen, Germany. During the meeting, I learned that Dr. Hanieh Fattahi's team at the MPL was developing a specialized glass concentrator that could potentially couple sunlight into optical fibers. Through discussions with Dr. Hanieh Fattahi and her student, Mr. Michael Küblböck, I was convinced of the feasibility of pumping SPDC with concentrated sunlight. I then formalized the collaboration with support from Dr. Jeremy Upham and Prof. Robert Boyd.

5.1 Estimating the optimal pump wavelength

While sunlight is inherently broadband, SPDC can only convert the pump light within a narrow spectral range, as dictated by the phase-matching condition of a given nonlinear crystal. To seamlessly integrate Dr. Fattahi's expertise with ours, we need to first select an optimal wavelength for a given entangled-photon source setup so that the sunlight concentration module can be optimized for maximal concentration efficiency at that wavelength. We have performed this wavelength estimation by considering a periodically-poled potassium titanyl phosphate (ppKTP) crystal quasi-phase-matched for Type-II degenerate SPDC, which composes one of the brightest entangled-photon sources to date, including the one we used in Chapter 4.

We model the photon pair generation rate from the PDC process by adapting the framework in Ref. [50, 51]. The down-converted photon flux generated and emitted into the signal(idler) mode from a crystal with length L is calculated from the following expression:

$$N_{dc} = \int_0^\infty \int_{-\pi/2}^{\pi/2} \int_{-\pi/2}^{\pi/2} \frac{\beta L^2}{\hbar \omega_{dc}} P(\omega_p, \phi, \theta) q(\omega_{dc}) \sin^2\left(\frac{\Delta k L}{2}\right) d\phi \, d\theta \, d\omega_{dc}, \tag{5.1}$$

where P is the the power of pump beam, which is dependent on its frequency ω_p, and angular spectrum (ϕ, θ), β is the nonlinear conversion coefficient, $q(\omega_{dc})$ is the detection quantum efficiency of the down-converted photons, and Δk is the wave vector mismatch between pump, signal, and idler fields.

The nonlinear conversion coefficient is β given by [52]

$$\beta = \frac{\omega_s^4 \omega_i d_{\text{eff}}^2 \hbar n_s}{4\pi^3 \epsilon_0 c^5 n_i n_p} = \frac{\omega_{dc}^5 d_{\text{eff}}^2 \hbar}{4\pi^3 \epsilon_0 c^5 n_p}, \tag{5.2}$$

where we have assumed the case of degenerate phase-matching so that $\omega_s = \omega_i = \omega_{dc}$ and $n_s = n_i$. For simplicity, we may also assume perfect phase-matching and detection efficiency over all spatial modes, so that the pair generation rate is seen as proportional to the following expression, which we denote as R:

$$R = \frac{\beta}{\hbar \omega_{dc}} P(\omega_p) = \frac{4\pi d_{\text{eff}}^2}{(2\lambda_p)^4 \epsilon_0 c n_p} P(\lambda_p), \tag{5.3}$$

where we have changed the variable to wavelength and used $\lambda_{dc} = 2\lambda_p$. We then use this expression to estimate the optimal pump wavelength by considering the wavelength dependence of both the solar irradiance and the second-order nonlinear coefficient.

Fig. 5.1a depicts the ASTM G173-03 Reference spectra of solar irradiance [53]. We use the direct and circumsolar irradiance data as a benchmark for the sunlight pump power spectrum [54]. While solar irradiance peaks around 500 nm and sharply declines at shorter wavelengths, the second-order nonlinear coefficients of most materials tend to increase in this range with decreasing wavelengths. We calculate the dispersion of d using [55]:

$$d_{il}(\lambda) = \chi^{(1)}(\lambda) \bar{d}_{il} \tag{5.4}$$

where $\bar{d}_{il}$ is a material-specific constant. Since a Type-II ppKTP crystal is x-cut, we choose

$$d_{\text{eff}} = d_{24} = 1.68\chi^{(1)} = 1.68[n_\beta^2(\lambda) - 1] \tag{5.5}$$

where $n_\beta(\lambda)$ is the β-axis refractive index of KTP. Fig. 5.2 depicts the dispersion of d as presented in Ref. [55].

Fig. 5.3 depicts the numerical results of estimated values of R, which is proportional to the expected pair generation rate. In Fig. 3a, we plot the value of R from 350 nm to 600 nm. It is evident that although the solar irradiance is stronger at 500 nm,

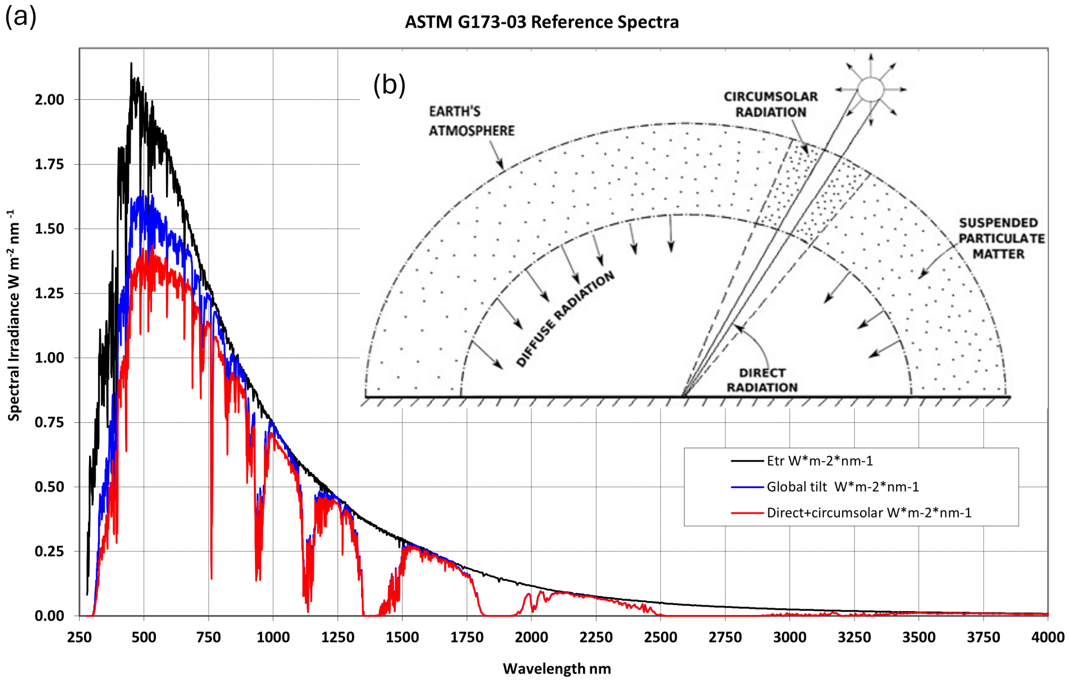

Figure 5.1: (a) ASTM G173-03 solar irradiance data. Etr—extraterrestrial solar irradiance. Global tilt—irradiance on 37° tilted sun-facing surface. Direct+circumsolar—surface normal to the Sun and its surroundings. (b) Conceptual diagram of the direct+circumsolar measurement regime. Figures adapted from Ref. [53, 54].

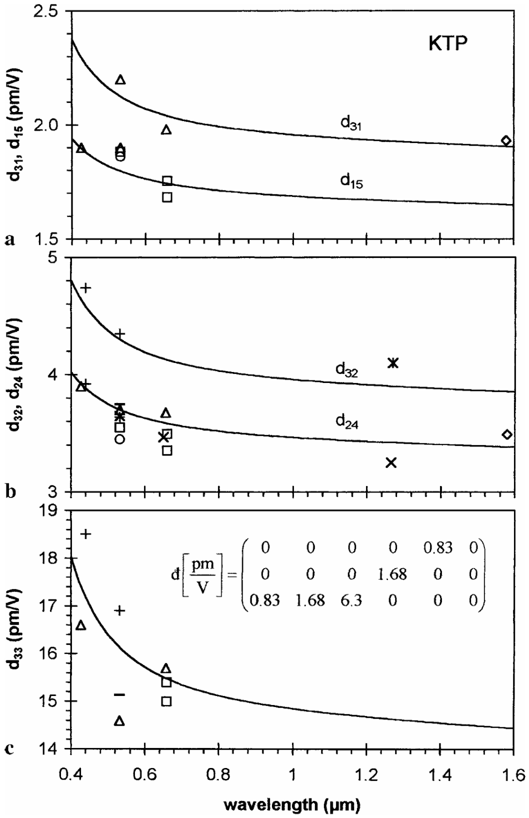

FIGURE 5.2: Dispersion of second-order nonlinear optical coefficients of KTP. The data markers represent experimentally measured values from different earlier publications. Figure adapted from [55].

the expected coincidence is higher when the pump wavelength is around 400 nm. In Fig. 3b, we depict R around 400 nm and notice that the coincidence rate has negligible wavelength dependence in the range of 400 nm to 410 nm. These results indicate that a wavelength between 400 nm and 410 nm could be the optimal pump wavelength for generating entangled photons using sunlight-pumped SPDC.

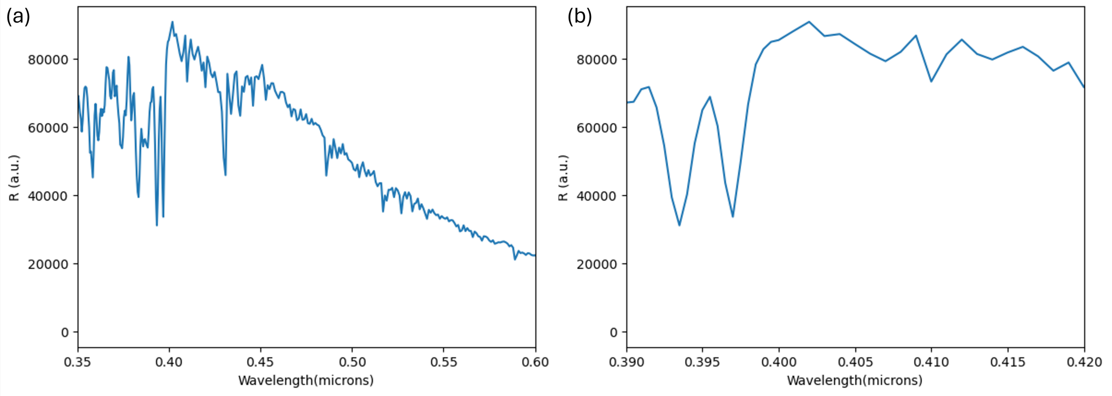

FIGURE 5.3: Estimated coincidence rates in different wavelength ranges using a ppKTP crystal with Type-II degenerate quasi-phase-matching.

In Fig. 5.4 we depict a comparison between the solar irradiance, which is proportional to the power of the solar pump and $\beta/\hbar\omega_{dc}$. By plotting log scales and normalizing with their values at 400 nm, we observe that from 400 nm to 500 nm, the increase in solar irradiance appears marginal in contrast to the sharp drop in nonlinear conversion efficiency.

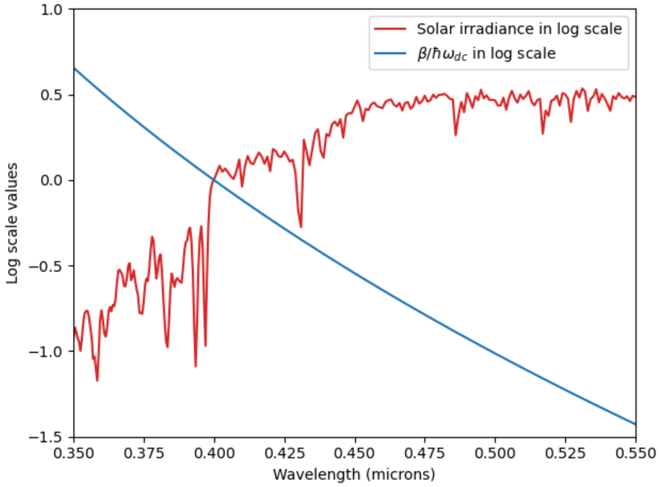

FIGURE 5.4: Comparison of solar irradiance and nonlinear conversion efficiency

Fortunately, our lab already has a ppKTP crystal quasi-phase-matched for Type-II degenerate SPDC from 405 nm to 810 nm. Therefore, we have decided to use this crystal in the entangled-photon source, which we had been building in the work that later led to

Chapter 4. Working in parallel with our efforts to build the entangled-photon source, Dr. Fattahi's team, specifically her students, Mr. Jasvinder Brar and Mr. Michael Küblböck, optimized the design of their solar concentration module to prioritize the collection of sunlight around 405 nm. In particular, they have aimed at efficient coupling of concentrated sunlight into a multimode fiber (MMF) so that the sunlight can be guided into our free-space entangled-photon source. While a detailed discussion on solar concentration is beyond the scope of this thesis, we have included a brief description in the Supplementary Material of this work. For more information, one may refer to Ref. [56].

5.2 Integration optimization of sunlight-pumped entangled-photon source

In Aug 2025, I travelled to Germany on a business visa to conduct the first test round for this experiment. With limited resources at our disposal, we shipped most optical components composing the entangled-photon source from Ottawa to Erlangen so that I could rebuild the entangled-photon source at the MPL. Additionally, we borrowed single-photon detection equipment from Dr. Christoph Marquardt's group at the MPL.

Ideally, a free-space optical entangled-photon setup should be stabilized on an optics table inside an enclosed lab space, while the concentrated sunlight collected from outdoors is sent into the lab through an optical fiber. However, due to the significant absorption of 405 nm light by silica, we decided to place the entangled-photon source outdoors, next to the sunlight concentration module, to minimize pump-power loss. I rebuilt the setup used in Chapter 4 more compactly on a breadboard. The setup, which is aligned in the lab, can then be transported to the outdoor space on a cart. To shield the setup from the bright ambient light in an outdoor space, I worked with Mr. Jasvinder Brar to design and build an optical enclosure, whose front and top panels are made into an L-shaped lid. To minimize disturbance to the setup's alignment during transportation, we also equipped the breadboard with passive vibration-absorbing feet. The experimental setup used in this first test round is depicted in Fig. 5.5.

However, the difficulties in conducting quantum optical experiments outdoors were still beyond our estimation. First, we were constrained by the geological factors. The ideal weather condition for this experiment—sunny days with clear sky—is not typical at Erlangen. Even on relatively sunny days, our measurements could be interrupted with unexpected cloud coverage. Additionally, solar irradiance on earth's surface varies with time of the day and may only be strong enough within 2 hours from noon. This further restricts the time window for conducting a full state tomography measurement.

Despite the effort in mitigating the vibration during transportation, the setup still experiences misalignment in the process. Specifically, the mirrors in the Sagnac polarization

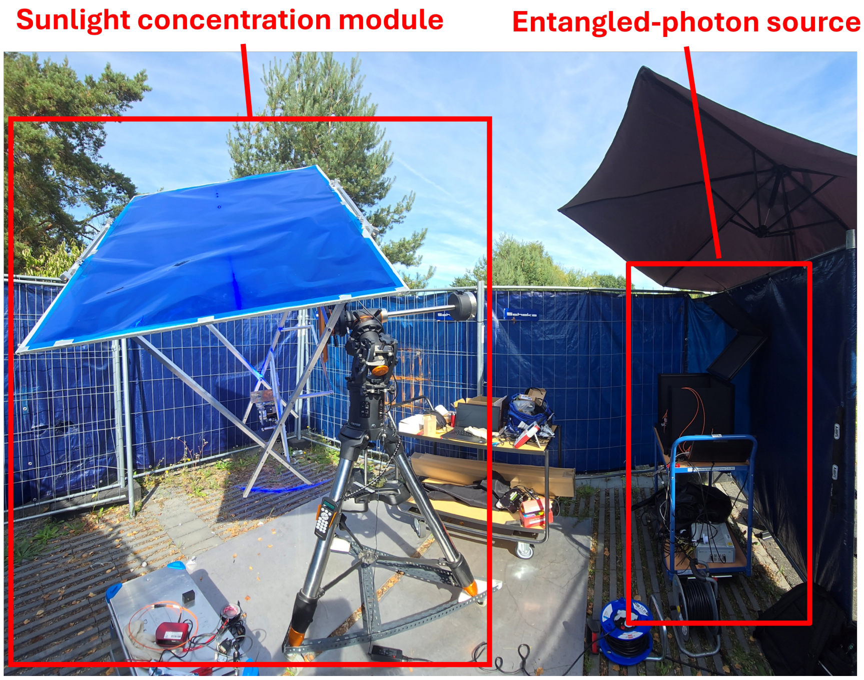

Figure 5.5: Field test setup for integration of the sunlight concentration module and the entangled-photon source.

interferometer ended up in slightly different tilt angles, which introduces spatial distinguishability between the SPDC processes produced in two directions and reduces the resulting entanglement. The misalignment then requires that we troubleshoot the setup on-site, which could expose the detectors under broad daylight. Since fine adjustment of the alignment requires observing quantum interferences between single-photons, an exposure to even the faintest ambient light could disrupt the optical precision. Although I attempted aligning the setup in the dark hours before dawn, the wind during daytime could also disturb the aligned setup during measurements. Nevertheless, the two-photon state generated from sunlight-pumped SPDC during the first test round still yields a concurrence of ~ 0.6.

On the other hand, sunlight exposure caused significant accumulation of heat at the metallic mounts of the filters composing the sunlight concentration module, which could lead to irreversible setup damage and even fire hazard. This risk factor had forced us to aggressively remove the warm light components by covering the input of the concentration module with multiple layers of blue-coloured films. However, these commercial grade films are not designed for optical filtering and only offers $\sim 70\%$ of transmission at 405 nm per layer. As a result, while they excel at blocking warm-coloured light, they also introduce significant loss at our desired pump wavelength. Furthermore, we discovered that an optical filter within the sunlight concentration module has much lower transmission at 405 nm than its manufacturer claims. Fortunately, we still managed to detect 30 photon pairs per 5-minute with an average sunlight pump power of ~ 70 nW.

These encouraging preliminary results had strengthened our confidence in this experiment and we quickly proceed to resolve these issues. To better isolate the setup from wind and ambient light, we acquired a blackout tent to house the setup in an outdoor environment. Consequently, we can easily fine-tune the alignment of the entangled-photon source on-site while enjoying better resistance against wind disturbance. To balance thermal management and operation efficiency of the sunlight concentration module, we carefully reduced the number of layers of the coloured film and installed a copper panel to shield the filter mounts from direct sunlight exposure. These improvements have increased the sunlight concentration efficiency at 405 nm and allowed us to observe nearly 45 photon pairs per 3-minute with $\sim$ 120 nW of average pump power. The higher coincidence counts effectively reduced the required measurement time. As a result, we can perform a full state tomography and a complete Bell test within the same sunny day while accommodating a few occasions of cloud coverage.

While I had to leave Germany due to visa expiration in early September, we immediately planned my second visit from October to early December, during which the aforementioned improvements were implemented. The details of the improved setup and the results obtained with it are discussed in the manuscript presented later in this Chapter. Below I summarize the contributions of all co-authors.

Mr. Jasvinder Brar and Mr. Michael Küblböck designed and built the solar concentration module in Fig. 1. I built the entangled photon source in Fig. 1, which is a slightly modified version of that used in Chapter 4. With technical support from Mr. Michael Küblböck, Mr. Jasvinder Brar and I worked closely together to measure the entangled photons generated from sunlight-pumped SPDC. Mr. Jasvinder Brar and I optimized both setups for improved sunlight collection efficiency and setup stability in outdoor environments, achieving the results shown in Fig. 2-4. Mr. Jasvinder Brar and I analyzed the results through discussions with Dr. Jeremy Upham and Dr. Hanieh Fattahi. I wrote the first draft of the manuscript together with Mr. Jasvinder Brar, and all co-authors subsequently contributed to the writing. Dr. Hanieh Fattahi and Prof. Robert Boyd supervised the research. This paper is currently under review at Optica.

Generating quantum entanglement from sunlight

Cheng Li[1†,*], Jasvinder Brar[2,3†], Michael Küblböck[2,3],
Jeremy Upham[1], Hanieh Fattahi[2,3*], Robert W. Boyd[1,4*]

[1]Department of Physics, University of Ottawa, Ottawa, Ontario, Canada K1N 6N5.

[2]Max Planck Institute for the Science of Light, Erlangen, Germany.

[3]Friedrich-Alexander-Universität Erlangen-Nürnberg, Erlangen, Germany.

[4]Institute of Optics, University of Rochester, Rochester, New York 14627, USA.

[*]Corresponding authors. Emails: hanieh.fattahi@mpl.mpg.de; rboyd@uottawa.ca

[†]These authors contributed equally to this work.

Energy consumption is becoming a serious bottleneck for integrating quantum technologies within the existing global information infrastructure. In photonic architectures, considerable energy overheads stem from using lasers, whose high coherence was long considered indispensable for quantum state preparation. Here, we demonstrate that natural, incoherent sunlight can successfully produce quantum-entangled states via spontaneous parametric down-conversion. We detect polarization-entangled photon pairs with a concurrence of 0.905 ± 0.053 and a Bell state fidelity of 0.939 ± 0.027. Importantly, the system violates Bell's inequality with $S = 2.5408 \pm 0.2171$, exceeding the classical threshold of 2, while maintaining generation rates comparable to laser-based setups. These findings pave the way for sustainable quantum applications in resource-limited environments like interplanetary missions.

Background

Quantum technologies have promised to revolutionize modern information processing, offering computational advantages for classically hard problems (*1–3*), information-theoretic communication security (*4–6*), and sensing precision beyond classical shot-noise limits (*7, 8*). Over the past few decades, breakthroughs in device performance have been widely celebrated in both scientific journals and the popular press, while a critical figure of merit for these advances—the energy cost—has raised concerns for their sustainability (*9*). In the classical domain, the global information and communication technology sector already accounts for ∼ 1.8–3.9% of worldwide greenhouse gas emissions and energy use (*10, 11*). With the ever-growing global data traffic, any large-scale deployment of quantum-enabled information and communication technology will inevitably add to this burden.

On existing quantum platforms, a substantial share of the power consumption stems from the energy overhead required to prepare and control the physical quantum systems. Preserving quantum coherence in superconducting circuits requires millikelvin-level cooling, which is provided by cryogenic equipment that routinely consumes 5-10 kW of electrical power per unit (*12, 13*). Ion-trap processors require energy-intensive resources such as ultra-high-vacuum infrastructure and high-power radiofrequency drive fields (*14*). In photonic quantum systems, generating quantum states of light often involves deploying lasers, which have suboptimal electrical-to-optical conversion efficiency due to their inherent requirement of operating above a driving current threshold. Commercial lasers typically draw watts of electrical power only to deliver optical power on the milliwatt scale, with a significant portion of the consumed energy going towards spectrum stabilization and temperature control, or dissipating as heat. Moreover, their durability and long-term reliability are limited when operating in harsh conditions such as intense radiation, high vacuum, and extreme temperature fluctuations. The energy requirements for these platforms could significantly constrain the scalability and accessibility of quantum technologies. Fortunately, operations of photonic quantum systems may not require enduring the energy burden from lasers, unlike superconducting and ion-trap systems, whose underlying physical principles necessitate the energy overheads.

A key ingredient in photonic quantum technologies is the entangled photon state (*15–20*). Lasers often serve as the pump source for generating entangled photons from spontaneous parametric down-conversion (SPDC), which is a nonlinear optical process widely employed in many photonic quantum applications. In SPDC, photons from a pump beam interact with a nonlinear medium and are down-converted into photon pairs (*21–23*). Conventionally, lasers are employed as pump sources due to their typically high coherence across all degrees of freedom, including spatial, spectral-temporal, and polarization. The reason is that the coherence of the pump in a given degree of freedom puts an upper bound on the maximally attainable entanglement in the same degree of freedom (*24–33*). However, this constraint does not apply when the target entanglement is in a different degree of freedom from that of the coherence of the pump (*34*). For instance, studies from the authors, as well as others, have demonstrated that a polarized but spatiotemporally incoherent light source, such as a light-emitting diode (LED), can produce polarization-entangled photon pairs via SPDC (*35–37*). These earlier achievements suggest that natural sources of light, such as sunlight, can replace lasers as the pump source for nonlinear optical processes and generate entangled photons, thereby enabling energy-efficient quantum technologies.

Solar energy harvesting through photovoltaics offers a prominent option for green, renewable power supply. However, the efficiency of state-of-the-art solar cells remains below 50% (*38*), and their performance and durability are similarly constrained in severe environmental conditions. In parallel with the materials science effort in solar cell research, sunlight concentration technologies have been developed over the years to facilitate optimal utilization of solar power (*39*). Studies have proposed using solar concentration technology to directly drive optical amplification and build a solar laser (*40–42*). On the other hand, large-scale solar-powered space infrastructure, such as space-based solar power platforms (*43*) and orbital data centers (*44*), is rapidly advancing, driving interest in photonic technologies capable of operating directly on abundant, incoherent solar radiation without dependence on power-intensive laser or electrical subsystems. Within this landscape, solar-driven photonic quantum technologies represent a promising route toward energy-autonomous quantum photonic functionality, naturally aligned with the requirements of future space power and information architectures. Here, we demonstrate, for the first time, that sunlight, a ubiquitous and environmentally friendly light source, can produce entangled photon pairs via SPDC despite its lack of optical coherence. Using a combination of a Fresnel lens and a conic concentrator, we couple the sunlight into a multimode fiber (MMF) that guides the sunlight into a free-space optical entanglement source setup. The spectrally filtered sunlight then pumps a nonlinear crystal placed inside a polarization Sagnac interferometer (PSI) to induce SPDC (*45*). We measure photon coincidences with a time correlation width of $\sim$ 1 ns. By conducting quantum state tomography (*46*), we measure a two-photon state with a concurrence of $C = 0.905 \pm 0.053$ (*47*), a purity of $P = 0.919 \pm 0.045$, and a fidelity to the target Bell state of $F = 0.939 \pm 0.027$. The polarization correlations between photon pairs result in a Bell parameter for a Clauser-Horne-Shimony-Holt (CHSH)-type measurement of $S = 2.5408 \pm 0.2171$ (*48, 49*), which surpasses the local realistic threshold of $S = 2$ by 2.49 standard deviations, indicating that the correlation cannot be fully explained by a local hidden variable theory. These results are not simply a proof of principle that polarization entanglement is generated from SPDC pumped by sunlight; they are a quantitative demonstration that these photon pairs have entanglement close to that of many recent results on polarization entanglement generated from SPDC pumped by coherence laser sources (*50–53*). We attribute the non-maximal entanglement and purity to practical imperfections in the experimental conditions, such as the wavefront distortions introduced by optical components, not to any inherent issue with the coherence of our solar pump. More importantly, we observe that the generation rate of entangled photons from sunlight-pumped SPDC, which is $\sim 1600\ \mathrm{s}^{-1}$ (mW of pump power)$^{-1}$, is comparable with that of laser-pumped SPDC when normalized against the effective phase-matching bandwidth. Our proof-of-principle demonstration not only indicates that there is no physical impediment to generating entangled photon pairs from incoherent sunlight, but is also highly encouraging that technical optimization of sunlight concentration at the phase-matching wavelengths of SPDC could make it competitive with current laser-pumped sources of polarization entangled photon sources. Our results serve as an important step towards solar-driven photonic quantum technologies and have important implications for developing energy-efficient and environmentally friendly quantum devices.

Experiment

Figure 1 depicts the experimental setup, which consists of a sunlight-concentration module and an entangled-photon source. The sunlight concentration module is designed to optimally isolate sunlight in the desired spectral bandwidth and couple them into the MMF. To this end, we first pre-focus the sunlight using a rectangular (1 m × 1.4 m) Fresnel lens covered with commercial-grade color films that partially block the warm-colored spectral components. This beam then propagates through a short-pass filter and a dichroic mirror to further reduce the optical power outside of the ultraviolet spectral band. The focused and filtered sunlight is then coupled into a MMF with a core diameter of 50 μm and numerical aperture (NA) of 0.22 (MMF-50-0.22) using a custom glass conic concentrator. Additional details relevant to the sunlight concentration module are included in the Materials and Methods section of the Supplementary Material.

To efficiently couple the sunlight into the nonlinear medium responsible for inducing SPDC, we first collimate the sunlight transmitted through the MMF into a beam using a microscope objective with 20× magnification and 0.4 NA. This beam, which will later serve as the pump of the SPDC processes, is spectrally filtered using a short-pass filter with a cutoff wavelength of 550 nm and a band-pass filter with a center wavelength of 405 nm and a bandwidth of 1.5 nm (BPF-405). Using a combination of a polarizing beam splitter (PBS) and a half-wave plate (HWP), we make the pump beam highly polarized with equal amplitudes in its horizontal and vertical components, which ensures the generation of high polarization entanglement (*32*). To account for the overall phase delays that the orthogonal polarization components may later experience, we add a quarter-wave plate (QWP) that can be tilted to pre-compensate for the expected phase differences. The polarized sunlight pump beam is then focused into the nonlinear medium using a lens with a focal length of $f_1 = 200$ mm. The filtered sunlight reflected by the PBS is sent to a power meter to monitor the pump power in real time or to a spectrometer to measure its spectrum. Since sunlight is nearly unpolarized, and considering the depolarizing effect of propagation in MMFs, we expect the pump power to be equally split at the PBS so that the power meter readings reflect the actual pump power incident on the nonlinear medium. Similarly, we expect the PBS to have negligible influence on the spectral shape of light around 405 nm, so that the spectrum measured at the spectrometer reflects the spectrum of the actual pump beam that induces the SPDC process. We depict the spectrum of the filtered sunlight pump beam in the inset of Fig. 1. At the center of the nonlinear medium, the sunlight pump beam has a diameter of ~ 1 mm with an estimated divergence half-angle of 11 mrad.

The nonlinear medium is a 10-mm-long periodically poled potassium titanyl phosphate (ppKTP) crystal quasi-phase-matched for Type-II SPDC from 405 nm to 810 nm. By placing this crystal at the center of the PSI, we have made the SPDC processes induced in clockwise and counterclockwise directions indistinguishable by the detectors. As a result, the setup produces a polarization-entangled two-photon state $|\Psi\rangle \sim |HV\rangle + e^{i\phi}|VH\rangle$, where ϕ is jointly determined by the initial polarization of the pump beam and the subsequent phase delays acquired within the PSI (*45*). In the experiment, we have set the tilting angle of QWP to target $\phi = \pi$ so that the resulting two-photon state is written as

$$|\Psi\rangle = \frac{1}{\sqrt{2}}(|HV\rangle - |VH\rangle) \tag{1}$$

The SPDC fields emitted into two distinct paths are each collimated by a lens with a focal length of $f_2 = 250$ mm. We denote the down-converted photons emitted into the upper path as *signal* while those emitted into the lower path as *idler*. Their joint polarization state is analyzed using a set of QWP, HWP, and PBS in each path. Note that we have chosen all waveplates in the setup to be zero-order (except for the dHWP inside the PSI) and have carefully aligned their optical axes before taking measurements. We use microscope objectives (OBJs) to couple down-converted photons into MMFs with core diameters of 200 μm and NAs of 0.39 (MMF-200-0.39) and detect them using avalanche photodiodes (APDs, PerkinElmer SPCM-CD 3017/Excelitas SPCM-QRH-14-FC).

We register the photon arrival time using a time-to-digital converter (TDC, qutool's quTAU) with a time resolution of $\tau = 81$ ps and extract the time correlation histograms between signal and idler photons. To characterize the resulting two-photon polarization state, we perform quantum state tomography (*46*) by recording coincidence rates at 16 different polarization projection bases and reconstruct the two-photon density matrix ρ, from which we can quantify the entanglement by calculating the concurrence $C(\rho)$ (*47*) and purity $P(\rho) = \mathrm{Tr}\{\rho^2\}$. We set an acquisition time of 2 min and a coincidence time window of 1 ns for each projective measurement. Due to solar irradiance variation throughout the daytime under realistic weather conditions, we observe differences in the sunlight pump power between measurements. Since the sunlight pump power measured at the power meter is well below 1 mW, we expect the SPDC to work in the low-gain regime where the pair generation rate scales linearly with the pump power. In subsequent data processing, we normalize the experimentally measured coincidence counts against the average pump power during data acquisition. The accidental coincidence rates are estimated using the average coincidence rates of photons arriving more than 5 ns apart.

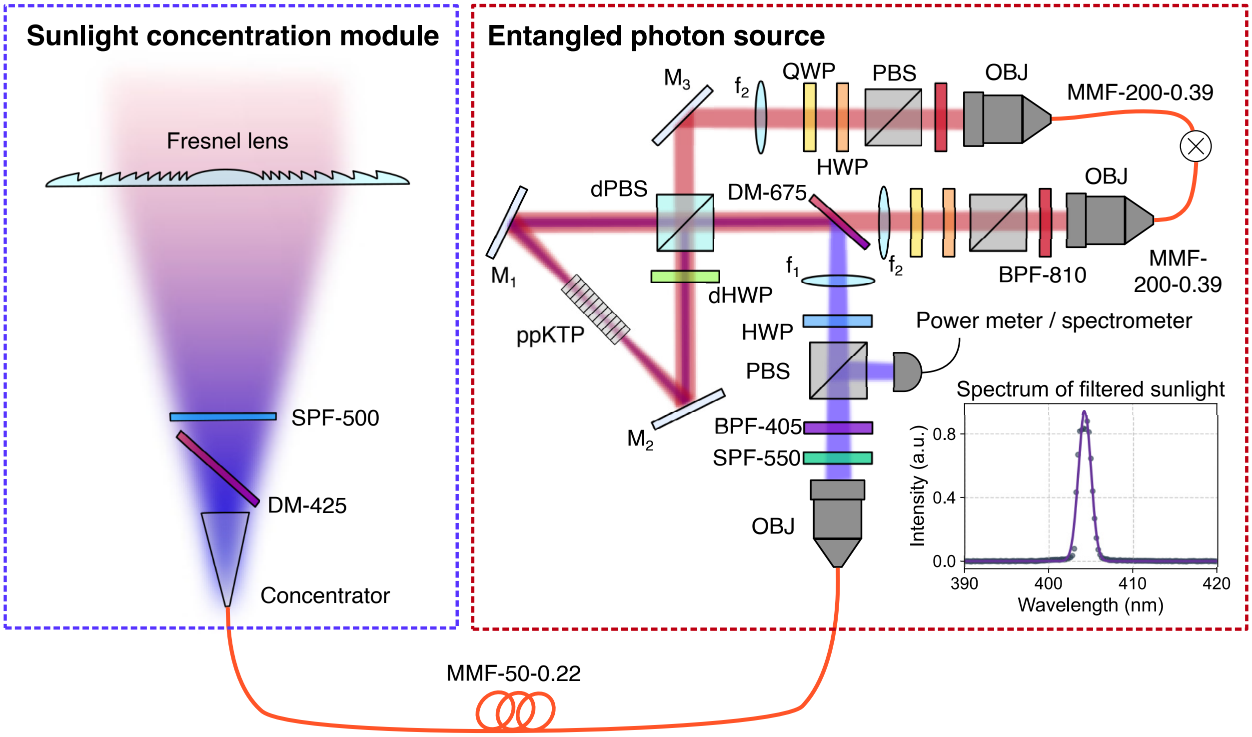

Figure 1: **Schematics of the experimental setup** The setup consists of a sunlight concentration module and an entangled-photon source. The sunlight concentration module collects direct sunlight via a 1 m × 1.4 m Fresnel lens and concentrates the spectrally filtered light into a multimode fiber (MMF). In the entangled-photon source, the sunlight is collimated and filtered to 405 nm ± 0.75 nm (inset) to pump a ppKTP crystal inside a PSI. We have carefully balanced the PSI to compensate for most spatial and temporal distinguishabilities between the SPDC processes in two directions. The resulting SPDC field is split and detected by MMF-coupled APDs to characterize two-photon entanglement and test for violation of local realism.

Results

Figure 2 displays the experimentally measured time correlation histogram between the SPDC photons measured on three separate days. We have set the waveplates in the detection paths to measure in the joint polarization bases VH and HV, respectively. We acquire data for 2 min per measurement and record the average pump power during the data acquisition. The time bin size is set to be twice the TDC's temporal resolution, $2\tau = 162$ ps. We observe photon coincidences centered around $\Delta t \sim 2.25$ ns. This time difference is caused by electronic delays between different channels of the TDC unit. At a 1 ns coincidence time window, we extract an average coincidence rate of 10 counts per minute per 100 nW of pump power, which is equivalent to a coincidence rate of $\sim 1600\ \mathrm{s}^{-1}$ (mW of pump power)$^{-1}$. This coincidence rate is consistent with the results obtained in an earlier work, in which a blue-light LED filtered to the same spatiotemporal bandwidth is employed as the pump source for SPDC and produces 100 counts per minute per 1 μW of pump power (*37*). We also note that, when this result is normalized against the effective bandwidth of the nonlinear interaction, the pair generation rate from incoherent-light-pumped SPDC is comparable to that of laser-pumped SPDC reported in (*37*). We also observe near-zero coincidence count rates at time differences far from the center of correlation, that is, $\Delta t > 5$ ns. Therefore, the experimentally measured coincidence counts contain negligible accidental coincidence counts. These results indicate a strong temporal correlation between the signal and idler photons, which is a feature of photon pair production from SPDC. Interestingly, an earlier study has observed spatial correlations between photon pairs produced from sunlight-pumped SPDC without studying entanglement (*54*). To observe photon entanglement beyond spatial and temporal correlations, it is necessary to reconstruct the density matrix of the quantum state and test for violations of Bell-type inequalities.

Figure 3 depicts the real and imaginary parts of the two-photon density matrix for sunlight-pumped SPDC. We obtain the depicted density matrix by averaging over the ones reconstructed from QST measurements conducted on three separate days. The resulting two-photon state has a concurrence of $C = 0.905 \pm 0.053$. Recall that the concurrence $C(\rho)$ is defined as an entanglement monotone that ranges from 0 to 1, where $C = 0$ represents complete absence of entanglement and $C = 1$ stands for maximal entanglement (*47*). Therefore, we have, for the first time, observed the

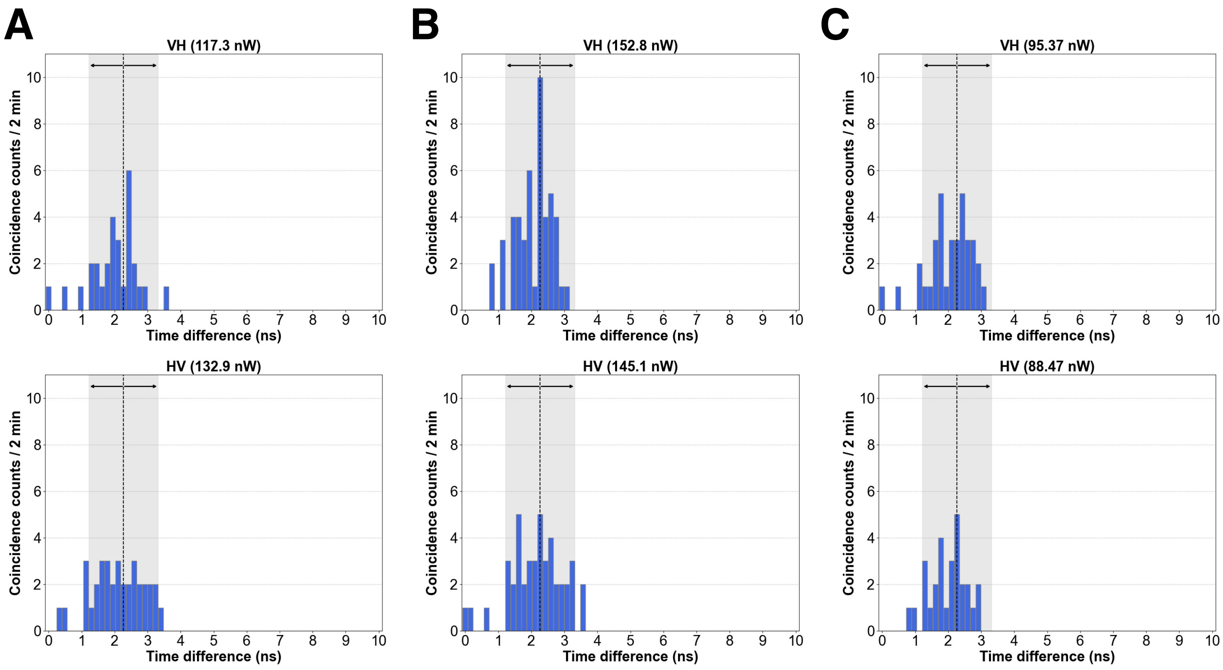

Figure 2: **Time-correlation histogram of sunlight-pumped SPDC measured in joint polarization bases VH and HV, respectively** In the titles of subplots, we note the average pump power measured over the time of data acquisition. (A-C) display results measured on three separate days. The bar plots display the experimentally measured photon coincidences, while the grey shade indicates the coincidence time window. The photon pairs show clear temporal correlation with negligible accidental coincidences.

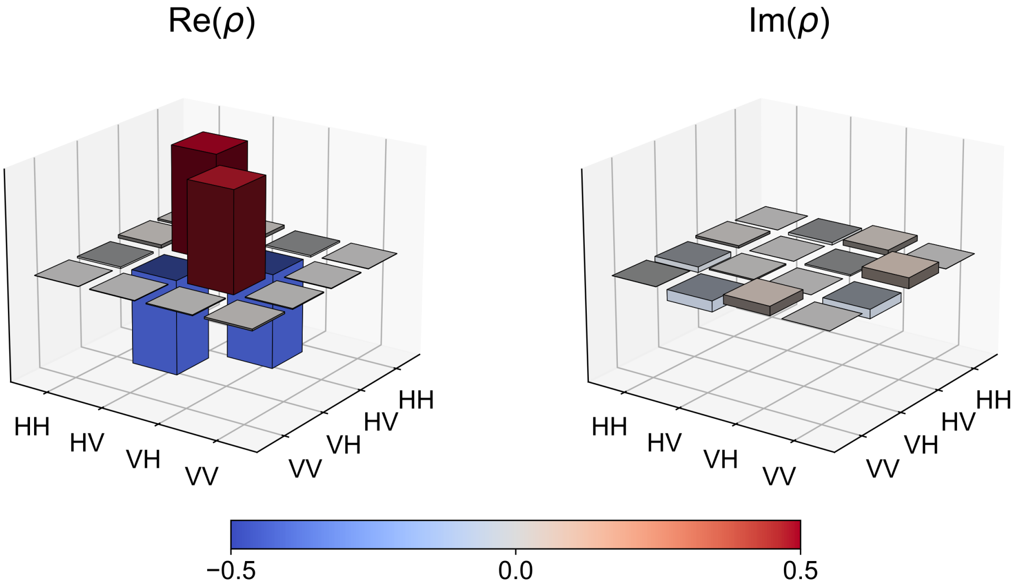

Figure 3: **Real and imaginary parts of the density matrix of the two-photon state produced from sunlight-pumped SPDC.** These results are calculated using quantum state tomography based on polarization correlation measurements in 16 different projection bases, which include those that have been displayed in Fig. 2. These results confirm polarization entanglement with a concurrence of $C = 0.905 \pm 0.053$, a purity of $P = 0.919 \pm 0.045$, and a fidelity of $F = 0.939 \pm 0.027$ to the target Bell state (Eqn. 1).

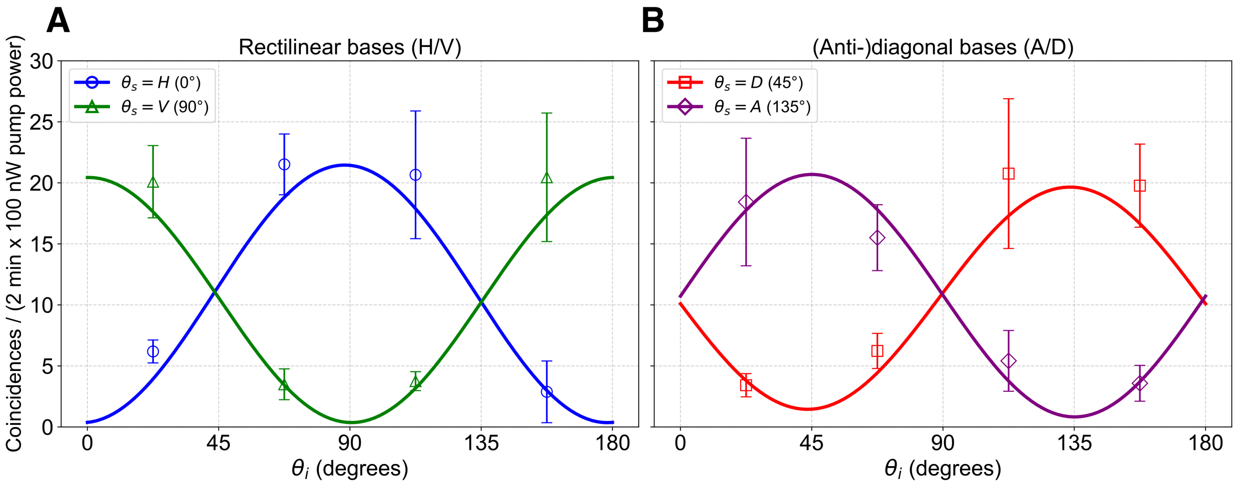

Figure 4: **Bell parameter measurement using the CHSH formalism.** Idler photons are projected into different linear polarizations while signal photons are projected into the **(A)** rectilinear bases and **(B)** (anti-)diagonal bases. We denote $\theta_{s(i)}$ as the angle of linear polarization with respect to the horizontal polarization, so that $\theta_s = 0°, 45°, 90°, 135°$ represents projecting signal photons in the horizontal (H), diagonal (D), vertical (V), and anti-diagonal (A) bases, respectively. These results lead to a violation of local realism with a Bell-CHSH parameter of $S = 2.5408 \pm 0.2171 > 2$.

generation of polarization-entangled photons from SPDC pumped by sunlight. To fully characterize the resulting state, we calculate the purity $P = \mathrm{tr}\{\rho^2\}$, where $\mathrm{tr}\{\cdots\}$ denotes the trace of a matrix, and the fidelity F, which quantifies the overlap between the generated state and the maximally entangled target state (Eqn. 1). As a result, we obtain $P = 0.919 \pm 0.045$ and $F = 0.939 \pm 0.027$. These already high values for the concurrence, purity, and fidelity indicate that the state is highly entangled, mostly pure (low noise), and close to the desired Bell state and are likely not limited in any fundamental way by the sunlight-pumped SPDC, but rather a consequence of optimizable technical parameters. Specifically, we believe that the spatial incoherence of the sunlight pump does not fundamentally degrade the entanglement quality in the polarization degree of freedom, and further improvements in entanglement quality can be achieved with an optimized setup design, such as using optical components with low wavefront distortions (*37, 55*).

While the tomography results quantify the quality of entanglement, verifying the non-classical nature of these correlations requires a test against local realism. Violation of local realism arguably distinguishes quantum systems from their classical counterparts (*48, 49, 56*) and could thus benchmark the performance of quantum systems for practical applications. For instance, observing violations of local realism certifies the security of quantum communication channels (*4, 5, 57*) and serves as a valuable resource for quantum-enhanced imaging and metrology (*58–60*). To demonstrate this capability with our sunlight-pumped entangled-photon source, we perform a Bell test using the CHSH formalism.

In Figure 4, we depict the experimentally measured photon coincidences for a Bell test in the CHSH formalism. To account for pump power fluctuations between different measurements, we have normalized the coincidence counts to a reference pump power of 100 nW before further data processing. The markers and error bars indicate the experimentally measured average coincidences and their standard deviations over measurements conducted on three separate days. We have used these data to calculate the Bell-CHSH parameter. The solid lines represent the expected polarization correlation curves, which are numerically calculated by projecting the resulting two-photon density matrix shown in Fig. 3 onto different joint polarization bases. The results of Bell test measurements agree well with those reconstructed from state tomography, indicating high consistency of the setup performance. We choose $\theta_s = 0°, \theta'_s = 45°, \theta_i = 22.5°, \theta'_i = 67.5°$ and calculate the CHSH parameter S from the coincidence rates using:

$$S = |E(\theta_s, \theta_i) - E(\theta_s, \theta'_i) + E(\theta'_s, \theta_i) + E(\theta'_s, \theta'_i)|, \tag{2}$$

and $E(\theta_s, \theta_i)$ is defined as

$$E(\theta_s, \theta_i) = \frac{N(\theta_s, \theta_i) + N(\theta_s^{\perp}, \theta_i^{\perp}) - N(\theta_s, \theta_i^{\perp}) - N(\theta_s^{\perp}, \theta_i)}{N(\theta_s, \theta_i) + N(\theta_s^{\perp}, \theta_i^{\perp}) + N(\theta_s, \theta_i^{\perp}) + N(\theta_s^{\perp}, \theta_i)}, \tag{3}$$

$$\theta^{\perp} = \theta + 90°, \tag{4}$$

where $\theta^{\perp}_{s(i)}$ stands for an angle perpendicular to $\theta_{s(i)}$. As a result, sunlight-pumped SPDC photons exhibit $S = 2.5408 \pm 0.2171 > 2$, thereby violating the CHSH inequality by 2.49 standard deviations.

Conclusions and perspectives

In summary, we have experimentally demonstrated the generation of polarization entanglement from SPDC pumped by sunlight. We observe a strong time correlation between photons produced from sunlight-pumped SPDC. Polarization correlations between the SPDC photons violate the

Bell-CHSH inequality with $S = 2.5408 \pm 0.2171$, which is larger than the local realistic threshold of 2, and thus confirms the non-classical nature of these correlated photons. Tomography analysis shows that the two-photon state produced from sunlight-pumped SPDC has a concurrence of $C = 0.905 \pm 0.053$, a purity of $P = 0.919 \pm 0.045$, and a fidelity of $F = 0.939 \pm 0.027$ to the target Bell state (Eq. 1), confirming, respectively, the generation of high polarization entanglement, with low decoherence and in the desired state from sunlight-pumped SPDC. These results mark the first demonstration of an entangled photon source operating without electrical energy input (except for temperature control on the nonlinear crystal to maintain phase-matching conditions), thus paving the way for energy-efficient and environmentally friendly quantum entangled sources. Furthermore, we emphasize that the quality of entanglement generated from sunlight-pumped SPDC, as quantified by its concurrence, purity, and fidelity to the target state, is on par with what has been reported in recent works employing laser-pumped SPDC (*50–53*), highlighting the application potential of sunlight-driven entangled-photon sources in photonic quantum technologies.

Having measured high entanglement for these sunlight-pumped SPDC photon pairs, as well as confirming that the correlations are fundamentally non-classical, we next consider what technical alterations would further improve these figures of merit.

One possible improvement would be to mitigate wavefront distortions in the optical components comprising the PSI. For instance, an uneven surface of the dPBS could introduce path distinguishability within the PSI and reduce the overall entanglement (*37, 45*). This wavefront distortion could be characterized and compensated for using adaptive optics methods. Alternatively, one can employ optical components custom-designed for low wavefront distortion. We believe these improvements can significantly enhance the quality of the resulting entanglement, yielding near-unity concurrence, purity, and fidelity to a maximally entangled state.

Another question is how to improve the photon pair production efficiency. We have shown here that sunlight-pumped SPDC produces photon pairs at a rate of $\sim 1600\ \mathrm{s}^{-1}$ (mW of pump power)$^{-1}$, which is the same efficiency observed with an LED of the same spectral profile (*37*), that is, 1.5 nm bandwidth centred around 405 nm. However, this is still somewhat less than the efficiency shown in the same setup for laser pumping ($\sim 7500\ \mathrm{s}^{-1}$ (mW of pump power)$^{-1}$). This discrepancy is likely due to the limited spectral phase-matching bandwidth of the nonlinear crystal (0.2-0.3 nm centred around 405 nm), which is much wider than the laser bandwidth, meaning that only a fraction of the power in the input sunlight participates in the SPDC and produces entangled photons. The spectral utilization efficiency can be improved by adopting type-0 phase-matching. In this experiment, we have chosen the MMF-50-0.22 to maximize the overlap between the transverse profile of the sunlight pump beam and that of the ppKTP crystal in the same plane. By adopting a nonlinear medium with larger transverse dimensions, the SPDC processes can potentially accommodate an increased amount of pump power distributed over a wider spatial spectrum.

Overall, we stress that entanglement quality and production efficiency are currently only limited by technical challenges and do not suggest a fundamental difference in the quality of an entangled photon source with an incoherent pump.

To further improve the overall brightness of entangled photon generation, one should refine the design of the solar concentration module for better sunlight collection efficiency. We identify several technical aspects to be improved in this avenue. Firstly, one can optimize the design of the conic concentrator so that its effective clear aperture and acceptance angle better match the focal parameters of the Fresnel lens at the desired spectral band. Wavelength-specific optical coatings could also be applied to the concentrator to minimize reflection and scattering losses. Secondly, one can adopt a motorized solar-tracking mount with finer angular resolution so that the overall coupling efficiency of sunlight into the MMF is less susceptible to motor inaccuracies and environmental disturbances. Thirdly, one can explore a filtering element engineered for high transmission at the pump wavelength to directly increase the usable optical flux. Although the commercial-grade color film employed in the current setup performs well at rejecting light at longer wavelengths, it also reflects a significant fraction of the light near 405 nm (see Supplementary Material), thereby reducing the available pump power. Finally, one can employ collection fibers with a larger core diameter. This would not only enhance the coupling efficiency of concentrated sunlight but, when paired with an appropriate lens imaging system, also deliver more overall pump power to a nonlinear crystal with larger transverse dimensions, thereby facilitating more effective utilization of the spatially diverse solar pump.

Although several opportunities for technical optimization have been identified, the highly entangled photons demonstrated in this proof-of-principle experiment already make a compelling case for replacing power-hungry, high-maintenance lasers with energy-efficient sources such as sunlight or LEDs. This technology offers strategic advantages, particularly for deploying quantum technologies in resource-restricted environments such as the Arctic or satellites in space (*18*).

Beyond logistical benefits, entangled photons generated from incoherent sources possess unique performance advantages. For instance, sunlight-pumped SPDC could take advantage of the broad spectral band of solar irradiance to facilitate access to entangled photons over a wider spectral range. Combined with the inherent low coherence between spectral components, these states may have optimized robustness against cross-talk between adjacent wavelength channels and thus offer a larger information capacity (*61*). Additionally, studies indicate that polarization-entangled photons pumped by spatially partially coherent light display stronger resilience to atmospheric turbulence, making them highly suitable for free-space quantum key distribution (*62–64*). Interestingly, recent findings show that four-wave mixing driven by amplified spontaneous emission can produce highly entangled states with higher generation rates than those driven by coherent emission (*65*). These findings not only challenge the conventional presumptions on the relations between coherence and entanglement but also present a new opportunity for boosting the energy efficiency and performance of current quantum information technologies.

References and Notes

1. R. P. Feynman, Simulating physics with computers. *International Journal of Theoretical Physics* **21** (6), 467–488 (1982), doi:10.1007/BF02650179, `https://doi.org/10.1007/BF02650179`.

2. P. Shor, Algorithms for quantum computation: discrete logarithms and factoring, in *Proceedings 35th Annual Symposium on Foundations of Computer Science* (1994), pp. 124–134, doi: 10.1109/SFCS.1994.365700.

3. G. D. Kahanamoku-Meyer, *et al.*, Classically verifiable quantum advantage from a computational Bell test. *Nature Physics* **18**, 918–924 (2022), doi:10.1038/s41567-022-01643-7.

4. C. H. Bennett, G. Brassard, Quantum cryptography: public key distribution and coin tossing, in *Proceedings of IEEE International Conference on Computers, Systems and Signal Processing* (IEEE, Bangalore, India) (1984), pp. 175–179.

5. A. K. Ekert, Quantum cryptography based on Bell's theorem. *Phys. Rev. Lett.* **67**, 661–663 (1991), doi:10.1103/PhysRevLett.67.661, `https://link.aps.org/doi/10.1103/PhysRevLett.67.661`.

6. C. Portmann, R. Renner, Security in quantum cryptography. *Reviews of Modern Physics* **94** (2), 025008 (2022), doi:10.1103/RevModPhys.94.025008.

7. V. Giovannetti, S. Lloyd, L. Maccone, Quantum-Enhanced Measurements: Beating the Standard Quantum Limit. *Science* **306** (5700), 1330–1336 (2004), doi:10.1126/science.1104149, `https://www.science.org/doi/abs/10.1126/science.1104149`.

8. C. L. Degen, F. Reinhard, P. Cappellaro, Quantum sensing. *Reviews of Modern Physics* **89** (3), 035002 (2017), doi:10.1103/RevModPhys.89.035002.

9. A. Auffèves, Quantum Technologies Need a Quantum Energy Initiative. *PRX Quantum* **3** (2), 020101 (2022), doi:10.1103/PRXQuantum.3.020101.

10. International Telecommunication Union, World Bank, Measuring the Emissions & Energy Footprint of the ICT Sector (2023), `https://www.itu.int/dms_pub/itu-d/opb/ind/d-ind-clim-2023-01-pdf-e.pdf`, provides data showing ICT sector emissions ~1.7–2.0%.

11. C. Freitag, *et al.*, The real climate and transformative impact of ICT. *Patterns* **2** (9), 100340 (2021), doi:10.1016/j.patter.2021.100340.

12. Oxford Instruments, *Principles of Dilution Refrigeration* (2015), `https://nanoscience.oxinst.com/assets/uploads/NanoScience/Brochures/Principles%20of%20dilution%20refrigeration_Sept15.pdf`, university of Oxford / Oxford Nanoscience brochure. States that a typical compressor for a ”dry” dilution refrigerator uses ~9 kW.

13. E. Parker, M. J. D. Vermeer, Estimating the Energy Requirements to Operate a Cryptanalytically Relevant Quantum Computer (2023), `https://arxiv.org/abs/2304.14344`.

14. D. Kielpinski, C. Monroe, D. J. Wineland, Architecture for a large-scale ion-trap quantum computer. *Nature* **417**, 709–711 (2002), doi:10.1038/nature00784.

15. T. Jennewein, C. Simon, G. Weihs, H. Weinfurter, A. Zeilinger, Quantum Cryptography with Entangled Photons. *Phys. Rev. Lett.* **84**, 4729–4732 (2000), doi:10.1103/PhysRevLett.84.4729, `https://link.aps.org/doi/10.1103/PhysRevLett.84.4729`.

16. R. Ursin, *et al.*, Entanglement-based quantum communication over 144 km. *Nature Physics* **3** (7), 481–486 (2007), doi:10.1038/nphys629, `https://doi.org/10.1038/nphys629`.

17. A. N. Black, *et al.*, Quantum Nonlocal Aberration Cancellation. *Phys. Rev. Lett.* **123**, 143603 (2019), doi:10.1103/PhysRevLett.123.143603, `https://link.aps.org/doi/10.1103/PhysRevLett.123.143603`.

18. J. Yin, *et al.*, Entanglement-based secure quantum cryptography over 1,120 kilometres. *Nature* **582** (7813), 501–505 (2020), doi:10.1038/s41586-020-2401-y, `https://doi.org/10.1038/s41586-020-2401-y`.

19. H. Defienne, B. Ndagano, A. Lyons, D. Faccio, Polarization entanglement-enabled quantum holography. *Nature Physics* **17** (5), 591–597 (2021), number: 5 Publisher: Nature Pub-

lishing Group, doi:10.1038/s41567-020-01156-1, `https://www.nature.com/articles/s41567-020-01156-1`.

20. P. Cameron, *et al.*, Adaptive optical imaging with entangled photons. *Science* **383**, 1142–1148 (2024), doi:10.1126/science.adk7825.

21. D. C. Burnham, D. L. Weinberg, Observation of Simultaneity in Parametric Production of Optical Photon Pairs. *Phys. Rev. Lett.* **25**, 84–87 (1970), doi:10.1103/PhysRevLett.25.84, `https://link.aps.org/doi/10.1103/PhysRevLett.25.84`.

22. C. K. Hong, L. Mandel, Theory of parametric frequency down conversion of light. *Phys. Rev. A* **31**, 2409–2418 (1985), doi:10.1103/PhysRevA.31.2409, `https://link.aps.org/doi/10.1103/PhysRevA.31.2409`.

23. R. W. Boyd, *Nonlinear Optics* (Academic Press, San Diego, CA) (2020).

24. A. K. Jha, R. W. Boyd, Spatial two-photon coherence of the entangled field produced by down-conversion using a partially spatially coherent pump beam. *Phys. Rev. A* **81**, 013828 (2010), doi:10.1103/PhysRevA.81.013828, `https://link.aps.org/doi/10.1103/PhysRevA.81.013828`.

25. E. Giese, R. Fickler, W. Zhang, L. Chen, R. W. Boyd, Influence of pump coherence on the quantum properties of spontaneous parametric down-conversion. *Physica Scripta* **93** (8), 084001 (2018).

26. C. H. Monken, P. H. S. Ribeiro, S. Pádua, Transfer of angular spectrum and image formation in spontaneous parametric down-conversion. *Phys. Rev. A* **57**, 3123–3126 (1998), doi:10.1103/PhysRevA.57.3123, `https://link.aps.org/doi/10.1103/PhysRevA.57.3123`.

27. H. Defienne, S. Gigan, Spatially entangled photon-pair generation using a partial spatially coherent pump beam. *Phys. Rev. A* **99**, 053831 (2019), doi:10.1103/PhysRevA.99.053831, `https://link.aps.org/doi/10.1103/PhysRevA.99.053831`.

28. W. Zhang, R. Fickler, E. Giese, L. Chen, R. W. Boyd, Influence of pump coherence on the generation of position-momentum entanglement in optical parametric down-conversion.

Opt. Express **27** (15), 20745–20753 (2019), doi:10.1364/OE.27.020745, `http://www.opticsexpress.org/abstract.cfm?URI=oe-27-15-20745`.

29. A. Burlakov, M. Chekhova, O. Karabutova, S. Kulik, Biphoton interference with a multimode pump. *Phys. Rev. A* **63** (5), 053801 (2001).
30. A. K. Jha, M. N. O'Sullivan, K. W. C. Chan, R. W. Boyd, Temporal coherence and indistinguishability in two-photon interference effects. *Phys. Rev. A* **77** (2), 021801 (2008).
31. G. Kulkarni, P. Kumar, A. K. Jha, Transfer of temporal coherence in parametric down-conversion. *J. Opt. Soc. Am. B* **34** (8), 1637–1643 (2017), doi:10.1364/JOSAB.34.001637, `http://josab.osa.org/abstract.cfm?URI=josab-34-8-1637`.
32. G. Kulkarni, V. Subrahmanyam, A. K. Jha, Intrinsic upper bound on two-qubit polarization entanglement predetermined by pump polarization correlations in parametric down-conversion. *Phys. Rev. A* **93**, 063842 (2016), doi:10.1103/PhysRevA.93.063842, `https://link.aps.org/doi/10.1103/PhysRevA.93.063842`.
33. N. Meher, A. S. M. Patoary, G. Kulkarni, A. K. Jha, Intrinsic degree of coherence of two-qubit states and measures of two-particle quantum correlations. *J. Opt. Soc. Am. B* **37** (4), 1224–1230 (2020), doi:10.1364/JOSAB.384936, `http://josab.osa.org/abstract.cfm?URI=josab-37-4-1224`.
34. L. Hutter, G. Lima, S. P. Walborn, Boosting Entanglement Generation in Down-Conversion with Incoherent Illumination. *Phys. Rev. Lett.* **125**, 193602 (2020), doi:10.1103/PhysRevLett.125.193602, `https://link.aps.org/doi/10.1103/PhysRevLett.125.193602`.
35. C. Li, B. Braverman, G. Kulkarni, R. W. Boyd, Experimental generation of polarization entanglement from spontaneous parametric down-conversion pumped by spatiotemporally highly incoherent light. *Phys. Rev. A* **107**, L041701 (2023), doi:10.1103/PhysRevA.107.L041701, `https://link.aps.org/doi/10.1103/PhysRevA.107.L041701`.
36. W. Zhang, D. Xu, L. Chen, Polarization Entanglement from Parametric Down-conversion with an LED Pump. *Phys. Rev. Appl.* **19**, 054079 (2023), doi:10.1103/PhysRevApplied.19.054079, `https://link.aps.org/doi/10.1103/PhysRevApplied.19.054079`.

37. C. Li, J. Upham, B. Braverman, R. W. Boyd, Violation of local realism with spatially multimode parametric down-conversion pumped by spatially incoherent light. *Phys. Rev. A* **112**, 053726 (2025), doi:10.1103/mxxf-ycdf, `https://link.aps.org/doi/10.1103/mxxf-ycdf`.

38. National Renewable Energy Laboratory, Best Research-Cell Efficiency Chart, `https://www.nrel.gov/pv/cell-efficiency` (2025), accessed: 2025-09-16.

39. M. Tian, *et al.*, A review on the recent research progress in the compound parabolic concentrator (CPC) for solar energy applications. *Renewable and Sustainable Energy Reviews* **82**, 4320–4337 (2018), doi:10.1016/j.rser.2017.11.031.

40. P. F. Holloway, L. B. Garrett, *Comparative analyses of space-to-space central power stations*, Technical report, NASA (1981).

41. Z. Kiss, H. Lewis, R. C. Duncan, Sun pumped continuous optical maser. *Applied Physics Letters* **2** (5), 93–94 (1963), doi:10.1063/1.1753762.

42. M. Küblböck, J. Will, H. Fattahi, Solar lasers: Why not? *APL Photonics* **9** (5), 050903 (2024), doi:10.1063/5.0209355.

43. P. E. Glaser, Method and Apparatus for Converting Solar Radiation to Electrical Power, U.S. Patent 3,781,647 (1973), `https://patents.google.com/patent/US3781647A/en`, filed by Arthur D. Little, Inc.

44. B. Agüera y Arcas, *et al.*, Towards a future space-based, highly scalable AI infrastructure system design. *arXiv preprint arXiv:2511.19468* (2025), doi:10.48550/arXiv.2511.19468, `https://arxiv.org/abs/2511.19468`.

45. T. Kim, M. Fiorentino, F. N. C. Wong, Phase-stable source of polarization-entangled photons using a polarization Sagnac interferometer. *Phys. Rev. A* **73**, 012316 (2006), doi:10.1103/PhysRevA.73.012316, `https://link.aps.org/doi/10.1103/PhysRevA.73.012316`.

46. D. F. V. James, P. G. Kwiat, W. J. Munro, A. G. White, Measurement of qubits. *Phys. Rev. A* **64**, 052312 (2001), doi:10.1103/PhysRevA.64.052312, `https://link.aps.org/doi/10.1103/PhysRevA.64.052312`.

47. W. K. Wootters, Entanglement of formation of an arbitrary state of two qubits. *Phys. Rev. Lett.* **80** (10), 2245 (1998).

48. J. S. Bell, On the Einstein Podolsky Rosen paradox. *Physics Physique Fizika* **1**, 195–200 (1964), doi:10.1103/PhysicsPhysiqueFizika.1.195, `https://link.aps.org/doi/10.1103/PhysicsPhysiqueFizika.1.195`.

49. J. F. Clauser, M. A. Horne, A. Shimony, R. A. Holt, Proposed Experiment to Test Local Hidden-Variable Theories. *Phys. Rev. Lett.* **23**, 880–884 (1969), doi:10.1103/PhysRevLett.23.880, `https://link.aps.org/doi/10.1103/PhysRevLett.23.880`.

50. A. Lohrmann, C. Perumangatt, A. Villar, A. Ling, Broadband pumped polarization entangled photon-pair source in a linear beam displacement interferometer. *Applied Physics Letters* **116** (2), 021101 (2020), doi:10.1063/1.5124416, `https://doi.org/10.1063/1.5124416`.

51. Y. S. Lee, M. Xie, R. Tannous, T. Jennewein, Sagnac-type entangled photon source using only conventional polarization optics. *Quantum Science and Technology* **6** (2), 025004 (2021), doi:10.1088/2058-9565/abd151, `https://doi.org/10.1088/2058-9565/abd151`.

52. E. Brambila, R. Gómez, R. Fazili, M. Gräfe, F. Steinlechner, Ultrabright polarization-entangled photon pair source for frequency-multiplexed quantum communication in free-space. *Opt. Express* **31** (10), 16107–16117 (2023), doi:10.1364/OE.461802, `https://opg.optica.org/oe/abstract.cfm?URI=oe-31-10-16107`.

53. K. Park, J. Lee, D.-G. Im, D. Kim, Y. S. Ihn, Ultrabright Fiber-Coupled Polarization-Entangled Photon Source with Spectral Brightness Surpassing 2.0MHz mW^{-1} nm^{-1}. *Advanced Photonics Research* **6** (10), 2500024 (2025), doi:https://doi.org/10.1002/adpr.202500024, `https://advanced.onlinelibrary.wiley.com/doi/abs/10.1002/adpr.202500024`.

54. Y. Xing, D. Xu, Y. Li, W. Zhang, L. Chen, Sunlight-Excited Spontaneous Parametric Down-Conversion for Quantum Imaging (2025), `https://arxiv.org/abs/2508.11207`.

55. C. Li, *et al.*, Rapid comprehensive characterization of biphoton spatial-polarization hyperentanglement (2025), `https://arxiv.org/abs/2502.03586`.

56. A. Einstein, B. Podolsky, N. Rosen, Can Quantum-Mechanical Description of Physical Reality Be Considered Complete? *Phys. Rev.* **47**, 777–780 (1935), doi:10.1103/PhysRev.47.777, `https://link.aps.org/doi/10.1103/PhysRev.47.777`.

57. D. Mayers, A. Yao, Quantum cryptography with imperfect apparatus, in *Proceedings of the 39th Annual Symposium on Foundations of Computer Science (FOCS)* (IEEE) (1998), pp. 503–509.

58. P.-A. Moreau, *et al.*, Imaging Bell-type nonlocal behavior. *Science Advances* **5** (7), eaaw2563 (2019), doi:10.1126/sciadv.aaw2563, `https://www.science.org/doi/abs/10.1126/sciadv.aaw2563`.

59. A. Niezgoda, J. Chwedeńczuk, Many-Body Nonlocality as a Resource for Quantum-Enhanced Metrology. *Phys. Rev. Lett.* **126**, 210506 (2021), doi:10.1103/PhysRevLett.126.210506, `https://link.aps.org/doi/10.1103/PhysRevLett.126.210506`.

60. B. Yadin, M. Fadel, M. Gessner, Metrological complementarity reveals the Einstein-Podolsky-Rosen paradox. *Nature Communications* **12** (1), 2410 (2021), doi:10.1038/s41467-021-22353-3, `https://doi.org/10.1038/s41467-021-22353-3`.

61. B. Dong, *et al.*, Partial coherence enhances parallelized photonic computing. *Nature* **632** (8023), 55–62 (2024), doi:10.1038/s41586-024-07590-y, `https://doi.org/10.1038/s41586-024-07590-y`.

62. A. Bhattacharjee, A. K. Jha, Experimental demonstration of structural robustness of spatially partially coherent fields in turbulence. *Opt. Lett.* **45** (14), 4068–4071 (2020), doi:10.1364/OL.395697, `http://opg.optica.org/ol/abstract.cfm?URI=ol-45-14-4068`.

63. Y. Qiu, W. She, The influence of atmospheric turbulence on partially coherent two-photon entangled field. *Applied Physics B* **108** (3), 683–687 (2012), doi:10.1007/s00340-012-5041-6, `https://doi.org/10.1007/s00340-012-5041-6`.

64. S. P. Phehlukwayo, M. L. Umuhire, Y. Ismail, S. Joshi, F. Petruccione, Influence of coincidence detection of a biphoton state through free-space atmospheric turbulence using a partially

spatially coherent pump. *Phys. Rev. A* **102**, 033732 (2020), doi:10.1103/PhysRevA.102.033732, `https://link.aps.org/doi/10.1103/PhysRevA.102.033732`.

65. Y.-W. Song, *et al.*, On-chip quantum states generation by incoherent light. *Nature Communications* **16** (1), 11429 (2025), doi:10.1038/s41467-025-66258-x, `https://doi.org/10.1038/s41467-025-66258-x`.

66. J. Brar, Towards Incoherent Quantum Down-Conversion Enabled by Optimized Solar Concentration, Bachelor's thesis, Friedrich-Alexander-Universität Erlangen-Nürnberg (2025), `https://open.fau.de/items/3503d7c8-f5be-4e9b-bb62-478261c6282e`, accessed: 2026-02-03.

67. M. Küblböck, M. Sahil, J. Brar, H. Fattahi, Solar-Pumped Laser Apparatus and Method of Generating Laser Radiation with the Solar-Pumped Laser Apparatus, European patent application (2025), patent application filed; not yet published.

Acknowledgments

The authors acknowledge useful discussions with Prof. Maria Chekhova and thank Prof. Jeff Lundeen, Dr. Manuel Francisco Ferrer García, Prof. Christoph Marquardt, Thomas Dirmeier and Dr. Yen-Ju Chen for access to key experimental equipment and software.

Funding: The portion of the work performed at the University of Ottawa was supported by the Canada Research Chairs program under Award 950-231657, the Natural Sciences and Engineering Research Council of Canada under Alliance Consortia Quantum Grant ALLRP 578468 - 22, Discovery Grant RGPIN/2017-06880, and the Canada First Research Excellence Fund Award 072623. The work performed at the Max Planck Institute for the Science of Light was supported by the Max Planck Society and a scholarship from Erlangen School in Advanced Optical Technologies. In addition, R.W.B. acknowledges support from the U.S. National Science Foundation Award No. 2138174 and the U.S. Department of Energy Award No. FWP 76295.

Author contributions: C.L., J.U., H.F., and R.W.B. conceived the research idea. J.B. and M.K. designed and built the solar concentration module. C.L. built the entangled-photon source. C.L. and J.B. conducted outdoor experiments with M.K.'s help to measure sunlight-driven entangled photon generation. C.L., J.B., J.U., and H.F. analyzed the data. C.L. and J.B. wrote the first draft of the paper, and all authors subsequently contributed to the writing. H.F. and R.W.B. supervised the project.

Competing interests: There are no competing interests to declare.

Data and materials availability: All data required to reproduce the results shown in Fig. 2-4 are available at Dryad via: `http://datadryad.org/share/LINK_NOT_FOR_PUBLICATION/NtVTjAjs5S8-U0Hn-oFiItMRjmpGNZtnJReX-s6ZFsU`

Supplementary materials

Materials and Methods

Figs. S1 to S4

References *(62-67)*

Supplementary Materials for

Generating quantum entanglement from sunlight

Cheng Li[1†], Jasvinder Brar[2,3†], Michael Küblböck[2,3],
Jeremy Upham[1], Hanieh Fattahi[2,3*], Robert W. Boyd[1,4*]
[1]Department of Physics, University of Ottawa, Ottawa, Ontario, Canada K1N 6N5.
[2]Max Planck Institute for the Science of Light, Erlangen, Germany.
[3]Friedrich-Alexander-Universität Erlangen-Nürnberg, Erlangen, Germany.
[4]Institute of Optics, University of Rochester, Rochester, New York 14627, USA.
[*]Corresponding authors. Emails: hanieh.fattahi@mpl.mpg.de; rboyd@uottawa.ca
[†]These authors contributed equally to this work.

This PDF file includes:

Materials and Methods

Figures S1 to S2

References *(62-67)*

Materials and Methods

Outdoor experimental setup

Fig. S1 depicts the actual experimental setup, which is deployed in an enclosed outdoor space at the Max Planck Institute for the Science of Light in Erlangen, Germany. To minimize the influence of wind, the experimental area is surrounded by protective fencing. The full setup for generating entangled photons, together with the APDs, TDC, and the temperature control unit of the ppKTP crystal, is placed inside a tent. This outer enclosure provides a darkroom-like environment that facilitates onsite troubleshooting of optical alignment for a setup placed outside a traditional laboratory. Within this tent, the entangled-photon source setup is enclosed in a light-tight housing that prevents any residual external light from entering the system. The APDs are mounted inside this inner enclosure to minimize the detection of background illumination and accidental coincidences. The pre-filtered and concentrated sunlight is guided to the entangled-photon source through a five-meter MMF with a core diameter of 50 μm and a numerical aperture (NA) of 0.22 (MMF-50-0.22). One end of this fibre is butt-coupled to the sunlight concentration module, while the other end is routed through a small opening at the bottom of the tent, and connected to the OBJ (with 20× magnification and 0.4 NA) that couples the light into the free-space entanglement setup.

Sunlight concentration system

Fig. S2 displays the design and performance of the sunlight concentration module used for solar pumping. Fig. S2(A) shows a photograph of the actual sunlight concentration setup. Incident sunlight is collected by a 1 m × 1.4 m PMMA Fresnel lens serving as the primary concentrator, focusing the light to a focal spot of 13 mm in diameter at a focal length of 90 cm. To reduce the contribution of long-wavelength spectral components, the Fresnel lens is covered with commercial-grade colour filters (Roscolux). The lens, clamped between two arms of a supporting frame, is mounted on a high-precision equatorial mount (Celestron CGE Pro). Following polar alignment to the celestial north pole, the Sun's position is calculated using software integrated into the mount, which automatically slews the system to the solar position and provides continuous motor-driven tracking. The mount achieves a tracking accuracy of approximately 9 arcseconds, ensuring stable alignment of the Fresnel lens with the sun throughout the measurement period. Residual tracking errors and environmental perturbations nevertheless introduce slow fluctuations in the focal-spot position at the secondary optics, which limit the overall coupling efficiency into the subsequent concentrator and fiber. Employing a motorized solar-tracking mount with finer angular resolution would reduce sensitivity to such effects and improve long-term coupling stability, allowing increased acquisition times (currently on the order of 2 min per measurement).

After being pre-filtered by the films on the Fresnel lens, the sunlight then propagates through additional secondary filters located at the focal plane of the Fresnel lens. This secondary concentration module is protected by a copper shielding structure with a circular aperture that is concentrically aligned with subsequent optical components. We have designed this copper shield to maximize sunlight throughput while effectively protecting the subsequent optical elements from being heated up by stray radiation. The beam first passes through a short-pass filter with a cut-off wavelength of 500 nm (SPF-500, Edmund optics, 84-719), and subsequently through a dichroic mirror transmitting wavelengths shorter than 425 nm and reflecting longer wavelengths (DM-425, Thorlabs DMLP425L) at a 45° angle of incidence. Fine adjustment of the dichroic mirror angle with respect to the optical axis is used to maximize transmission at 405 nm. Through this multi-stage filtering process, the solar spectrum is progressively narrowed to the ultraviolet–blue wavelength range, selectively retaining the target pump wavelength of 405 nm.

Fig. S2(C) depicts the experimentally measured transmission spectra after each stage of filtering, with the solar spectrum serving as a reference. The inset shows an enlarged view of the transmission behaviour around 405 nm. These are normalized and scaled to the respective full-spectrum power. As shown, the initially broadband solar spectrum is progressively attenuated at each filtering stage, i.e. the Fresnel lens, the SPF-500 and the DM-425, resulting in a corresponding reduction of the transmitted power.

In order to efficiently couple the light focused and filtered by the Fresnel lens and secondary filters into a multimode fiber with a core diameter of 50 μm and a numerical aperture of 0.22 (MMF-0.5-0.22), a custom-made conical concentrator is used (*66*). Its shape and geometry are shown in Fig. S2(B), along with a plot highlighting the relevant geometric and optical optimization parameters. The solid cylindrically symmetric conical concentrator is fabricated from fused silica. It has an overall length of 69 mm, an entrance aperture diameter of 23 mm and an exit aperture diameter of 1.5 mm. Light entering the wide aperture is guided toward the narrow output by refractive guiding and total internal reflection at the silica–air interface, resulting from the tapered geometry. This design enables efficient concentration of incident solar radiation onto a small area while maintaining high optical transmission and thermal stability. Experimentally, a concentration efficiency η of approximately 30 ± 3% is obtained. This efficiency is defined as the ratio of the output power measured at the smaller end of the cone to the input power at the wider end. Importantly, the existing conical concentrator was originally designed to maximize collection efficiency across a broad visible spectral range, rather than being optimized specifically for narrowband collection at 405 nm. As a result, additional improvements in the usable 405 nm throughput are expected through the application of wavelength-specific anti-reflection coatings, refinement of the acceptance angle to better match the focused solar cone, and optimization of the entrance aperture relative to the Fresnel-lens focal spot (*66, 67*).

Ray tracing simulations indicate that, with the appropriate choice of glass material and further geometric and optical optimizations, this concentrator can achieve concentration efficiencies of up to 67% (*66*). The plot in Fig. S2(C) compares the maximum concentration efficiencies obtained for four different glass materials at their respective optimal opening angles, denoted as θ_{opt}, which correspond to the opening angles yielding the highest efficiency. We define the opening angle θ as the half-angle between the cone axis and the tapered sidewall of the concentrator, thereby directly describing the degree of tapering of the conical geometry. In contrast to fused silica ($n_{405} = 1.464$) used in the experiment, simulations for N-BK7 ($n_{405} = 1.527$), N-SF10 ($n_{405} = 1.776$), and LASF35 ($n_{405} = 2.087$) predict increasing efficiencies of 49 %, 58 %, and 67 %, respectively, all within a common optimal opening-angle range of $8.2^\circ - 8.7^\circ$. These results demonstrate a clear trend of increasing concentration efficiency with higher refractive index, accompanied by a convergence of the optimal opening angle toward smaller values for higher-index glasses.

Based on the latitude of Erlangen (49.6° N) and season of measurement, the maximum solar power collectable by the 1.4 m^2 Fresnel lens is approximately 1.1–1.2 kW, of which we estimate that approximately 1.7 W of this power lies within the 405 ± 0.75 nm spectral band. Due to the combined effect of spectral filtering and the light-concentrating properties of the cone, the full-spectrum optical power available at the tip of the conic concentrator can reach up to 5 W under near-perfect conditions. After coupling into the MMF, the entangled-photon source receives an optical power of 100–200 nW within a 1.5-nm bandwidth around the center wavelength of 405 nm.

As discussed in the main text, this overall sunlight utilization efficiency into the setup is constrained by the spatial and spectral bandwidth of the nonlinear conversion process and can be further improved by optimizing the crystal geometry and choosing a broadband phase-matching condition. Additionally, the coupled sunlight power is significantly influenced by the weather conditions at the time of measurement and by the time of day. Fig. S2(D) shows an example of the diurnal variation of the pump power measured on 18 September 2025. The pump power increases from the morning hours to a maximum around solar noon before decreasing again toward the late afternoon. On the measurement days corresponding to the data presented in this paper, pump powers of up to 195 nW were achieved. Although sufficient pump power is available throughout the day to obtain meaningful statistics for sunlight-driven entangled-photon generation, measurements performed near solar noon yield higher count rates and reduced statistical uncertainties.

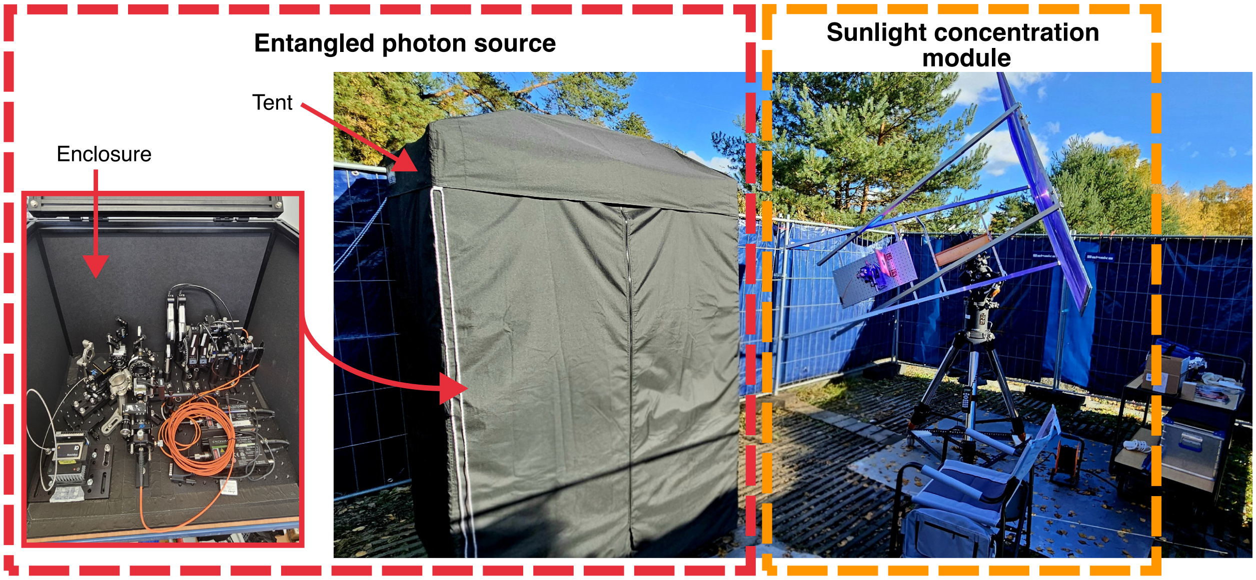

Figure S1: **Real-life photographs of experimental setups used for the sunlight-pumped generation of polarization-entangled photon pairs** The entire setup consists of two components: a sunlight concentration module (right) and an entangled-photon source (left) housed inside a protective and darkening tent, which also contains the associated electronics. Inset: Optical setup of the entangled-photon source, showing the optical arrangement and avalanche photodiodes (APDs) used for photon-pair generation. A hinged door (not shown) is also installed as part of the enclosure, which, when closed, covers the front and top sides of the optical setup.

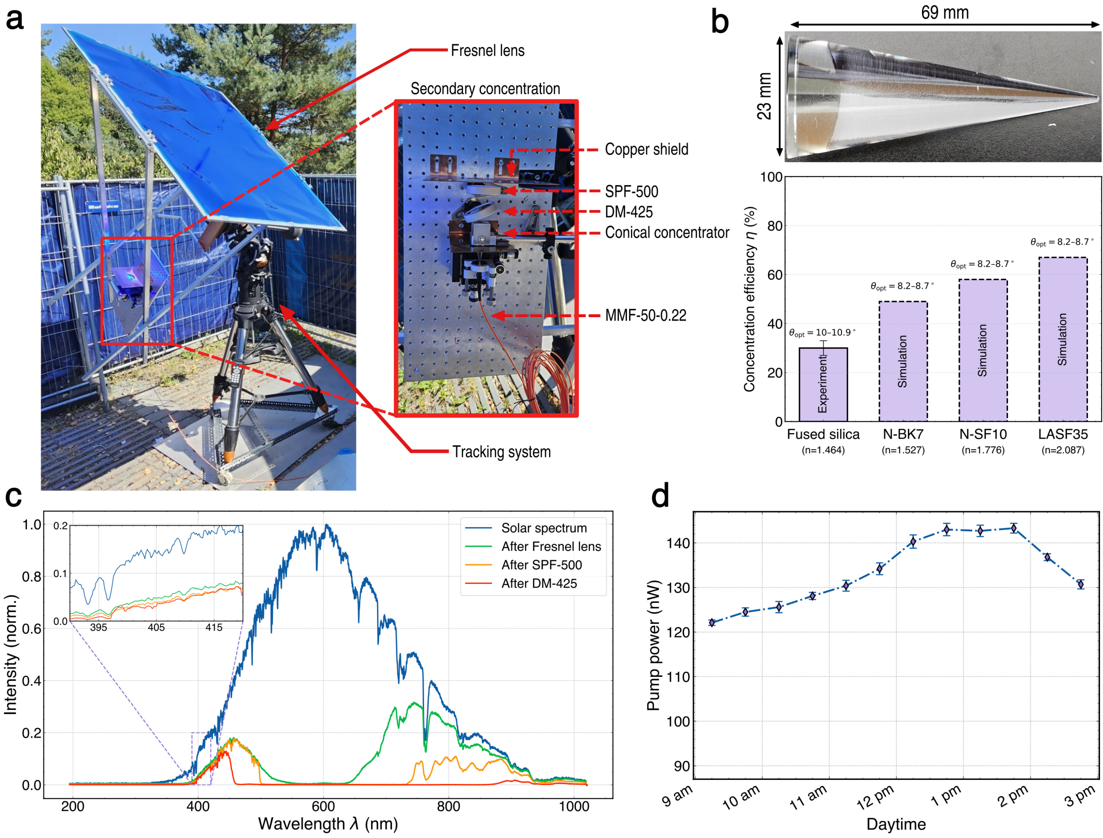

Figure S2: **Detailed schematics of the sunlight concentration module and its performance** (**A**) Real-life photograph of the outdoor solar concentration setup showing the Fresnel lens serving as the primary concentrator, mounted on a dual-axis tracking system, together with the secondary concentration module. Inset: secondary concentration module. (**B**) Geometry and dimensions together with a plot indicating the optimization parameters of the custom-designed conical concentrator used to efficiently couple concentrated sunlight into the multimode fibre. (**C**) Experimentally measured spectra at successive stages of the solar concentration, illustrating the gradual spectral filtering of sunlight. They are normalised and scaled to the respective measured power, summed over the entire spectrum. Inset: spectrum around target pumping wavelength 405 nm (**D**). Diurnal variation of the pump power over the course of the day under clear-sky conditions, showing a maximum near solar noon. The data were recorded on 18 September 2025. SPF-500: short-pass filter with a cut-off wavelength of 500 nm; DM-425: dichroic mirror transmitting wavelengths shorter than 425 nm and reflecting longer wavelengths; MMF-50-0.22: multimode fiber with a core diameter of 50 μm and a numerical aperture of 0.22.

Chapter 6

Conclusion and Future Works

In this thesis, we have addressed a crucial issue in the field of nonlinear quantum optics, that is, the fundamental necessity of classical optical coherence in the generation of quantum photon entanglement through nonlinear optical conversions. Specifically, we have demonstrated the generation of two-photon entanglement using SPDC pumped by incoherent light sources. Furthermore, we have attributed the minor influence of the pump beam's spatial coherence on the two-photon polarization state generated by SPDC to spatial-polarization coupling introduced by technical aspects of the experimental setup. Critically, unlike the case in which the pump beam and the SPDC field are considered in the same DoF, the cross-influence between different DoFs is not a fundamental effect in SPDC. Consequently, by optimizing the experimental setup, one can achieve high polarization entanglement from SPDC pumped by spatially incoherent light sources, such as LEDs and sunlight. These results demonstrate novel approaches to SPDC-based entanglement generation, opening the way for photonic quantum technologies driven by ubiquitous, energy-efficient light sources. Moving forward, this thesis could inform future studies in several important aspects of photonic quantum science and technologies.

From a fundamental perspective, the study of the influence of pump coherence on the two-photon entanglement is not yet exhaustive. While the present study confirms that the pump's spatial coherence does not influence the polarization entanglement generated by SPDC, the potential cross-influence from other DoFs requires further experimental examination. For instance, one can study the influence of the pump's spatial coherence on time-energy entanglement generated from SPDC, or vice versa. Combined with the results presented in this thesis, demonstrating the generation of time-energy entanglement from SPDC pumped by spatially incoherent light would also imply the possibility of generating time-energy-polarization hyperentangled states, which have important implications in photonic quantum technologies [57, 58, 59].

The application potential of incoherent-light-driven entangled photon sources also remains underexplored. In the context of free-space quantum communication, SPDC pumped by spatially incoherent light is shown to be more robust against atmospheric turbulence than that pumped by highly coherent lasers [60, 61, 62]. Therefore, it would be useful to investigate quantum key distribution using two-photon polarization entanglement generated from incoherent-light-driven SPDC. In classical photonic computing, a recent study has shown that decreased temporal coherence can reduce cross-talk between different wavelength channels, thereby optimizing the bandwidth use in the photonic convolutional processing. Furthermore, since classical low-coherence light sources are known to reduce speckle noise and improve image quality compared to their coherent counterparts [63, 64], the implications of using incoherent-light-driven SPDC for quantum-enhanced imaging and sensing may also warrant investigation.

On the other hand, cross-influence between different DoFs could inform the controlled generation of hybrid entanglement between them, whose topological features can be exploited to enable novel information processing protocols. While existing literature routinely introduces these cross-DoF couplings by structuring a postselected subset of the SPDC field, one can also pre-modulate the desired structures in the pump beam so that they are directly generated in the resulting SPDC fields [65]. Alternatively, it would be valuable to explore the domain-engineering of a nonlinear crystal that embeds the desired cross-DoF coupling into the phase-matching functions of the nonlinear conversion processes[66].

Another important nonlinear optical effect used for entangled photon generation is FWM. As a third-order nonlinear effect, FWM is often considered to have much lower nonlinear conversion efficiency than its second-order counterparts. However, recent research in epsilon-near-zero (ENZ) materials offers a promising approach to significantly enhancing the third-order nonlinearity in practical photonic devices [67, 68]. Importantly, in 2024, Lim et al. [69] experimentally demonstrated high-efficiency degenerate FWM using ENZ-based cavity devices, reporting an absolute efficiency of up to 34%. Moreover, a recent study showed that polarization-entangled two-photon states can be generated via on-chip FWM processes driven by temporally incoherent light, namely the amplified spontaneous emission from an erbium-doped fiber amplifier [70]. Interestingly, the photon pair generation efficiency of incoherent-light-driven FWM appears higher than that of the coherent-light-driven FWM. Taken together, we believe that incoherence, which was long viewed as a limitation in photonic and quantum systems, can instead be leveraged as a viable resource for scalable, energy efficient, and robust photonic quantum technologies, potentially reshaping both the conceptual and practical landscape of nonlinear quantum optics.

Bibliography

[1] Ryszard Horodecki, Paweł Horodecki, Michał Horodecki, and Karol Horodecki. Quantum entanglement. *Rev. Mod. Phys.*, 81:865–942, Jun 2009.

[2] David Deutsch and Artur Ekert. Quantum computation. *Physics World*, 11(3):47, mar 1998.

[3] Robert Raussendorf and Hans J. Briegel. A one-way quantum computer. *Phys. Rev. Lett.*, 86:5188–5191, May 2001.

[4] Charles H. Bennett and Gilles Brassard. Quantum cryptography: public key distribution and coin tossing. In *Proceedings of IEEE International Conference on Computers, Systems and Signal Processing*, pages 175–179, Bangalore, India, 1984. IEEE.

[5] Artur K. Ekert. Quantum cryptography based on Bell's theorem. *Phys. Rev. Lett.*, 67:661–663, Aug 1991.

[6] Vittorio Giovannetti, Seth Lloyd, and Lorenzo Maccone. Quantum-enhanced measurements: Beating the standard quantum limit. *Science*, 306(5700):1330–1336, 2004.

[7] John Clarke and Frank K. Wilhelm. Superconducting quantum bits. *Nature*, 453(7198):1031–1042, Jun 2008.

[8] Markus Ansmann, H. Wang, Radoslaw C. Bialczak, Max Hofheinz, Erik Lucero, M. Neeley, A. D. O'Connell, D. Sank, M. Weides, J. Wenner, A. N. Cleland, and John M. Martinis. Violation of Bell's inequality in josephson phase qubits. *Nature*, 461(7263):504–506, Sep 2009.

[9] D. L. Moehring, P. Maunz, S. Olmschenk, K. C. Younge, D. N. Matsukevich, L.-M. Duan, and C. Monroe. Entanglement of single-atom quantum bits at a distance. *Nature*, 449(7158):68–71, Sep 2007.

[10] Guido Burkard, Thaddeus D. Ladd, Andrew Pan, John M. Nichol, and Jason R. Petta. Semiconductor spin qubits. *Rev. Mod. Phys.*, 95:025003, Jun 2023.

[11] D. M. Zajac, A. J. Sigillito, M. Russ, F. Borjans, J. M. Taylor, G. Burkard, and J. R. Petta. Resonantly driven CNOT gate for electron spins. *Science*, 359(6374):439–442, 2018.

[12] Stuart J. Freedman and John F. Clauser. Experimental test of local hidden-variable theories. *Phys. Rev. Lett.*, 28:938–941, Apr 1972.

[13] Alain Aspect, Philippe Grangier, and Gérard Roger. Experimental tests of realistic local theories via Bell's theorem. *Phys. Rev. Lett.*, 47:460–463, Aug 1981.

[14] Jeremy L. O'Brien, Akira Furusawa, and Jelena Vučković. Photonic quantum technologies. *Nature Photonics*, 3(12):687–695, Dec 2009.

[15] Sergei Slussarenko and Geoff J. Pryde. Photonic quantum information processing: A concise review. *Applied Physics Reviews*, 6(4):041303, 10 2019.

[16] S. E. Harris, M. K. Oshman, and R. L. Byer. Observation of tunable optical parametric fluorescence. *Phys. Rev. Lett.*, 18:732–734, May 1967.

[17] David C. Burnham and Donald L. Weinberg. Observation of simultaneity in parametric production of optical photon pairs. *Phys. Rev. Lett.*, 25:84–87, Jul 1970.

[18] Y. H. Shih and C. O. Alley. New type of Einstein-Podolsky-Rosen-Bohm experiment using pairs of light quanta produced by optical parametric down conversion. *Phys. Rev. Lett.*, 61:2921–2924, Dec 1988.

[19] Jay E. Sharping, Marco Fiorentino, and Prem Kumar. Observation of twin-beam-type quantum correlation in optical fiber. *Opt. Lett.*, 26(6):367–369, Mar 2001.

[20] Hiroki Takesue and Kyo Inoue. Generation of polarization-entangled photon pairs and violation of Bell's inequality using spontaneous four-wave mixing in a fiber loop. *Phys. Rev. A*, 70:031802, Sep 2004.

[21] Anand Kumar Jha. *Coherence properties of the entangled two-photon field produced by parametric down-conversion.* PhD thesis, University of Rochester, 2009.

[22] Leonard Mandel and Emil Wolf. *Optical Coherence and Quantum Optics.* Cambridge University Press, 1995.

[23] Juan Yin, Yu-Huai Li, Sheng-Kai Liao, Meng Yang, Yuan Cao, Liang Zhang, Ji-Gang Ren, Wen-Qi Cai, Wei-Yue Liu, Shuang-Lin Li, Rong Shu, Yong-Mei Huang, Lei Deng, Li Li, Qiang Zhang, Nai-Le Liu, Yu-Ao Chen, Chao-Yang Lu, Xiang-Bin Wang, Feihu Xu, Jian-Yu Wang, Cheng-Zhi Peng, Artur K. Ekert, and Jian-Wei Pan. Entanglement-based secure quantum cryptography over 1,120 kilometres. *Nature*, 582(7813):501–505, Jun 2020.

[24] Marco Lanzagorta. Quantum imaging for underwater arctic navigation. In Kenneth I. Ranney and Armin Doerry, editors, *Radar Sensor Technology XXI*, volume 10188, page 101880G. International Society for Optics and Photonics, SPIE, 2017.

[25] Joachim Piprek. Comparative efficiency analysis of gan-based light-emitting diodes and laser diodes. *Applied Physics Letters*, 109(2):021104, 07 2016.

[26] International Telecommunication Union and World Bank. Measuring the emissions & energy footprint of the ICT sector, 2023.

[27] Charlotte Freitag, Mike Berners-Lee, Kelly Widdicks, Bran Knowles, Gordon Blair, and Adrian Friday. The real climate and transformative impact of ICT. *Patterns*, 2(9):100340, 2021.

[28] Anand Kumar Jha and Robert W. Boyd. Spatial two-photon coherence of the entangled field produced by down-conversion using a partially spatially coherent pump beam. *Phys. Rev. A*, 81:013828, Jan 2010.

[29] Enno Giese, Robert Fickler, Wuhong Zhang, Lixiang Chen, and Robert W Boyd. Influence of pump coherence on the quantum properties of spontaneous parametric down-conversion. *Physica Scripta*, 93(8):084001, 2018.

[30] C. H. Monken, P. H. Souto Ribeiro, and S. Pádua. Transfer of angular spectrum and image formation in spontaneous parametric down-conversion. *Phys. Rev. A*, 57:3123–3126, Apr 1998.

[31] Hugo Defienne and Sylvain Gigan. Spatially entangled photon-pair generation using a partial spatially coherent pump beam. *Phys. Rev. A*, 99:053831, May 2019.

[32] Wuhong Zhang, Robert Fickler, Enno Giese, Lixiang Chen, and Robert W. Boyd. Influence of pump coherence on the generation of position-momentum entanglement in optical parametric down-conversion. *Opt. Express*, 27(15):20745–20753, Jul 2019.

[33] AV Burlakov, MV Chekhova, OA Karabutova, and SP Kulik. Biphoton interference with a multimode pump. *Phys. Rev. A*, 63(5):053801, 2001.

[34] Anand Kumar Jha, Malcolm N O'Sullivan, Kam Wai Clifford Chan, and Robert W Boyd. Temporal coherence and indistinguishability in two-photon interference effects. *Phys. Rev. A*, 77(2):021801, 2008.

[35] Girish Kulkarni, Prashant Kumar, and Anand K. Jha. Transfer of temporal coherence in parametric down-conversion. *J. Opt. Soc. Am. B*, 34(8):1637–1643, Aug 2017.

[36] Girish Kulkarni, V. Subrahmanyam, and Anand K. Jha. Intrinsic upper bound on two-qubit polarization entanglement predetermined by pump polarization correlations in parametric down-conversion. *Phys. Rev. A*, 93:063842, Jun 2016.

[37] Nilakantha Meher, Abu Saleh Musa Patoary, Girish Kulkarni, and Anand K. Jha. Intrinsic degree of coherence of two-qubit states and measures of two-particle quantum correlations. *J. Opt. Soc. Am. B*, 37(4):1224–1230, Apr 2020.

[38] A. Einstein, B. Podolsky, and N. Rosen. Can quantum-mechanical description of physical reality be considered complete? *Phys. Rev.*, 47:777–780, May 1935.

[39] E. Schrödinger. Discussion of probability relations between separated systems. *Mathematical Proceedings of the Cambridge Philosophical Society*, 31(4):555–563, 1935.

[40] J. S. Bell. On the Einstein Podolsky Rosen paradox. *Physics Physique Fizika*, 1:195–200, Nov 1964.

[41] John F. Clauser, Michael A. Horne, Abner Shimony, and Richard A. Holt. Proposed experiment to test local hidden-variable theories. *Phys. Rev. Lett.*, 23:880–884, Oct 1969.

[42] B. S. Cirel'son. Quantum generalizations of Bell's inequality. *Letters in Mathematical Physics*, 4(2):93–100, Mar 1980.

[43] Reinhard F. Werner. Quantum states with Einstein-Podolsky-Rosen correlations admitting a hidden-variable model. *Phys. Rev. A*, 40:4277–4281, Oct 1989.

[44] William K Wootters. Entanglement of formation of an arbitrary state of two qubits. *Phys. Rev. Lett.*, 80(10):2245, 1998.

[45] L. E. Myers, R. C. Eckardt, M. M. Fejer, R. L. Byer, W. R. Bosenberg, and J. W. Pierce. Quasi-phase-matched optical parametric oscillators in bulk periodically poled $LiNbO_3$. *J. Opt. Soc. Am. B*, 12(11):2102–2116, Nov 1995.

[46] Robert W Boyd. *Nonlinear Optics.* Academic Press, San Diego, CA, 2020.

[47] Girish Kulkarni, Jeremy Rioux, Boris Braverman, Maria V. Chekhova, and Robert W. Boyd. Classical model of spontaneous parametric down-conversion. *Phys. Rev. Res.*, 4:033098, Aug 2022.

[48] Suman Karan, Shaurya Aarav, Homanga Bharadhwaj, Lavanya Taneja, Arinjoy De, Girish Kulkarni, Nilakantha Meher, and Anand K Jha. Phase matching in β-barium borate crystals for spontaneous parametric down-conversion. *Journal of Optics*, 22(8):083501, jun 2020.

[49] Asma Al-Qasimi, Olga Korotkova, Daniel James, and Emil Wolf. Definitions of the degree of polarization of a light beam. *Opt. Lett.*, 32(9):1015–1016, May 2007.

[50] G. Tamošauskas, J. Galinis, A. Dubietis, and A. Piskarskas. Observation of spontaneous parametric down-conversion excited by high brightness blue LED. *Optics Express*, 18(5):4310–4315, 2010.

[51] Justinas Galinis, Michał Karpiński, Gintaras Tamošauskas, Krzysztof Dobek, and Algis Piskarskas. Photon coincidences in spontaneous parametric down-converted radiation excited by a blue LED in bulk $LiIO_3$ crystal. *Optics Express*, 19(11):10351–10358, 2011.

[52] R. L. Byer and S. E. Harris. Power and bandwidth of spontaneous parametric emission. *Physical Review*, 168:1064–1068, 1968.

[53] ASTM International. Standard tables for reference solar spectral irradiances: Direct normal and hemispherical on 37° tilted surface, 2020.

[54] R. Pitz-Paal. Concept and status of concentrating solar power systems. *EPJ Web Conf.*, 189:00008, 2018.

[55] J. Seres. Dispersion of second-order nonlinear optical coefficient. *Appl Phys B*, 73:705–709, 2001.

[56] Michael Küblböck, Mohammad Sahil, and Hanieh Fattahi. Solar-pumped radiation-balanced laser, 2026.

[57] Paul G. Kwiat. Hyper-entangled states. *Journal of Modern Optics*, 44(11-12):2173–2184, 1997.

[58] Julio T. Barreiro, Nathan K. Langford, Nicholas A. Peters, and Paul G. Kwiat. Generation of hyperentangled photon pairs. *Physical Review Letters*, 95(26):260501, 2005. Publisher: American Physical Society.

[59] Zhenda Xie, Tian Zhong, Sajan Shrestha, XinAn Xu, Junlin Liang, Yan-Xiao Gong, Joshua C. Bienfang, Alessandro Restelli, Jeffrey H. Shapiro, Franco N. C. Wong, and Chee Wei Wong. Harnessing high-dimensional hyperentanglement through a biphoton frequency comb. *Nature Photonics*, 9(8):536–542, Aug 2015.

[60] Abhinandan Bhattacharjee and Anand K. Jha. Experimental demonstration of structural robustness of spatially partially coherent fields in turbulence. *Opt. Lett.*, 45(14):4068–4071, Jul 2020.

[61] Y. Qiu and W. She. The influence of atmospheric turbulence on partially coherent two-photon entangled field. *Applied Physics B*, 108(3):683–687, Sep 2012.

[62] Samukelisiwe Purity Phehlukwayo, Marie Louise Umuhire, Yaseera Ismail, Stuti Joshi, and Francesco Petruccione. Influence of coincidence detection of a biphoton state through free-space atmospheric turbulence using a partially spatially coherent pump. *Phys. Rev. A*, 102:033732, Sep 2020.

[63] Brandon Redding, Michael A. Choma, and Hui Cao. Speckle-free laser imaging using random laser illumination. *Nature Photonics*, 6(6):355–359, Jun 2012.

[64] Yuanbo Deng and Daping Chu. Coherence properties of different light sources and their effect on the image sharpness and speckle of holographic displays. *Scientific Reports*, 7(1):5893, Jul 2017.

[65] Chloé Vernière and Hugo Defienne. Hiding images in quantum correlations. *Phys. Rev. Lett.*, 133:093601, Aug 2024.

[66] Anatoly Shukhin, Inbar Hurvitz, Leonid Vidro, Ady Arie, and Hagai S. Eisenberg. Direct polarization-entangled photon pair generation using domain-engineered nonlinear crystals. *Optica Quantum*, 3(5):487–494, Oct 2025.

[67] M. Zahirul Alam, Israel De Leon, and Robert W. Boyd. Large optical nonlinearity of indium tin oxide in its epsilon-near-zero region. *Science*, 352(6287):795–797, 2016.

[68] Orad Reshef, Israel De Leon, M. Zahirul Alam, and Robert W. Boyd. Nonlinear optical effects in epsilon-near-zero media. *Nature Reviews Materials*, 4(8):535–551, Aug 2019.

[69] Theng-Loo Lim, Yaswant Vaddi, M. Zahirul Alam, Shivashankar R. Vangala, Jeremy Upham, Joshua R. Hendrickson, and Robert W. Boyd. Highly efficient degenerate four-wave mixing with an epsilon-near-zero-based low-Q cavity. In *Advanced Photonics Congress 2024*, page NpTh3C.5. Optica Publishing Group, 2024.

[70] Yue-Wei Song, Heng Zhao, Li Chen, Yin-Hai Li, En-Ze Li, Ming-Yuan Gao, Ren-Hui Chen, Zhao-Qi-Zhi Han, Meng-Yu Xie, Guang-Can Guo, Zhi-Yuan Zhou, and Bao-Sen Shi. On-chip quantum states generation by incoherent light. *Nature Communications*, 16(1):11429, Dec 2025.